# Ionic Conductivity in Acceptor-Doped Barium Zirconate

Von der Fakultät für Mathematik, Informatik und Naturwissenschaften der RWTH Aachen University zur Erlangung des akademischen Grades eines Doktors der Naturwissenschaften genehmigte Dissertation

vorgelegt von
**Fabian Michael Draber, M.Sc.**
aus Köln

Berichter:
Universitätsprofessor Dr. rer. nat. Manfred Martin
Universitätsprofessor Dr. rer. nat. Arne Lüchow

Tag der mündlichen Prüfung: 26.02.2021

Diese Dissertation ist auf den Internetseiten der Universitätsbibliothek online verfügbar.

# Abstract

**Ionic Conductivity in Acceptor-Doped Barium Zirconate**

Acceptor-doped $BaZrO_3$ is a very promising material for different applications like electrolysers, fuel cells or for methane conversion cells. Although this material has already been investigated by different groups with theoretical and experimental methods, the understanding for the underlying processes on the atomic level is still limited. This work is supposed to expand understanding, therein. To do so, the explicit goal of this work is to connect macroscopically measurable values like ionic conductivity and microscopic processes like single ion jumps.

Through density functional theory calculations, microscopic properties like defect interactions and migration energies of protons and oxygen vacancies are calculated. These data are used in kinetic Monte Carlo simulations to predict the mobility of both species and the ionic conductivity. Here, the dependence on dopant fraction, degree of hydration and the type of dopant ions is investigated in particular.

It is predicted that protons are trapped at low dopant fractions. With increasing dopant fraction, these traps start to overlap and they build complete pathways through the crystal. Especially for yttrium doped barium zirconate, protons are able to move faster inside these pathways than outside. This leads to a strong increase in ionic mobility and conductivity. Comparing these results with experimental data shows good agreement. It is then predicted how the perfect yttrium defect structure to reach a maximum of increase in ionic conductivity is build.

Oxygen vacancies play a minor role in yttrium doped barium zirconate because they are much slower than protons. Nevertheless, for a full understanding of the material it is necessary to investigate them as well. Experimental findings that the ionic conductivity is mainly resulting from protons, could be confirmed. On top of that, it was found that oxygen vacancies play a much more important role in barium zirconate with other dopant ions, for example gallium.

It is experimentally very challenging to get barium zirconate with *either* protons or oxygen vacancies. Usually, both are there. Therefore, simulations were performed with both ions mobile at the same time. To our best knowledge, these are the first simulations of this kind.

This work is rounded off with some particularities like the investigation of the vehicle mechanism, where one proton and one oxygen ion jump together and in-depth research of the influence of the octahedral tilting in barium zirconate.

**Ionische Leitfähigkeit in Akzeptor-Dotiertem Bariumzirkonat**

Akzeptor-dotiertes Bariumzirkonat ist ein sehr vielversprechendes Material für verschiedene Anwendungsgebiete, wie zum Beispiel Elektrolysezellen, Brennstoffzellen oder bei der Methanumwandlung. Obwohl schon viele theoretische und praktische Untersuchungen dazu durchgeführt wurden, ist doch das Verständnis für die auf atomarer Ebene ablaufenden Prozesse bisher immernoch begrenzt. Diese Arbeit soll das Verständnis erweitern.

Das explizite Ziel dieser Arbeit ist es, einen Zusammenhang zwischen makroskopisch messbaren Größen wie der ionischen Leitfähigkeit und mikroskopisch ablaufenden Prozessen, wie einzelnen Ionensprüngen herzustellen.

Durch Dichtefunktionaltheorie-Rechnungen werden dabei mikroskopische Eigenschaften wie Defektwechselwirkungen und die Migrationsenergien von Protonen und Sauerstoffleerstellen bestimmt. Diese Daten werden in Kinetik Monte Carlo-Simulationen benutzt um die ionische Leitfähigkeit und Beweglichkeit von Protonen sowie Sauerstoffleerstellen in akzeptor-dotiertem Bariumzirkonat vorherzusagen. Dabei wird insbesondere die Abhängigkeit dieser Größen vom Dotiergrad, dem Hydratationsgrad und dem verwendeten Dotierion untersucht.

Es wird vorausgesagt, dass Protonen bei niedrigem Dotiergrad in energetischen „Fallen“ festsitzen. Bei steigendem Dotiergrad beginnen diese Fallen zu überlappen und bilden schließlich ganze Pfade durch den Kristall. Insbesondere in Yttrium-dotiertem Bariumzirkonat ist es möglich, dass sich Protonen entlang dieser Pfade bevorzugt und schneller bewegen als außerhalb. Dies führt zu einer Erhöhung der Beweglichkeit und Leitfähigkeit. Vergleiche dieser Ergebnisse mit experimentellen Daten zeigen eine gute Übereinstimmung. Es wird außerdem vorhergesagt, wie eine perfekte Yttrium-Defektstruktur in Bariumzirkonat aussehen müsste, um einen maximalen Zugewinn in der ionischen Leitfähigkeit zu erzielen.

Sauerstoffleerstellen spielen in Yttrium-dotiertem Bariumzirkonat eine eher untergeordnete Rolle, da sie deutlich langsamer sind als Protonen. Nichtsdestotrotz ist es für ein umfassendes Verständnis des Materials unerlässlich auch diese zu erforschen. Experimentelle Befunde, dass die Leitfähigkeit deutlich geringer ist, konnten bestätigt werden. Obendrein wurde gefunden, dass Sauerstoffleerstellen in Bariumzirkonat mit anderen Dotierionen, wie z.B. Gallium eine größere Rolle spielen könnten.

Es ist experimentell schwierig in Bariumzirkonat nur Sauerstoffleerstellen oder nur Protonen zu haben. Normalerweise sind beide vorhanden. Deshalb werden ebenfalls Simulationen durchgeführt, in denen beide Ionen beweglich sind. Nach bestem Wissen sind dies die weltweit ersten Simulationen dieser Art.

Diese Arbeit wird erweitert und abgerundet durch einige Besonderheiten wie dem Vehikelmechanismus, bei dem ein Proton und ein Sauerstoff zusammen springen und der Erforschung der Oktaederverkippung, die einen großen Einfluss in Bariumzirkonat hat.

# Acknowledgment

During my time at the Chair of Physical Chemistry 1, I was accompanied by a lot of nice people that all supported me on my way to my PhD. The first and most important person to mention is Prof. Dr. Manfred Martin. He not only supervised my work and helped me scientifically in every possible way. He also promoted my personal development and created an atmosphere in his work group that allowed working together as well as making friends and celebrating together.

Prof. Dr. Arne Lüchow is very gratefully acknowledged for his immediate willingness to review this thesis.

A special thanks go to Prof. Peter Schmidt for a large number of fruitful discussions and many very enjoyable journeys to Ober-Rahmstadt.

Many thanks go to "my" students Christiane Ader, Igor Graf von Westarp, Peter Müller, Jordy Peulen, Isabel Sommerfeld, Felix Melzer, Katharina Eickmeier und Johannes Denninger for their great work, which is partly presented in this thesis.

I am very grateful to Dr. Alexandra von der Heiden, Dr. Annalena Genreith-Schriever, Dr. Andreas Falkenstein, Dr. Christian Schwab, John Arnold, Maike Andresen, Dr. Markus Mann and Nils Bornwasser, who helped me a lot by proofreading this document.

Special thanks goes to my office colleagues, Dr. Julius Köttgen, Philipp Hein and Dennis Kemp for a nice working atmosphere. In particular, I would like to thank the whole work group of the Chair of Physical Chemistry 1. During my time and through a lot of social activities, many of you became more friends than colleagues.

I would like to thank Sebastian Kirchmeyer and Fabian Claßen for their incredible technical support at every occurring computer problem.

Finally, I want to thank my whole family very much. You were always there fore me to celebrate the good times and to support me during the hard times.

**Eidesstattliche Erklärung**

Ich, Fabian Michael Draber erkläre hiermit, dass diese Dissertation und die darin dargelegten Inhalte die eigenen sind und selbstständig, als Ergebnis der eigenen originären Forschung in meiner Zeit am Lehrstuhl 1 für Physikalische Chemie an der RWTH Aachen, unter Anleitung von Professor Dr. Manfred Martin generiert wurden.
Wann immer andere eigene oder Veröffentlichungen Dritter herangezogen wurden, wurden diese klar benannt. Wenn aus anderen eigenen oder Veröffentlichungen Dritter zitiert wurde, wurde stets die Quelle hierfür angegeben. Diese Dissertation ist vollständig meine eigene Arbeit, mit der Ausnahme solcher Zitate.
Alle wesentlichen Quellen von Unterstützung wurden benannt und wenn immer ein Teil dieser Dissertation auf derZusammenarbeit mit anderen basiert, wurde dies von mir klar gekennzeichnet.
Teile dieser Arbeit wurden bereits veröffentlicht in den auf der nächsten Seite angegebenen Veröffentlichungen.

Aachen den 17.11.2020

**Parts of this work have been published in the following article:**

Fabian M. Draber, Christiane Ader, John P. Arnold, Sebastian Eisele, Steffen Grieshammer, Shu Yamaguchi and Manfred Martin, "Nanoscale percolation in doped $BaZrO_3$ for high proton mobility", Nature Materials, **2020**, 19, 338–346.

**and oral presentations and posters:**

Fabian M. Draber and Manfred Martin, "A Kinetic Monte Carlo study of proton conductivity in doped $BaZrO_3$ inspired by first principles calculations", poster at 21th International Conference on Solid State Ionics (SSI-21), Padua, Italy, June 19, 2017.

Fabian M. Draber and Manfred Martin, "Ion conductivity in doped $BaZrO_3$", presentation at the 117$^{th}$ General Assembly of the German Bunsen Society for Physical Chemistry, Hannover, Germany, May 11, 2018.

Fabian M. Draber, Peter C. Müller, Isabel K. Sommerfeld and Manfred Martin, "A combined DFT and KMC study of ionic conductivity in doped $BaZrO_3$", presentation at the E-MRS Spring Meeting, Strasbourg, France, June 21, 2018.

Fabian M. Draber, Isabel K. Sommerfeld, Sebastian Eisele, John P. Arnold and Manfred Martin, "Kinetic Monte Carlo simulations on proton and oxygen conductivity in doped $BaZrO_3$", presentation at the 118$^{th}$ General Assembly of the German Bunsen Society for Physical Chemistry, Jena, Germany, May 31, 2019.

Fabian M. Draber and Manfred Martin, "Predicting the perfect dopant superstructure for maximum ionic conductivity in acceptor-doped $BaZrO_3$", poster at 22$^{nd}$ International Conference on Solid State Ionics (SSI-22), PyeongChang , South Korea, June 19, 2019.

Fabian M. Draber and Manfred Martin, "KMC Simulations on Proton and Oxygen Vacancy Conductivity in Doped $BaZrO_3$", presentation at the Konferenz über aktuelle Fragestellungen der physikalischen Festkörperchemie, Kall, Germany, August 7, 2019.

Fabian M. Draber and Manfred Martin, "Ionic conductivity in acceptor-doped $BaZrO_3$", presentation at the 11$^{th}$ Petite Workshop, Sommarøy, Norway, October 20, 2019.

**The following students finished their work under my supervision and their work is (partially) used in this thesis:**

Christiane Ader, "Abhängigkeit der Protonenleitfähigkeit in $BaZrO_3$ vom Dotieratom", research project, RWTH Aachen University, Aachen, 2016.

Igor Louis Graf von Westarp, "Protonenleitfähigkeit in dotiertem $BaZrO_3$", bachelor thesis, RWTH Aachen University, Aachen, 2017.

Peter Christian Müller, "Sauerstoffionenleitfähigkeit in dotiertem $BaZrO_3$", bachelor thesis, RWTH Aachen University, Aachen, 2017.

Jordy Johannes Andreas Peulen, "Untersuchungen zum Vehikelmechanismus in dotiertem $BaZrO_3$", bachelor thesis, RWTH Aachen University, Aachen, 2018.

Isabel Katja Sommerfeld, "Simulation of Proton and Oxide Ion Conductivity in $BaZrO_3$ using the Kinetic Monte Carlo Method", research project, RWTH Aachen University, Aachen, 2018.

Katharina Eickmeier, "Metropolis Monte Carlo Simulationen in $BaZrO_3$", research project, RWTH Aachen University, Aachen, 2020.

Jordy Johannes Andreas Peulen, "Untersuchung der Eigenschaften verschiedener Dopanden für akzeptor-dotiertes $BaZrO_3$", research project, RWTH Aachen University, Aachen, 2020.

Johannes Rudolph Denninger, "Kinetic Monte Carlo Simulation von Polaronen in $BaZrO_3$", research project, RWTH Aachen University, Aachen, 2020.

# Contents

# 1

# Introduction

"Basic research is what I am doing when I don't know what I am doing."
- Wernher von Braun (1912–1977), rocket engineer.

"The energy transition – which represents the efforts undertaken and results achieved on renewable energy expansion and energy efficiency – is our basis for a clean, secure and affordable energy supply, which is essential for all our lives." – these are the introductory words of "The National Hydrogen Strategy" from the German Federal Ministry for Economic Affairs and Energy in June 2020.[1] Not only the scarcity of fossil energy sources in today's world but also the 2030 Climate Action Plan from the federal government encourages politicians and scientists to look for other, preferably renewable energy sources and energy storage options.

One of the promising options is hydrogen. It can be obtained by the electrolysis of water in so-called electrolysers and can be used as an energy source in fuel cells. Its big advantage is, that it is storable. This way, energy from renewable sources like wind or solar power, which is usually just available during some hours of the day, can be stored for later use. Additionally, hydrogen is applied in many chemical and industrial processes. One very important example is the production of ammonia, in terms of product output and energy consumption one of the largest chemical processes in the world.[1]

Electrolysers and fuel cells both rely on electrolyte materials that can conduct ions but are electronically insulating. These electrolytes can belong to very different material classes, but solid oxides

are one promising class of materials, lending their name to solid oxide fuel cells (SOFCs).
In this work, the solid oxide electrolyte acceptor-doped $BaZrO_3$ is investigated by a combination of Density Functional Theory (DFT) calculations and kinetic Monte Carlo (KMC) simulations. The main focus is on the most prominent acceptor dopant yttrium. Nevertheless, other dopants like gallium, indium, scandium and gadolinium are studied as well. In the last years, acceptor-doped $BaZrO_3$ became an important topic of research. A closer look for example at the numbers of publications (Fig. 1.1) reveals the great effort and the growing interest many groups put into this research topic.[2–13]

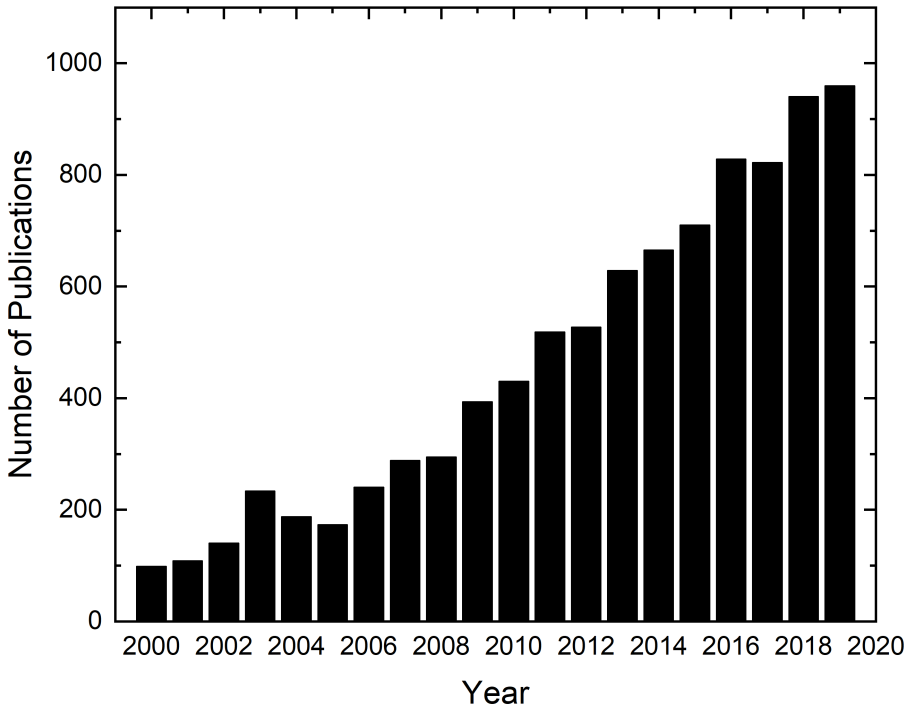


**Figure 1.1: The Number of publications found on Google Scholar that include the search terms "doped BaZrO3" in the title.** They are sorted by year of appearance as given from Google Scholar. At the end of July 2020, the number of publications for 2020 was already 697.

In the first part of this work, the fully hydrated case is studied. Here, only dopants and protons are considered. No other defects nor electrons or electron holes are taken into account here. This pictures the case where acceptor-doped $BaZrO_3$ is the perfect proton conductor. In the second part, the opposite is studied: The complete dry case, where only oxygen vacancies and dopants are considered. Here, the behaviour of oxygen vacancies without protons in acceptor-doped $BaZrO_3$ is investigated. Finally, in the third part, this work is rounded off with the combination of both parts: The dopant charge is compensated by oxygen vacancies and protons in different compositions.
In between, there are some important phenomena and special cases treated like the vehicle mechanism or the octahedral tilting.

# 2

# Ion Conduction

"In truth, there are only atoms and the void."
- Democritus (c. 460 BC–c. 370 BC), ancient Greek philosopher.

## 2.1 Ions and Crystals

Solid matter makes up a big part of our perceptible world. This can be materials as different as paper, wood, metal or glass. But also plants, animals, even we ourselves partly consist of solid matter. In natural science, it is defined by the solid state of matter. It differs from the liquid and gaseous states by the dense packing of the particles and their slow movement that lets solids keep their form.

The physical properties of solids can be very different from each other. They vary with the type of atoms the solid is made of as well as their composition and arrangement. A very fundamental property is the solid structure. This can be amorphous, where the solid has no long-range ordered structure, or crystalline.

In this work, we focus on one representative from the class of oxides, which in general denotes all chemical compounds that include oxygen with an oxidation number of −2. The largest part of the earth's crust consists of oxides (although not being solid, water is also an oxide) and therefore, they have been investigated in all of human history.

To constrain it further, this work will focus on the crystalline state. Crystals are solids that are built of regularly repeated "building blocks". These can be atoms, molecules or, in this case, ions. They form a three dimensional, highly symmetrical structure, the so-called lattice, where every ion has its crystallographic position. The smallest repetition unit is called the unit cell. There are different kinds of lattices, depending on the arrangement of the ions. Mathematically, they are described through 230 symmetrically unique space groups that can be categorized in seven different crystal systems, 14 Bravais lattices and 32 crystal classes.
A simple, descriptive example is magnesium oxide (MgO) that crystallizes in the sodium chloride structure, where every ion is surrounded by six ions of the opposite type (see Fig. 2.1). The unit cell contains 4 $Mg^{2+}$ and 4 $O^{2-}$ ions and is the smallest repetition unit that would build the whole crystal when expanded in all three dimensions.

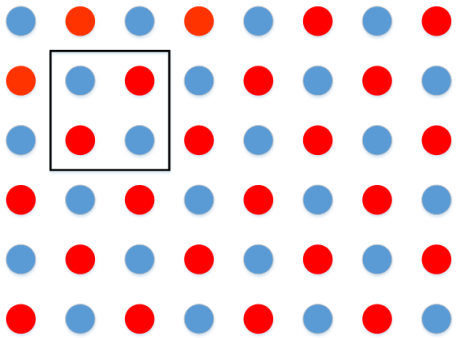

**Figure 2.1: Cut through the structure of magnesium oxide (MgO).** Magnesium is shown in blue and oxygen is shown in red. The black cube shows the unit cell.

## 2.2 Defects in Crystals

The perfect lattice can only exist at a temperature of 0 K, which is impossible to reach in the real world. Instead, at finite temperatures, disorders occur, resulting in so-called defects. This can be missing ions resulting in empty crystal positions or larger defects like displacements of whole lattice planes or crystal grains that are surrounded by a completely different crystal. These defects are of essential importance for the ionic conduction in solids. In fact, they were important enough to create a new term the "defect chemistry".
Defects are often categorized according to their dimension. A 0D defect is also called point defect and is therefore limited to one ion position. The following point defects exist:

1. Vacancies: One ion position is not occupied by an ion. It is empty.
2. Substitutions: One ion position is occupied by a foreign ion.
3. Interstitials: One ion occupies a place that is normally unoccupied in the perfect crystal.

To make the naming easier and more precise, Kröger and Vink suggested a nomenclature for point defects[14]. It contains the species S, the lattice position P and the charge C and is written as follows: $S_P^C$. The charge is set relative to the charge of the species that is supposed to be on the specific position. × represents a neutral, • a positive and ′ a negative relative charge. A magnesium ion on a Mg-position in a MgO crystal would be written as $Mg_{Mg}^{\times}$ while sodium on the same position would be written as $Na_{Mg}'$. Sodium is single positively charged and has therefore one positive charge less (or one negative charge more) compared to the bivalent magnesium. One particularity of this notation is the vacancy "V". If one lattice position is unoccupied this is written as a vacancy. If the above-mentioned magnesium position would be empty, this would be written as: $V_{Mg}''$. A magnesium ion is missing, therefore there are two positive charges too little on that position which is written as two negative charges. Because the spelling of the vacancy with a big "V" is confusing with the chemical element Vanadium, it is often written with a small "v". In this work however, it is written with a capital letter, because Vanadium plays no role.

Point defects are often correlated to keep the charge neutrality of the crystal. Their creation can be expressed by reaction equations written in Kröger-Vink notation. For example, the Schottky-disorder in MgO (see Fig. 2.2, left), where one formula unit is removed from the crystal, can be written as:

$$Mg_{Mg}^{\times} + O_O^{\times} \rightleftharpoons V_{Mg}'' + V_O^{\bullet\bullet} + MgO_{surface} \tag{2.1}$$

Other famous examples for 0D disorders are Frenkel- or Anti-Frenkel-disorders, where anions or cations, respectively, are moved from regular lattice sites to interstitial sites, written in the unoccupied state as $V_i^{\times}$. Frenkel-disorder (see Fig. 2.2, right) can be expressed as:

$$Mg_{Mg}^{\times} + V_i^{\times} \rightleftharpoons Mg_i^{\bullet\bullet} + V_{Mg}''. \tag{2.2}$$

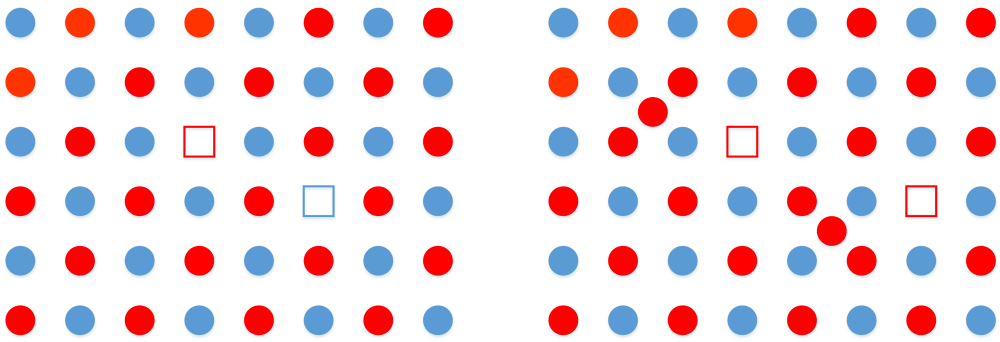

**Figure 2.2: Schottky- (left) und Anti-Frenkel-disorder (right) on the example of a MgO crystal.**
Magnesium is shown in blue, oxygen in red and the vacancies are squares in the respective colours.

While the corresponding equation for Anti-Frenkel-disorder would be:

$$O_O^{\times} + V_i^{\times} \rightarrow O_i'' + V_O^{\bullet\bullet}. \tag{2.3}$$

Higher dimensional defect disorders play a minor role in this work. 1D defects are also called line defects and they arise if one lattice plane ends in the crystal. Then, the lattice planes are bend around the step dislocation. The other kind of 1D disorder is the screw dislocation, where the ions follow a winding path around the screw axis which is the dislocation axis (see Fig. 2.3).[15]

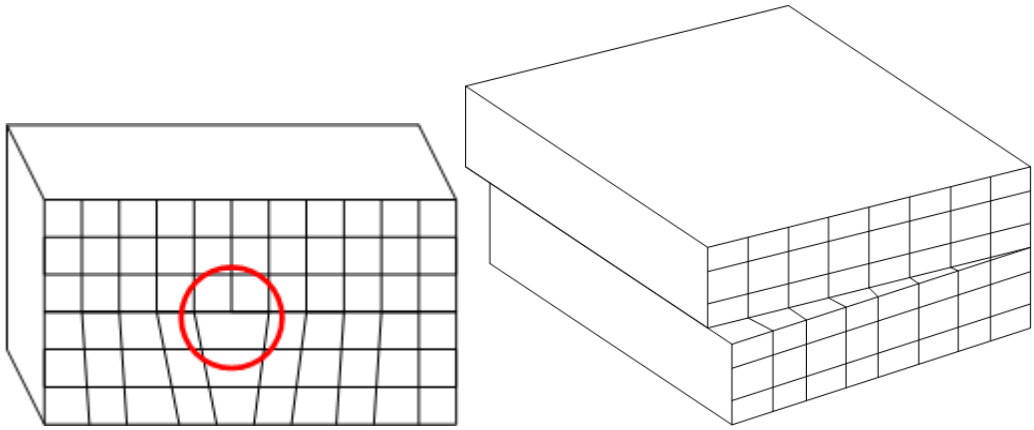

**Figure 2.3: 1D disorders in a crystal.** Left: One lattice plane ends in the crystal and the neighbouring lattice planes are bend around the disorder. Right: Screw disorder. Repainted after [15].

Two dimensional dislocations are planar defects like stacking faults, twin crystals and grain boundaries. The latter usually emerge, when two separate crystals grow together under oblique angles. They are known to influence the properties of a (poly-)crystal strongly. For example, ionic conductivity is different along grain boundaries and in the bulk crystal. Depending on the material it can be beneficial for ions to migrate along the grain boundary or adversely. For experimentalists, it is a challenge to distinguish between grain boundary and bulk conductivity.
Three dimensional defects are pores or grains, where a completely different material is grown into the crystal. This can be air in the case of pores or maybe remaining reagent from the crystal building reaction.

## 2.3 Ion Movement

Knowing, what a crystal is and how point defects are built, the next question is what these defects and the surrounding ions can *do*. If the temperature is high enough, the ions (and defects) start to move. Measurable conductivity is a consequence of this ion movement, making it a central part of this work. When it comes to ion movement, there is more than one way to approach the topic. In the following, the microscopic way is described. The main sources for the whole subchapter are the textbooks written by Maier[15] and by Ielmini *et. al.*[16]
Ions move through the crystal by a variety of ion jumps. Different mechanisms are imaginable. The three most common ones are the vacancy mechanism, where one ion and one vacancy change places, the interstitial mechanism, where one ion on an interstitial position moves to another inter-

stitial position and the interstitialcy mechanism, where one ion on an interstitial "pushes" an ion on a regular position to an interstitial position taking its place instead. They are shown in figure 2.4.

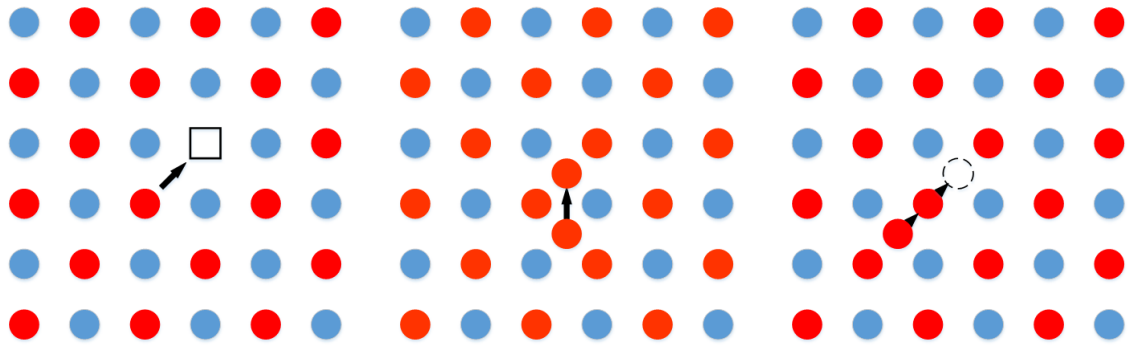

**Figure 2.4: Schematic drawing of the three most common diffusion mechanisms in solid oxides.** Left: Vacancy, middle: interstitial and right: interstitialcy mechanism.[16]

If the direction of the ions movement is called x-direction, Einstein and Smoluchowski derived the following equation for the diffusion coefficient:[17,18]

$$D = \frac{\langle(\Delta\vec{x})^2\rangle}{2 \cdot d \cdot t}. \tag{2.4}$$

With $\langle(\Delta\vec{x})^2\rangle$ being the mean squared displacement in $x$-direction in the time $t$. $d$ is the dimensionality ranging from 1 to 3 for 1D to 3D problems. For a random walker, $\langle(\Delta\vec{x})^2\rangle$ can be expressed by $\langle(\Delta\vec{x})^2\rangle = n\lambda^2$ with $\lambda$ being the jump length and $n$ the number of jumps. Equation 2.4 can be written as:

$$D = \frac{n\lambda^2}{2 \cdot d \cdot t}. \tag{2.5}$$

If we consider now the particles jump rate $\Gamma$ to one of the $Z$ neighbouring sites, with $\Gamma Z = n/t$ for a three-dimensional diffusion problem we get:

$$D = \frac{1}{6}\lambda^2 \Gamma Z. \tag{2.6}$$

Every jump has to go through an energetically unfavourable transition state and therefore has to overcome an energy barrier $E_{\mathrm{mig}}$. This barrier and the attempt frequency $\nu_0$ are connected through the Arrhenius law:

$$\Gamma = \nu_0 \cdot \mathrm{e}^{\left(\frac{-E_{\mathrm{mig}}}{k_{\mathrm{B}}T}\right)}. \tag{2.7}$$

Here, $k_{\mathrm{B}}$ is the Boltzmann constant and $T$ the temperature. For $\nu_0$, the Debye-frequency $10^{13}$ $\mathrm{s}^{-1}$ is often used.

The ionic conductivity $\sigma$ can be written as the sum over the products of the (electrochemical) mobility $u$, the concentration $c$ and the charge $q$ of each mobile species $i$:[19]

$$\sigma = \sum_{\mathrm{i}} u_{\mathrm{i}} \cdot c_{\mathrm{i}} \cdot q_{\mathrm{i}}. \tag{2.8}$$

Nernst and Einstein found an expression for the mobility that is known as the Nernst-Einstein-Equation:[20]

$$u_{\mathrm{i}} = \frac{D_{\mathrm{i}} q_{\mathrm{i}}}{k_{\mathrm{B}} T}. \tag{2.9}$$

Combining equations 2.6 – 2.9 for the conductivity of species *i*, we get:

$$\sigma = \sum_{\mathrm{i}} \frac{\lambda^2 q_i^2 Z \nu_0}{6 k_{\mathrm{B}} T} c_{\mathrm{i}} \mathrm{e}^{\left(\frac{-E_{\mathrm{mig}}}{k_{\mathrm{B}} T}\right)}. \tag{2.10}$$

## 2.4 Barium Zirconate

Barium zirconate crystalizes in a cubic perovskite structure ($ABO_3$) in the space group 221 ($Pm\bar{3}m$).[21] The unit cell has a lattice parameter of 4.18 Å at room temperature.[22] The unit cell can be built with zirconium at the corners of the cell (0.0, 0.0, 0.0 in fractional coordinates), while barium is in the middle (0.5, 0.5, 0.5). Oxygen is located at the middle of the edges (0.5, 0.0, 0.0 / 0.0, 0.5, 0.0 / 0.0, 0.0, 0.5) and builds one oxygen octahedron around zirconium (see Fig. 2.5).

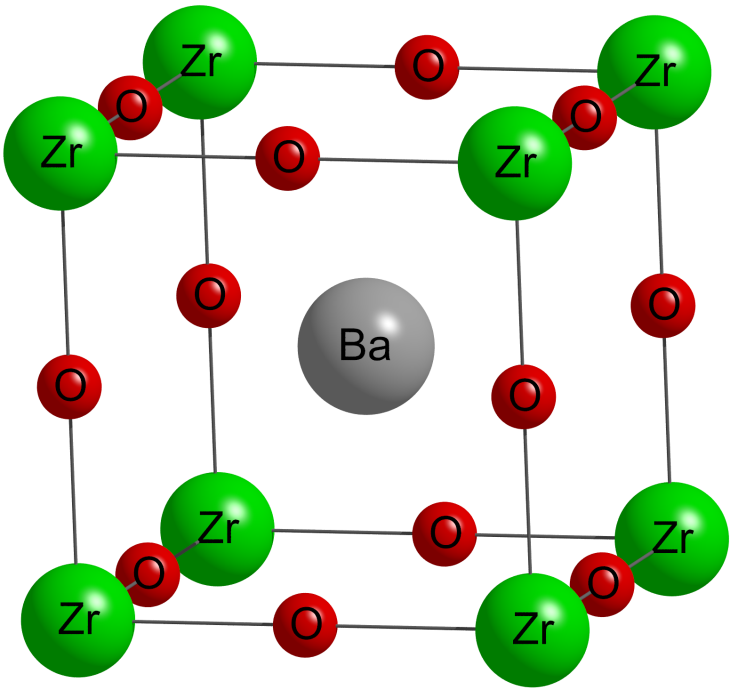


**Figure 2.5: Unit cell of $BaZrO_3$.** Zirconium is shown in green, barium in grey and oxygen in red.

$BaZrO_3$ has a band gap of 5.3 eV and is therefore an insulator.[23,24] It is thermally and chemically very stable with a melting temperature around 2900 °C[25] and additionally, when doped with yttrium on the B-site and hydrated, it is known for its high proton conductivity.[26]

# 3

# Density Functional Theory

"A person who isn't outraged on first hearing about quantum theory doesn't understand what has been said."

- Niels Bohr (1885–1962), physicist and Nobel Prize winner.

## 3.1 The Foundation

This chapter is mainly based on the textbooks written by Dronskowski[27] and by Sholl and Steckel.[28] Density Functional Theory is an important tool in solid-state chemistry. Its foundation, as for all quantum mechanical calculations is the time-independent Schrödinger equation:

$$\hat{H}\Psi = E\Psi, \tag{3.1}$$

with $\Psi$ as the wave function of the system and $E$ as the energy eigenvalue. The determination of these energy eigenvalues is the goal of quantum mechanical calculations and it is achieved by applying the Hamiltonian $\hat{H}$ to the wave function:

$$\hat{H} = -\sum_{\mathrm{i}=1}^{\mathrm{N}} \frac{\hbar^2}{2m_e}\nabla_i^2 - \sum_{\mathrm{A}=1}^{\mathrm{M}} \frac{\hbar^2}{2M_{\mathrm{A}}}\nabla_{\mathrm{A}}^2 - \frac{1}{4\pi\epsilon_0}\left(\sum_{\mathrm{i}=1}^{\mathrm{N}}\sum_{\mathrm{A}=1}^{\mathrm{M}} \frac{Z_{\mathrm{A}}e^2}{r_{\mathrm{iA}}} - \sum_{\mathrm{i}=1}^{\mathrm{N}}\sum_{\mathrm{j}>\mathrm{i}}^{\mathrm{N}} \frac{e^2}{r_{\mathrm{ij}}} - \sum_{\mathrm{A}=1}^{\mathrm{M}}\sum_{\mathrm{B}>\mathrm{A}}^{\mathrm{M}} \frac{Z_{\mathrm{A}}Z_{\mathrm{B}}e^2}{R_{\mathrm{AB}}}\right). \tag{3.2}$$

Here, the Hamiltonian contains five terms: the kinetic energy of $N$ electrons (first term in Eq. 3.2) and $M$ nuclei (second term), the attraction between electrons and nuclei and the repulsion between electrons or between nuclei, respectively (terms three to five). $m_e$ and $M_A$ are the masses and $e$ and $Z$ the charges of electrons and nuclei, respectively. $r_{iA}$, $r_{ij}$ and $R_{AB}$ are the distances between electrons and nuclei, two electrons and two nuclei. $\nabla$ is the differential operator, sometimes also called nabla. The dot product $\nabla \cdot \nabla$ yields the Laplace operator $\nabla^2$:

$$\nabla^2 = \frac{\partial^2}{\partial x^2} + \frac{\partial^2}{\partial y^2} + \frac{\partial^2}{\partial z^2}. \tag{3.3}$$

Note, that this equation refers to cartesian coordinates.[27] Unfortunately, an exact analytical solution is only possible for very simple systems like the hydrogen atom. Therefore, several approximations have to be made.

First, we make use of the positions of the nuclei that are much heavier than electrons and therefore move much slower. Every change of the nuclei's position is followed immediately by a fast adjustment of the electrons. To determine electronic properties, the nuclei can be treated as immobile and their kinetic energy can be ignored according to the Born-Oppenheimer approximation.[29]

We then use Hartree atomic units and write the simplified Hamilton operator as follows:

$$\hat{H} = -\sum_{i=1}^{N} \frac{1}{2}\nabla_i^2 - \sum_{i=1}^{N}\sum_{A=1}^{M} \frac{Z_A}{r_{iA}} + \sum_{i=1}^{N}\sum_{i>j}^{N} \frac{1}{r_{ij}}. \tag{3.4}$$

To solve the Schrödinger equation, even with these approximations, wave functions of $N$ electrons have to be calculated, resulting in $3N$ (due to the 3 dimensions in space) coordinates that have to be calculated. This is challenging for small systems and not practical if not impossible for large systems.

To circumvent this problem, Thomas[30] and Fermi[31] came up with the idea of a homogeneous electron gas (or electron density) with only three coordinates $\rho(\mathbf{r})$. Unfortunately, this theory had some serious problems. The greatest problem is the impossibility of describing chemical bonding with this theory, which made it unsuccessful.

The idea, however, was continued by Hohenberg and Kohn,[32] who laid the foundation to density functional theory. To calculate the electron density $\rho(\mathbf{r})$, they postulated two theorems, that are fundamental for DFT:

1. The energy $E$ of a system is a functional of the electron density:

$$E = E[\rho(\mathbf{r})]. \tag{3.5}$$

2. The true ground state electron density $\rho_0(\mathbf{r})$ minimizes the energy. Its energy is the lower bound of the energy of a test density of the ground state.

$$E_0 = E[\rho_0(\mathbf{r})] \leq E[\rho(\mathbf{r})]. \tag{3.6}$$

If the functional was known, one could vary the electron density until the energy was minimized to find the energetic ground state. This is called the variational principle. Unfortunately, the exact functional is unknown. Therefore, to calculate the energy, Kohn and Sham introduced an approximation.[33] A reference system with the same electron density was introduced, in which the electrons do not interact with each other. There, the energy is the sum of four terms:

$$E[\rho(\mathbf{r})] = T_0[\rho(\mathbf{r})] + \frac{1}{2}\int d\mathbf{r}\int d\mathbf{r}'\frac{\rho(\mathbf{r})\rho(\mathbf{r}')}{|\mathbf{r}-\mathbf{r}'|} + \int d\mathbf{r}V_{\text{ext}}(\mathbf{r})\rho(\mathbf{r}) + E_{\text{exc}}[\rho(\mathbf{r})]. \tag{3.7}$$

The first three terms make up most of the energy and they can be determined exactly. They are the kinetic energy of electrons, the interaction of electron densities with each other and the nuclei, respectively.

This shifts all uncertainties or sources of error to the last term, the exchange and correlation energy $E_{\text{exc}}[\rho(\mathbf{r})]$, that has to be approximated. Therefore, an exchange and correlation functional is needed and the precision of DFT calculation depends strongly on this functional. There are two main approaches in DFT: The *local density approximation* (LDA), where the energy of the real system is replaced by the energy of a non-interacting homogeneous electron gas with the same electron density. Although achieving good results, the LDA has problems with the description of chemical bonding. As a consequence, an improved functional was developed: The *generalized gradient approximation* (GGA), which is also used in this work. The GGA does not only consider the electron density but also their change (gradient)[27] and is expressed as:

$$E_{\text{exc}}^{\text{GGA}}[\rho(\mathbf{r})] = \int \rho(\mathbf{r})F[\rho(\mathbf{r}),\Delta\rho(\mathbf{r})]d\mathbf{r}. \tag{3.8}$$

Here, $F$ is the exchange and correlation functional.

## 3.2 Application to Solids

Crystals or solids in general are widely extended objects with a large number of atoms and electrons. Calculating the energy even of a small crystal would take an almost infinitely long time. It is only made possible through Bloch's theorem,[34] which describes the wave function at all positions in the crystal by using its translational invariance:

$$\Psi(\mathbf{r},\mathbf{k}) = \Psi_0(\mathbf{r},\mathbf{k})\cdot e^{i\mathbf{kr}}. \tag{3.9}$$

The wave function at a certain place $\Psi(\mathbf{r},\mathbf{k})$ is the product of the basis wave function $\Psi_0(\mathbf{r},\mathbf{k})$ and a phase factor $e^{i\mathbf{kr}}$. $\mathbf{r}$ and $\mathbf{k}$ are the positions in real and reciprocal space, respectively. They are connected through a Fourier transformation. Due to the translational invariance, it is sufficient to perform calculations in the first Brillouin zone of a cubic unit cell. Usually, only a few $\mathbf{k}$-points have to be calculated, and these can be found using the Monkhorst-Pack method.[35] The wave function $\Psi_0(\mathbf{r},\mathbf{k})$ can be expanded by a combination of plane waves:

$$\Psi_0(\mathbf{r},\mathbf{k}) = \sum_{\mathbf{G}} c_{\mathbf{G}}\cdot e^{i\mathbf{Gr}}, \tag{3.10}$$

with **G** being the lattice vector in reciprocal space. Combining equations 3.9 and 3.10 leads to:

$$\Psi(\mathbf{r},\mathbf{k}) = \sum_{\mathbf{G}} c_{\mathbf{G}+\mathbf{k}} e^{i(\mathbf{G}+\mathbf{k})\mathbf{r}}. \tag{3.11}$$

To calculate the energy at one single point in reciprocal space, one would have to sum over an infinite number of values of **G**. Plane waves can be interpreted as solutions of the Schrödinger equation with a certain kinetic energy. Therefore, it is possible to define a cut-off energy $E_{\text{cut}}$ to delimit the number of them:

$$E_{\text{cut}} = \frac{\hbar^2}{2m}\mathbf{G}_{\text{cut}}^2. \tag{3.12}$$

Only plane waves with a kinetic energy lower than $E_{\text{cut}}$ are used in the calculation. This is still not sufficient to make calculations possible. Between atoms, only a few plane waves are needed do describe the flat electronic wave function. Close to the cores, there are strong oscillations whose exact description would take plane waves with extremely high cut-off energies. For the description of chemical bonding, however, it is not necessary to describe the wave function around the core exactly. Therefore, pseudopotentials are used trading the loss of information about electrons in the core region against a significant decrease in computation time needed for the calculation. One of the most efficient methods is the projector augmented-wave (PAW) method, where augmented plane waves are used instead of plane waves.

## 3.3 The Transition State

To calculate the migration energy of an ion jump, it is necessary to know the transition state. The nudged elastic band (NEB) method is used,[36,37] a method that can find minimum energy pathways and saddle points in energy landscapes.

Starting with fully relaxed initial and final states, an imaginary band is stretched to connect both states. Along this band, the ion positions of one or more intermediate configurations (so-called images) are interpolated. These images are connected with artificial spring forces of 5 eV/Å. During the calculation, the atom positions of the images are relaxed in that way, that $F_{\text{i}}^{\text{NEB}}$ is minimized:

$$F_{\text{i}}^{\text{NEB}} = F_{\text{i}}^{\nabla\perp} + F_{\text{i}}^{\text{S}\parallel}, \tag{3.13}$$

with $F_i^{\nabla\perp}$ being the force created through the potential gradient orthogonal to the band and $F_i^{\text{S}\parallel}$ being the spring force parallel to the band. Both are varied during the optimization.

Although this method is good in finding minimum energy pathways, it sometimes fails to find the exact maximum of the path, the saddle point. This is especially the case when the pathway is not symmetrical. But this saddle point is of special interest because the energetic difference between the initial (or final) state and the saddle point configuration is exactly the height of the migration barrier. Therefore, a modified NEB method is used, the *climbing image* NEB method. It switches off the spring forces for the image with the highest energy. This moves the image up to higher energy

values along the band (climbing) and to lower energy values perpendicular to the band. In the fully converged state, this image depicts exactly the saddle point.

## 3.4 Computational Details

The computational details of the density functional theory calculations have been published in a similar way.[13]

All interaction and migration energies were calculated using density functional theory within the generalized gradient approximation (GGA) according to Perdew, Burke und Ernzerhof (PBE)[38] and the projector augmented wave method (PAW)[39] as implemented in the Vienna Ab initio Simulation Package (VASP).[40,41] The climbing image nudged elastic band method (CI-NEB)[36,37] was used to investigate the transition states and the minimum energy pathways. For all calculations on $BaZrO_3$, plane waves with an energy cut-off of 500 eV and a $6 \times 6 \times 6$ Monkhorst-Pack $k$-point mesh[35] were used for the $Pm\bar{3}m$ unit cell. The convergence parameters for the electronic and ionic relaxation were set to $10^{-5}$ eV and $10^{-2}$ eV/Å, respectively. The valence electrons can be seen in table 3.1.

**Table 3.1: Valence electrons in VASP.**

| Element | Valence electrons |
|---|---|
| Ba | $5s^2 5p^6 6s^2$ |
| Ga | $4s^2 4p^1$ |
| Gd | $5p^6 5d^1 6s^2$ |
| H | $1s^1$ |
| In | $4d^{10} 5s^2 5p^1$ |
| O | $2s^2 2p^4$ |
| Sc | $3s^2 3p^6 3d^3$ |
| Y | $4s^2 4p^6 5s^2 4d^1$ |
| Zr | $4s^2 4p^6 5s^2 4d^2$ |

For all defective cells, the number of electrons was adapted to reproduce the real charge state of the defect. For the elemental cell of pure $BaZrO_3$ a lattice constant of 4.23 Å was calculated using the Birch-Murnaghan equation of state.[42,43] This lattice constant was used for all calculations. To avoid errors from self-imaging of defects, finite-size corrections after Makov and Payne[44] are carried out for interaction and migration energies. Therefore, supercells of various sizes were used in the calculations: $2 \times 2 \times 2$ supercells (containing 40 atoms), $2\sqrt{2} \times 3\sqrt{2} \times 2$ supercells (120 atoms), $3 \times 3 \times 3$ supercells (135 atoms), $2\sqrt{2} \times 3\sqrt{2} \times 4$ supercells (240 atoms), $4 \times 4 \times 4$ supercells (320 atoms) and $3\sqrt{2} \times 3\sqrt{2} \times 4$ supercells (360 atoms). The internal atomic positions were relaxed for every calculation to minimize the energy of the cell.

# 4

# Monte Carlo Simulations

"Anyone who considers arithmetical methods of producing random digits is, of course, in a state of sin."

- John von Neumann (1903–1957), mathematician.

## 4.1 Metropolis Monte Carlo

In the early twentieth century, there were two different mathematical methods of treating physical problems. It was possible to describe problems that included only very few particles in classical mechanics and it was possible to describe problems with very many particles through statistical mechanics.[45] Metropolis and Ulam[45] wrote in 1949 about the need for a method that was able to describe problems that were "in between" with more than a few but fewer than very many particles. They called it the Monte Carlo Method.

It is somehow difficult to trace back the original inventor of this method. That is because it was developed further in the Manhattan Project at Los Alamos Scientific Laboratory with strict confidentiality during the second world war. Nevertheless, it is widely accepted, that the foundation for Metropolis Monte Carlo simulations was laid by Nicholas Metropolis and co-workers in 1953.[46] The following chapter is mainly based on this work. They used the supercomputer MANIAC to perform Metropolis Monte Carlo simulations with 224 particles over up to 48 cycles which took them

about three minutes per cycle. And even though computer power has increased tremendously since then, the principles of the Metropolis Monte Carlo algorithm are still the same.
At the beginning, we have a system with $N$ particles and known positions. The potential energy of the system can be calculated according to Metropolis *et al.*:[46]

$$E = \frac{1}{2}\sum_{i=1}^{N}\sum_{j=1,i\neq j}^{N} V(d_{ij}), \tag{4.1}$$

with $V$ as the potential between the particles and $d_{ij}$ as the minimum distance between particles. Assuming that $F$ is the systems quantity we are interested in, we can perform an integration over the complete configurational space. Here, the exact calculation would include to carry out a large number of integrals which would take a lot of time. Instead, we construct a lattice, where all the particles are distributed randomly. This is called the initial configuration. In the next step, we start the simulation and move the particles in a certain way. Metropolis *et al.*[46] let the particles move freely in the simulation box, whereas we will later restrict them to lattice positions in our crystal. After one movement step (Monte Carlo step), for example the exchange of two ions, the change in energy $\Delta E$ of the system is calculated. If $\Delta E < 0$, the movement step is accepted and the new configuration is the starting configuration for the next step. But if $\Delta E > 0$, the movement step is only accepted if a random number between 0 and 1 is smaller than the Boltzmann factor:

$$p = \mathrm{e}^{-\frac{\Delta E}{k_B T}}. \tag{4.2}$$

If the random number is larger, the movement step is not accepted and the previous configuration is used again. Now, we calculate the quantity of interest $F_j$ after the $j^{th}$ and proceed with the next movement step and so on. If we continue long enough with these simulations, the system strives for an equilibrium distribution. In this equilibrium distribution, the systems' energy only fluctuates and the quantity of interest is stable against the number of Monte Carlo Steps $M$ and can be calculated according to

$$\overline{F} = \left(\frac{1}{M}\right)\sum_{j=1}^{M} F_j. \tag{4.3}$$

Metropolis *et al.* did 48 simulation cycles trying to equilibrate their system. At present, it is possible to run millions of cycles with big simulation systems within seconds.

## 4.2 Kinetic Monte Carlo

While for Metropolis Monte Carlo simulations time does not play a role, it is of central importance in kinetic Monte Carlo simulations. A description of a Kinetic Monte Carlo algorithm was given by Murch in the late 70s and early 80s.[19,47,48] He used a supercell with 20×20×20 ion positions with 7999 ions and one vacancy, that worked as a tracer. Ions move through the supercell according to a vacancy mechanism and periodic boundary conditions are applied which means, that an ion moving out of the simulation cell on one side reenters on the opposite side. The tracer will perform a completely random walk through the crystal and the movement of every ion is tracked. Using the Einstein-Smoluchowski equation (Eq. 2.4),[17,18] the diffusion coefficient is calculated. Murch computed a tracer concentration profile after 640000 Monte Carlo steps. Therefore, he performed the experiment several times and plotted the end position of the tracer. The resulting diagram showed the expected Gaussian shape.[47]

It is possible to calculate the ionic conductivity and mobility from the mean displacement of ions. Therefore, Kinetic Monte Carlo simulations with a constant driving force, *e.g.* an electric field $E_{\text{field}}$ are performed. This driving force splits the probability of one jump being accepted up into three probabilities: jumps in field direction ($p^+$), against field direction ($p^-$) and perpendicular to the field($p^\perp$):

$$p^+ = \mathrm{e}^{\left(-\frac{\left(E_{\text{mig}}-\frac{1}{2}q\lambda E_{\text{field}}\right)}{k_{\text{B}}T}\right)} \tag{4.4}$$

$$p^- = \mathrm{e}^{\left(-\frac{\left(E_{\text{mig}}+\frac{1}{2}q\lambda E_{\text{field}}\right)}{k_{\text{B}}T}\right)} \tag{4.5}$$

$$p^\perp = \mathrm{e}^{\left(-\frac{E_{\text{mig}}}{k_{\text{B}}T}\right)} \tag{4.6}$$

For positively charged defects, jumps in field direction are more likely accepted while those against the field are less likely accepted. The difference in terms of energy is the product of the ion charge $q$, the jump length $\lambda$ and the contribution of the electric field $E_{\text{field}}$ for that jump. We assume the jump barrier in the middle of the jump, the factor $\frac{1}{2}$ is included (see Fig. 4.1). Consequentially, jumps against the field have to overcome an energy of $E_{\text{mig}} + \frac{1}{2}q\lambda E_{\text{field}}$ and those in field direction $E_{\text{mig}} - \frac{1}{2}q\lambda E_{\text{field}}$ (see Fig. 4.1).

Now the average drift velocity $\langle v\rangle$ can be expressed as[19]

$$\langle v\rangle = v_0\lambda \cdot \mathrm{e}^{\left(\frac{-E_{\text{mig}}}{k_{\text{B}}T}\right)} \cdot \sinh\left(\frac{\frac{1}{2}q\lambda E_{\text{field}}}{k_{\text{B}}T}\right). \tag{4.7}$$

For small fields, meaning $q\lambda E_{\text{field}} \ll k_{\text{B}}T$, the small angle approximation can be made and the sinh term is expressed as a Taylor series truncated after the first term. This approximation is called the *weak-field approximation* hereinafter. Thereby, $\sinh x \approx x$ is valid and the drift velocity becomes

$$\langle v\rangle = v_0\lambda \cdot \mathrm{e}^{\left(\frac{-E_{\text{mig}}}{k_{\text{B}}T}\right)} \cdot \frac{\frac{1}{2}q\lambda E_{\text{field}}}{k_{\text{B}}T}. \tag{4.8}$$

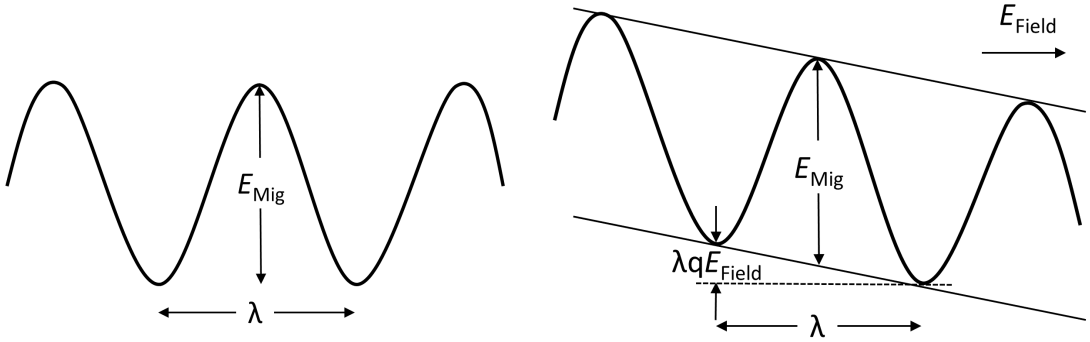


**Figure 4.1: Schematic energy barrier diagrams.** Shown are the energy barriers in the absence of an electric field (left) and in the presence of an electric field in positive $x$-direction (right). Repainted after [19].

With $\langle v \rangle = u \cdot E_{\text{field}}$, we get the drift mobility $u$:

$$u = v_0 \lambda \cdot e^{\left(\frac{-E_{\text{mig}}}{k_B T}\right)} \cdot \frac{\frac{1}{2} q \lambda}{k_B T} = \frac{\langle x \rangle}{E_{\text{field}} \cdot t}. \tag{4.9}$$

The ionic conductivity $\sigma$ is generally defined by the product of concentration mobility and charge of each species $i$ involved (eq. 2.8).[19] The weak-field approximation was tested by simulating the ionic conductivity for different field strengths (see Fig. 4.2). The physical time $t$ can be calculated from the sum of the single jump processes:[49]

$$t = \sum_{i=1}^{\text{MCS}} \Delta t = \frac{N_{\text{jumpatt}}}{N_{\text{Mob}} \cdot Z \cdot v_0}, \tag{4.10}$$

with $N_{\text{jumpatt}}$ as the number of jump attempts during the simulation, $N_{\text{Mob}}$ as the number of mobile species (for example protons or oxygen vacancies), $Z$ as the number of possible jump directions and $v_0$ as the attempt frequency. The latter is often set to the Debye-frequency $10^{13}$ $s^{-1}$ because it is difficult and time-consuming to calculate attempt frequencies.

Equation 4.10 is only valid for simulations with just one kind of mobile species. It could be shown, that it changes for more than one mobile species to:[50,51]

$$t = \sum_{j=1}^{\text{MCS}} \langle \Delta t \rangle = \frac{N_{\text{jumpatt}}}{N_{\text{Mob}} \cdot \langle Z \rangle \cdot v_0}. \tag{4.11}$$

Here, $\langle \Delta t \rangle$ is the averaged time between two state changes and $\langle Z \rangle$ the averaged number of possible jump directions of all species. MCS is the total number of all *Monte Carlo Steps* in the simulation while MCSP, which is later used, describes the *Monte Carlo Steps per Particle*.

In an exemplary study on acceptor-doped ceria, Köttgen *et al.*[52] combined DFT+U, NEB, phonon calculations and the transition state theory to calculate attempt frequencies within different definitions. One of their ways, the harmonic approximation, is also used in this work to estimate the attempt frequency.

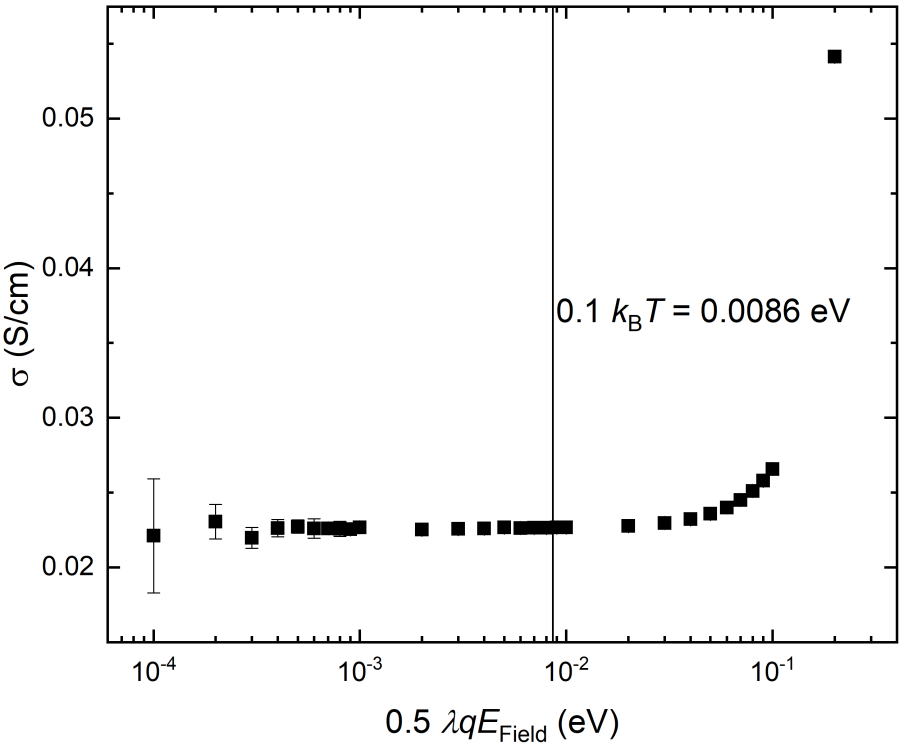


**Figure 4.2: Simulated proton conductivity in acceptor-doped $BaZrO_3$ depending on the electric field strength $E_{field}$.** $q$ is the charge of the ions, $\lambda$ the jump length. The simulations were performed in a 16×16×16 supercell at $T$ = 1000 K with 10000 MCSP. The vertical line marks $E_{pot}$ = 0.1 $k_B T$, that was used for all other calculations in agreement with [49].

## 4.3 iCon and MOCASSIN

Kinetic Monte Carlo simulations were performed using the programs iCon by Philipp Hein *et al.*[53] and MOCASSIN by Sebastian Eisele and Steffen Grieshammer.[54] The Monte Carlo algorithm[19] was implemented in C++ and random numbers were generated by the MT19937 random number generator (iCon)[55] or the PCG32 (MOCASSIN).[56] All jumps were carried out in a supercell containing 10 × 10 × 10 (Mocassin) or 16 × 16 × 16 (iCon) unit cells with periodic boundary conditions. We followed the method of Grope *et al.*[49] and applied a weak electric field which leads to a displacement of the mobile species in, or against the field direction, depending on the species' charge. A field strength of 0.1 $k_B T$ was used in iCon and $E_{Field}$ is calculated depending on the temperature, while in MOCASSIN $E_{Field}$ is set directly to $10^7$ V/m. Despite the different type of setting, for all relevant systems, they do not influence the thermodynamic equilibrium. To achieve good accuracy, jump attempts were carried out until every proton site was visited by a proton at least 10000 times on average. The initial starting configuration for the protons is completely random. To equilibrate the system before the data collection started, a pre-run was performed with 1 % of the jumps of the production run. For good statistical accuracy, every calculation was repeated at least five times.

# 5

# The Defect Model

"Zwei Dinge sind zu unserer Arbeit nötig: Unermüdliche Ausdauer und die Bereitschaft, etwas, in das man viel Zeit und Arbeit gesteckt hat, wieder wegzuwerfen."

- Albert Einstein (1879–1955), physicist and Nobel Prize winner.

The defect model has been developed over the years this work took. Parts of it have already been published in previous publications.[13,57] Nevertheless, this chapter provides the full defect model with all species – mobile or not – and their interactions with each other.

## 5.1 The Simplified Model

Pure, ideal $BaZrO_3$ has no defects at 0 K. At temperatures higher than 0 K, some defects are thermally evoked. The majority though, comes from the incorporation of lower valent acceptor dopants on the zirconium site. The most common one for $BaZrO_3$ is yttrium[2,12,26,58–60], but many others are possible (Tab. 5.1). Most dopants are triple positively charged but there are some investigations on two times positively charged dopant ions ($Co^{2+}$, $Fe^{2+}$, $Mg^{2+}$ and $Zn^{2+}$). Nevertheless, they are abbreviated with DOP in the following and the explanation of the defect model is carried out exemplarily for triple positively charged ions, while the changes for other charges are marginal.
During the sinter process, $BaZrO_3$ is doped with an acceptor dopant and the charge is compensated

**Table 5.1: Dopants for the B-site in $BaZrO_3$.**

| Dopant | experiment | theory |
|---|---|---|
| $Al^{3+}$ | [12, 58] | [61, 62] |
| $Bi^{3+}$ | [63] | |
| $Ce^{3+}$ | [64, 65] | |
| $Co^{3+}$ | [66] | |
| $Dy^{3+}$ | [2, 67] | [62] |
| $Er^{3+}$ | [60, 63, 68] | [62] |
| $Eu^{3+}$ | [60, 67] | |
| $Fe^{3+}$ | [69–72] | |
| $Ga^{3+}$ | [2, 12, 63, 73–76] | [59, 62, 77] |
| $Gd^{3+}$ | [26, 58, 60, 63, 65, 78–81] | [59, 73, 77, 82, 83] |
| $Ho^{3+}$ | [60, 63, 68] | [62] |
| $In^{3+}$ | [2, 12, 26, 58, 60, 63, 84, 85] | [59, 62, 77, 86] |
| $La^{3+}$ | [58, 63] | [62] |
| $Lu^{3+}$ | [12, 58] | |
| $Nd^{3+}$ | [2, 58, 63, 65] | [62, 77] |
| $Pr^{3+}$ | [60] | |
| $Rh^{3+}$ | [87] | |
| $Sc^{3+}$ | [12, 26, 58, 60, 63, 67, 88] | [59, 62, 77] |
| $Sm^{3+}$ | [58, 60, 67] | [62] |
| $Sn^{3+}$ | [89] | |
| $Tm^{3+}$ | [58, 60, 63, 68] | |
| $Yb^{3+}$ | [60, 63, 72, 90–92] | |
| $Co^{2+}$ | [66] | |
| $Fe^{2+}$ | [71, 72] | |
| $Mg^{2+}$ | [63] | |
| $Zn^{2+}$ | [93] | |

through the incorporation of oxygen vacancies:

$$2\,BaO + DOP_2O_3 \rightarrow 2\,Ba_{Ba}^{\times} + 2\,DOP_{Zr}' + 5\,O_O^{\times} + V_O^{\bullet\bullet}. \tag{5.1}$$

The dopant occupies the B-site and oxygen vacancies are formed on oxygen sites. There are several studies on A-site doping but this is not taken into account in this work.[94] Thereby $x$ in $BaZr_{1-x}DOP_xO_{3-\frac{x}{2}}V_{O\frac{x}{2}}^{\bullet\bullet}$ is the dopant fraction. It is limited between $0 \leq x \leq 1$ but the highest dopant fraction experimentally found for yttrium doping is 0.4.[95] The charge neutrality for the doped oxide can be set up to:

$$2\,[V_O^{\bullet\bullet}] = [DOP_{Zr}']. \tag{5.2}$$

**Table 5.2: Species occupying the sites in $BaZrO_3$ before (first row) and after doping (second row).** The numbers refer to the occupancy of one unit cell.

| A-site | B-site | Oxygen site | Interstitial site |
|---|---|---|---|
| 1 $Ba_{Ba}^{\times}$ | 1 $Zr_{Zr}^{\times}$ | 3 $O_O^{\times}$ | - |
| 1 $Ba_{Ba}^{\times}$ | $(1-x)$ $Zr_{Zr}^{\times}$; $x$ $DOP_{Zr}^{'}$ | $(3-\frac{x}{2})$ $O_O^{\times}$; $\frac{x}{2}$ $V_O^{\bullet\bullet}$ | - |

Square brackets ([...]) indicate site fractions of the respective species. After doping, $BaZrO_3$ is exposed to a water containing environment. This can be, for example, wet air, wet $H_2$ or wet Ar. Thereby, water is incorporated into the crystal, filling (parts of) the oxygen vacancies with a protonic species:

$$H_2O + V_O^{\bullet\bullet} \rightleftharpoons O_O^{\times} + 2\,H_i^{\bullet} \tag{5.3}$$

Here, the degree of hydration $\alpha$ is defined as the quotient of proton and dopant ion concentration:

$$\alpha = \frac{[H_i^{\bullet}]}{[DOP_{Zr}^{'}]}. \tag{5.4}$$

It is limited between $0 \leq \alpha \leq 1$ and although it is experimentally difficult, it is possible to come close to values of $\alpha = 1$.[96] This is called the *fully hydrated case*. The contrary case with $\alpha = 0$, is called the *dry case*.

**Table 5.3: Species occupying the sites in $BaZrO_3$ after the incorporation of water.** The numbers refer to the occupancy of one unit cell.

| A-site | B-site | Oxygen site | Interstitial site |
|---|---|---|---|
| 1 $Ba_{Ba}^{\times}$ | $(1-x)$ $Zr_{Zr}^{\times}$; $x$ $DOP_{Zr}^{'}$ | $(3-\frac{x}{2}+\alpha\frac{x}{2})$ $O_O^{\times}$; $(\frac{x}{2}-\alpha\frac{x}{2})$ $V_O^{\bullet\bullet}$ | $(\alpha x)$ $H_i^{\bullet}$ |

The charge neutrality equation (eq. 5.2) changes to:

$$2\,[V_O^{\bullet\bullet}] + [H_i^{\bullet}] = [DOP_{Zr}^{'}] \tag{5.5}$$

In their work, Lindman *et al.*[97] stated that electron hole polarons can have a contribution to the conductivity in acceptor-doped $BaZrO_3$. Therefore, polarons have to be taken into account in the defect model although they are more of an outlook in this work. Polarons are built, when oxygen vacancies are filled with pure oxygen:

$$\frac{1}{2}O_2 + V_O^{\bullet\bullet} + O_O^{\times} \rightleftharpoons 2\,O_O^{\bullet} \tag{5.6}$$

In $BaZrO_3$, polarons tend to localize at an oxygen ion. These *small polarons* can be written as $O_O^{\bullet}$. A degree of polaronization $\beta$ is defined analogous to $\alpha$:

$$\beta = \frac{[O_O^{\bullet}]}{[DOP_{Zr}^{'}]}. \tag{5.7}$$

**Table 5.4: Species occupying the sites in $BaZrO_3$ after polarons are formed.** The numbers refer to the occupancy of one unit cell.

| A-site | B-site | Oxygen site | Interstitial site |
|---|---|---|---|
| 1 $Ba_{Ba}^{\times}$ | $(1-x)$ $Zr_{Zr}^{\times}$; $x$ $DOP_{Zr}^{'}$ | $(3-\frac{x}{2}+\alpha\frac{x}{2})$ $O_O^{\times}$; $(\frac{x}{2}-\alpha\frac{x}{2})$ $V_O^{\bullet\bullet}$; $(\beta\frac{x}{2})$ $O_O^{\bullet}$ | $(\alpha x)$ $H_i^{\bullet}$ |

It is limited between $0 \leq \beta \leq 1$ with the additional constraint that $(\alpha + \beta) \leq 1$.
Now, the charge neutrality equation (eq. 5.5) changes to:

$$2\,[V_O^{\bullet\bullet}] + [H_i^{\bullet}] + [O_O^{\bullet}] = [DOP_{Zr}^{'}] \tag{5.8}$$

Protons do not have regular lattice sites but their interstitial sites are well defined. Around every oxygen site, there are four positions, protons can occupy. Depending on the dopant environment, they are around 1 Å away from the oxygen in the Zr-O-planes. They were found via structure relaxations with DFT and in agreement with literature data.[3,13,86]

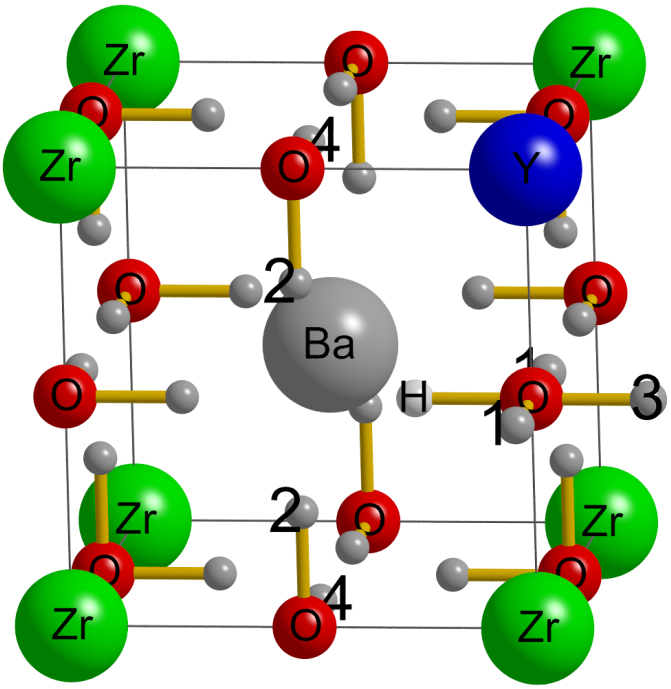


**Figure 5.1: The unit cell of $BaZrO_3$ with all the possible proton positions (grey), but only one position is occupied by a proton (white).** Zirconium is shown in green, yttrium in blue and oxygen in red. The yellow lines are simply a guide to the eye. The numbers refer to the *n*-th neighbourhood to the proton.

With protons, oxygen vacancies and polarons, up to three mobile species have to be considered. To

perform KMC calculations, a pair interaction model that uses interaction energies between every mobile and immobile species, is used. Within this model, the energy of the whole lattice can be calculated as a sum of pair interactions between the defects involved in the calculation. Following the method of Grieshammer *et al.*,[98] on the example of fully hydrated yttrium-doped $BaZrO_3$, the energy of one configuration $E_{conf}$ is calculated according to:

$$E_{conf} = \sum_{i=1}^{a} N^{i}_{H_i^{\bullet}-H_i^{\bullet}} \cdot \Delta E^{i}_{H_i^{\bullet}-H_i^{\bullet}} + \sum_{i=1}^{b} N^{i}_{H_i^{\bullet}-Y'_{Zr}} \cdot \Delta E^{i}_{H_i^{\bullet}-Y'_{Zr}} + \sum_{i=1}^{c} N^{i}_{Y'_{Zr}-Y'_{Zr}} \cdot \Delta E^{i}_{Y'_{Zr}-Y'_{Zr}}. \qquad (5.9)$$

Here, $N^{i}_{A-B}$ and $\Delta E^{i}_{A-B}$ are the number and interaction energy of the defect pair A–B in the i-th neighbourhood. The energy of one configuration in the dry case is calculated analogously but with interaction energies between other species. Table 5.5 gives an overview over the interactions needed for each specific simulation. There are some changes and assumptions made to this general procedure which are discussed later in this chapter. Interaction energies between immobile species (for example $\Delta E^{i}_{Y'_{Zr}-Y'_{Zr}}$) are special, because their contribution to the energy of the initial state is exactly equal to the energy of the final state.

**Table 5.5: Pair interactions needed for the KMC simulations.** The upper left rounded rectangle marks the pair interactions needed for the fully hydrated case (Chapter 6). The other one marks analogously the interactions for the dry case (Chapter 7). The interactions in both rectangles and the $H_i^{\bullet}$ – $V_O^{\bullet\bullet}$ interaction is needed for calculations with mobile protons and oxygen vacancies (Chapter 9) and all interactions marked with "X" would be needed for the full calculation with three mobile species.

| | $H_i^{\bullet}$ | $DOP'_{Zr}$ | $V_O^{\bullet\bullet}$ | $O_O^{\bullet}$ |
|---|---|---|---|---|
| $H_i^{\bullet}$ | X | X | X | X |
| $DOP'_{Zr}$ | | X | X | X |
| $V_O^{\bullet\bullet}$ | | | X | X |
| $O_O^{\bullet}$ | | | | X |

All interaction energies were calculated utilizing DFT as a function of the distance of the respective species. For example, calculating the interaction energy between $H_i^{\bullet}$ and $DOP'_{Zr}$, the dopant is held fixed in the supercell and the proton is set to another site at another distance for every calculation. It is assumed that for distances larger than 10 Å, there is no more interaction between defects. Therefore, the interaction energy calculated for the largest distance within these 10 Å is set to 0.0 eV. Normally, for the calculation of pair interactions, highly diluted dopant ions were assumed resulting in one dopant ion and one proton in the cell at a time. Later, there are corrections made that result from interactions between more than two defects (see *deep trapping* later in this work). Additionally, for all calculations of interaction energies, finite-size corrections after Makov and Payne are carried out.[44] In this process, the interaction energy is plotted against the reciprocal of the cell volume $V_{cell}$ and then the extrapolation $1/V_{cell} \rightarrow 0$ yields the interaction energy.
The interaction energy between $H_i^{\bullet}$ and $Y'_{Zr}$ is shown in figure 5.2. One can differentiate between

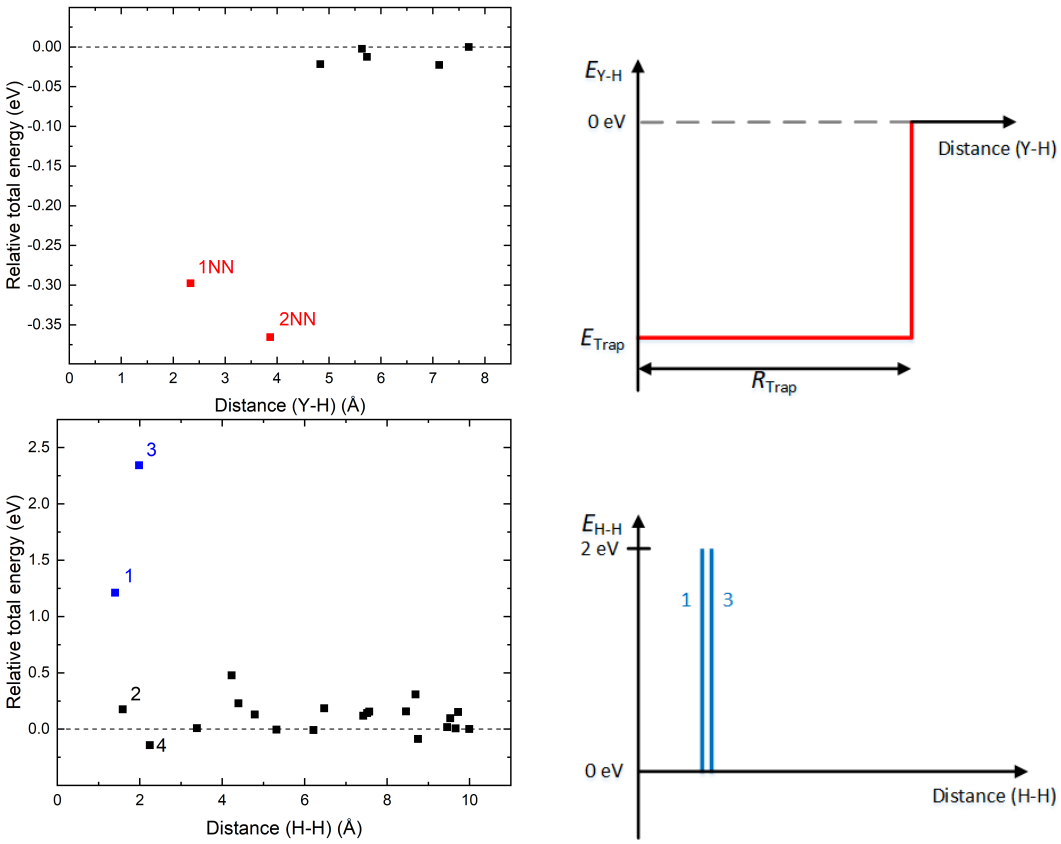


**Figure 5.2: Interaction energies between different defects and their adaption in the energy model.**[13] Top left: The finite-size corrected relative total energy of a supercell that contains one yttrium ion and one proton at different distances. Energies are related to the energy that corresponds to the largest distance, which is set to 0.0 eV. The yttrium-proton neighbourhood refers to the numbers in figure 5.3. Top right: For the energy model used in the KMC simulations, the obtained DFT energies are simplified to a trapping zone around the dopant ion (with a radius $R_{trap}$ and a depth $E_{trap}$). Bottom left: The finite-size corrected relative total energy of a supercell that contains two protons at different distances. The energies are related to the energy of the position with the largest distance, which is set to 0.0 eV. The numbers refer to positions in figure 5.3. Bottom right: For the energy model used in the KMC simulations, the obtained DFT energies are simplified. Only interaction energies depicting protons at the same oxygen ion (see positions 1 and 3 in fig. 5.1) are used.

two regions: one region close to the yttrium ion with lowered energy that includes protons on first (1NN) and second (2NN) nearest neighbourhood (compare the numbers in fig. 5.3). From 3NN on, in the second region, the proton no longer interacts with the yttrium ion. The first region is called *trapping zone* because a proton trying to move out of this zone has to overcome an additional amount of energy, therefore, it is trapped. The trapping zone of yttrium has a diameter of about 4.3 Å and the trapping energy on 1NN is −0.3 eV and −0.37 eV on 2NN, respectively.

In the KMC model, this interaction is simplified to a two-state model: The first state is the untrapped

proton far away from the dopant, whereas a trapping zone with radius $R_{trap}$ and depth $E_{trap}$ is introduced and a basis set of parameters with $R_{trap}$ = 4.3 Å and $E_{trap}$ = −0.3 eV is chosen. A strength of the model is the possibility to vary both. Doing so, this no longer represents the physical reality of yttrium dopants but it enables deep insights into the behaviour of the system.

This trapping effect is of great importance for the ionic conductivity of protons in doped $BaZrO_3$. Therefore, sets of DFT calculations were performed to investigate the interaction of one proton with many different dopants.[57]

Calculating the interaction energy between two protons analogously, it was found that two protons located at the same oxygen ion repel each other strongly (see Fig. 5.2). This is easy to understand in the sense of Coulomb's law and the equal charge of two protons. The interaction energy is 1.25 eV and 2.25 eV, respectively (Fig. 5.2).

Remarkably, the interaction cannot simply be interpreted as a function of the distance. Two protons located closely to each other but on different oxygen ions (position 2 in Fig. 5.2) repel each other hardly at all. There are even light attractive cases at all distances (position 4 in Fig. 5.2).

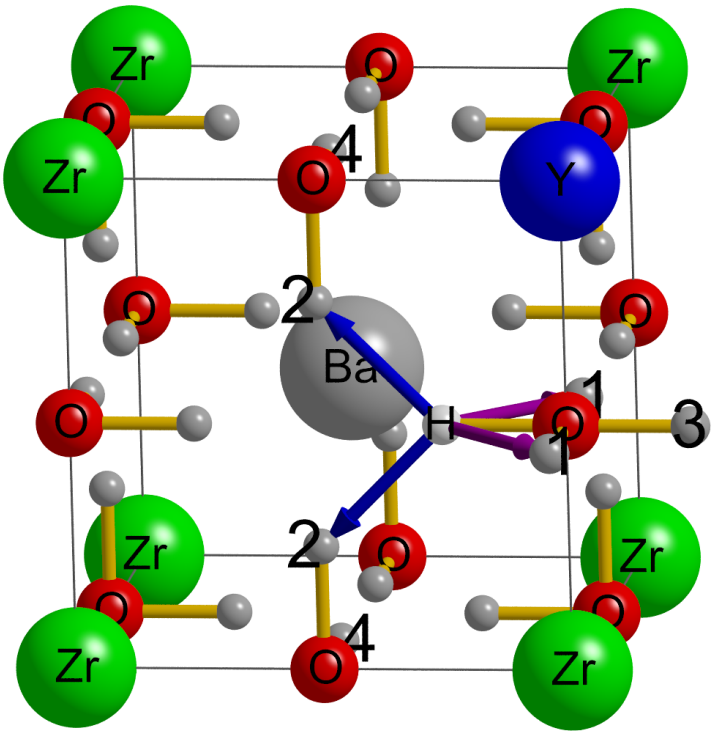


**Figure 5.3: The unit cell of $BaZrO_3$ with all the possible proton positions (grey), but only one position is occupied by a proton (white).**[13] Zirconium is shown in green, yttrium in blue and oxygen in red. The yellow lines are simply a guide to the eye. The numbers refer to the *n*-th neighbourhood to the proton. The four arrows show exemplarily the four possible jumps the proton can make. The two purple arrows show reorientation jumps around the oxygen ion. The two blue arrows show two translation jumps from the vicinity of one oxygen ion to another.

This cannot be understood in terms of just charge repulsion. Here, the tilting of the oxygen octahedra influences the interaction. A proton on an interstitial position slightly deflects the oxygen ion next to it. This causes two oxygen ions on 1NN to fill up the space and be moved closer to the proton. This effect continues although it weakens with increasing distance. Two protons placed in the same supercell can amplify or weaken this effect depending on their position. This influences the interaction energy and makes it hard to investigate. In the KMC model, therefore only the two strongest "peaks" were included. This is a simplification that can be removed later on if the influence of the oxygen octahedron tilting is fully understood.

The fully hydrated case with the simplifications mentioned above will be referred to as the *simplified model*.

For KMC simulations, not only interaction energies, but also migration energies are needed. These are the energy barriers between initial and final states of ion jumps.[98] Migration energies are calculated by means of CI-NEB calculations within DFT. In principal it would be necessary to calculate migration energies for protons and oxygen vacancies in every possible lattice configuration. Due to the large number of configurations and therefore the large amount of (computation) time that would be necessary for this project, this is impossible. Therefore, only B-sites in first nearest neighbourhood (1NN) to the initial or final position of one proton jump (and analogously oxygen vacancy jump) are permuted explicitly. The migration energy of configurations that are formed due to defects further away are modelled by combining the calculated migration energies and pair interactions according to Grieshammer *et al.*[98] as shown in figure 5.4.

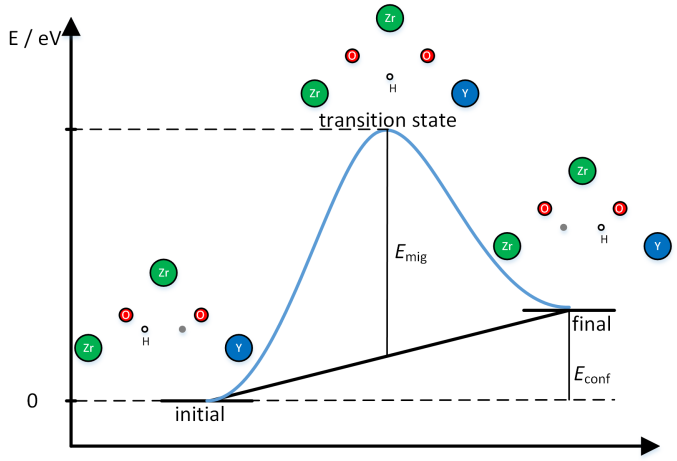


**Figure 5.4: Basic structure of the energy model used for the KMC simulations.**[98] A combination of pair interactions ($E_{conf}$) and a migration energy ($E_{mig}$) is used to calculate the resulting energy barrier of each respective ion jump. Although drawn similar, there is a difference between $E_{conf}$ and $E_{trap}$ in figure 5.2. The trapping energy is one possible contribution to $E_{conf}$, which is the sum out of many interaction energies. $E_{conf}$ can be positive or negative, while no example was found where $E_{trap}$ was positive on 1NN.

**Table 5.6: Proton migration energies for reorientation jumps.** All three possible permutations of the occupation of the zirconium sites in the first nearest neighbourhood of the initial and final positions of the reorientation jump. Zirconium is shown in green, yttrium in blue, oxygen in red and the proton in white. The corresponding migration energies were calculated explicitly by means of DFT and they were finite-size corrected.

| Configuration | Name | $E_{mig}$ in eV |
|---|---|---|
| 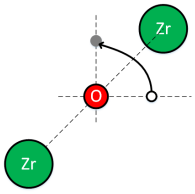 | R-Zr-Zr | 0.15 |
| 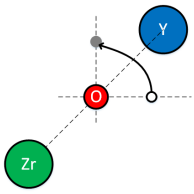 | R-Zr-Y | 0.22 |
| 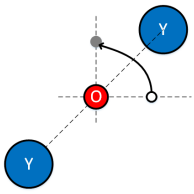 | R-Y-Y | 0.13 |

Every proton in $BaZrO_3$ moves from one site to another through an energetically unfavourable transition state. Thereby, protons do have two different jump possibilities: reorientation (purple arrows in Fig. 5.3) and translation jumps (blue arrows in Fig. 5.3). One reorientation jump leads a proton to one of two other interstitial positions around the same oxygen ion. They have a length of about 1.4 Å and a typical migration energy of 0.15 eV. Translation jumps on the contrary, lead a proton to the nearest position on a neighbouring oxygen ion. These jumps are about 1.6 Å long with a typical migration energy of 0.41 eV. Longer translation jumps are also conceivable, but the shortest longer jump has a migration energy of at least 3.31 eV, which makes this jump very unlikely. They are therefore not included in the KMC model.

Although typical values are given, the migration energies depend strongly on the dopant environment. Here, the difference to the experiment has to be highlighted: Experimentally, there is only one macroscopic activation energy of proton conductivity, while in the model there are several microscopical migration energies. Through the KMC simulations, the activation energy can be determined.

For proton jumps, eleven different configurations are calculated explicitly (see Tab. 5.6 and 5.7). In both cases, the occupation of B-positions in 1NN to start or end position are permuted resulting in three reorientation and eight translation jump configurations. Additionally, every migration en-

**Table 5.7: Proton migration energies for translation jumps.** All eight possible permutations of the occupation of the zirconium sites in the first nearest neighbourhood of the initial and final positions of the translation jump. Zirconium is shown in green, yttrium in blue, oxygen in red and the proton in white. The corresponding migration energies were calculated explicitly by means of DFT and they were finite-size corrected.

| Configuration | Name | $E_{mig}$ in eV | Configuration | Name | $E_{mig}$ in eV |
|---|---|---|---|---|---|
| 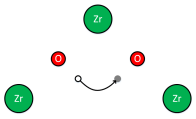 | Zr-Zr-Zr | 0.41 | 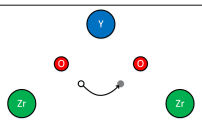 | Zr-Y-Zr | 0.22 |
| 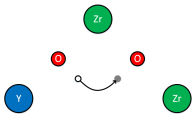 | Y-Zr-Zr | 0.35 | 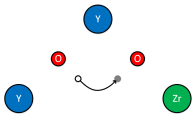 | Y-Y-Zr | 0.37 |
| 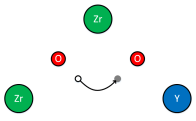 | Zr-Zr-Y | 0.35 | 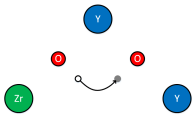 | Zr-Y-Y | 0.37 |
| 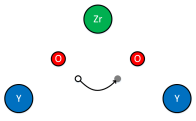 | Y-Zr-Y | 0.55 | 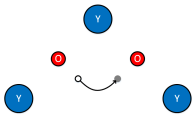 | Y-Y-Y | 0.66 |

ergy is calculated in at least three supercells of different sizes for the finite-size correction (see Figs. A.22, and A.23 in the appendix). The nomenclature used is explained in tables 5.6 and 5.7.
All migration energies for reorientation jumps are similar and very low. This causes the protons to rotate around the oxygen ions most of the time because these jumps are accepted very likely. For translation jumps, the differences between different configurations are larger. In particular, the Zr-Y-Zr jump with the migration energy of 0.22 eV plays a crucial role in the acceleration of protons inside of the trapping zone. Most jumps benefit from near yttrium dopants except the Y-Zr-Y and Y-Y-Y configurations.

## 5.2 Attempt frequencies

To calculate the attempt frequencies in our work (SI in [13]), we made an approximation to calculate the attempt frequencies by displacing the migrating proton out of the ground state along the migration pathway. If it is assumed, that all neighbouring atoms are frozen the attempt frequency can be calculated using the harmonic oscillator:

$$E_{el}^{0} = \frac{1}{2}kx^{2} + E_{el,x=0}^{0}. \tag{5.10}$$

With x being the displacement coordinate. The attempt frequency is then given by:

$$\nu_0 = \frac{\sqrt{k/m}}{2\pi}. \tag{5.11}$$

We calculated the attempt frequency for reorientation jumps in undoped $BaZrO_3$ to 0.776 $\cdot 10^{13}$ Hz and the attempt frequency for translation jumps to 1.243 $\cdot 10^{13}$ Hz. Both values are used in all KMC calculations including proton reorientation and translation jumps. Our results show some differences to literature values: Björketun *et al.*[86] calculated the attempt frequency for proton reorientation jumps to 2.7 $\cdot 10^{13}$ Hz and for proton translation jumps to 10.4 $\cdot 10^{13}$ Hz. Both values are significantly higher.
Small deviations in the migrating pathway during the DFT calculations, though, have an influence on the calculated value and could explain the discrepancy. Nevertheless, the attempt frequency is only a scaling factor[49] and should not influence general trends.
For oxygen ion jumps and later vehicle jumps, the attempt frequency was approximated with the Debye frequency of $10^{13}$ Hz.

## 5.3 Oxygen Vacancies in Yttrium-doped $BaZrO_3$

Interaction energies between one oxygen vacancy and another defect are calculated analogously (Fig. 5.5). The interaction between one oxygen vacancy and one yttrium dopant revealed that there is also a trapping zone for oxygen vacancies around every yttrium dopant (Fig. 5.6, left). It is −0.36 eV deep (on 1NN) and it ranges up to and including 3NN with energies of −0.28 eV (2NN) and −0.07 eV (3NN), respectively. Again, the same procedure as before was used to build the pair interaction model with defect interactions according to table 5.5 (see figure 5.5 for illustration).

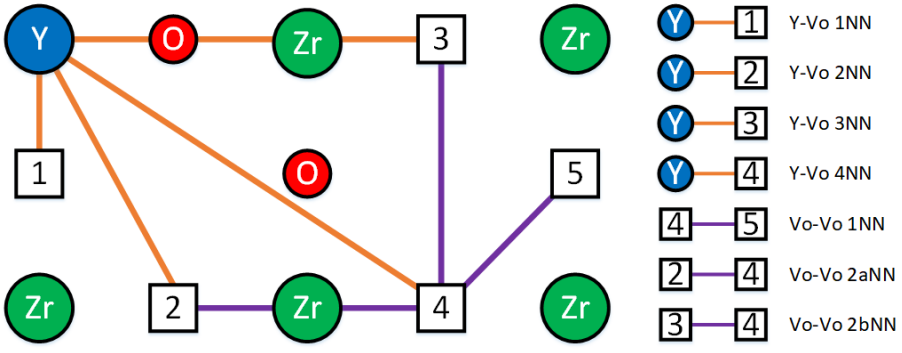


**Figure 5.5: Projection of a supercell of 2×1×1 $BaZrO_3$.** Yttrium is shown in blue, zirconium in green, oxygen in red and oxygen vacancies as black squares. The interaction energies that are most important for the KMC simulations are shown. For each interaction the distance is described in terms of neighbourhood. There are two interactions for Vo-Vo 2NN that are denoted as 2aNN (with zirconium in between) and 2bNN (without zirconium in between).

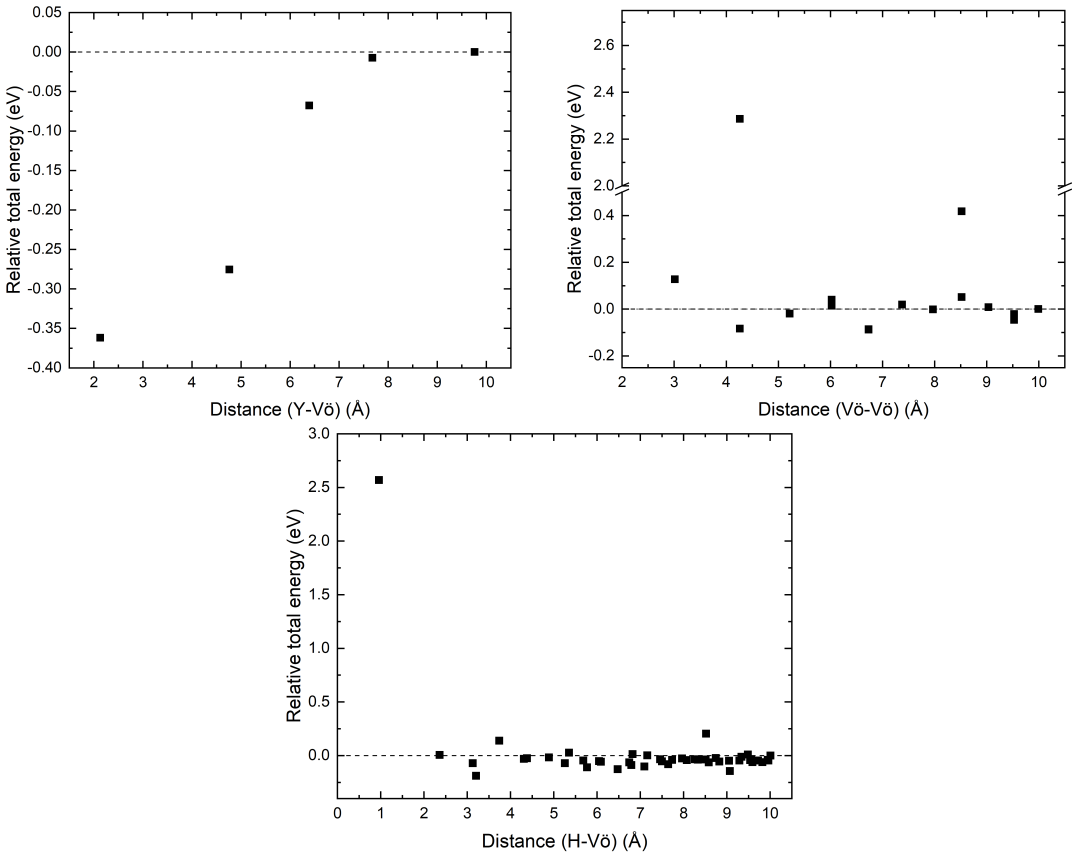


**Figure 5.6: Interaction energies between oxygen vacancies and other defects.** Left: The relative total energy of a supercell that contains one yttrium ion and one oxygen vacancy at different distances. Right: The relative total energy of a supercell that contains two oxygen vacancies at different distances. Bottom: The relative total energy of a supercell that contains one oxygen vacancy and one proton at different distances. In all three cases, the energies are related to the energy of the position with the largest distance, which is set to zero.

This pair interaction model was validated as follows. The relative total energies of different configurations with one oxygen vacancy and two yttrium dopants were predicted with the model and then calculated within DFT. The model fits well with one exception: The Y-$V_O^{\bullet\bullet}$-Y configuration was found to be energetically lower by 0.22 eV than predicted by the model (see Tab. 5.8). Therefore, an additional amount of energy was subtracted for this configuration. This is called "deep trapping" in the following. It has to be mentioned, that all values used in our model were finite-size corrected in contrast to the calculation of the Y-$V_O^{\bullet\bullet}$-Y configuration. An discrepancy of 0.22 eV could emerge from this. Therefore, we compare the – finite size corrected – migration energies of the oxygen vacancy jumps in the Y-Y-Zr and Z-Y-Y configuration with each other (Tab. 5.9). In the initial configuration of the Y-Y-Zr jump, the oxygen vacancy is in 1NN to both yttrium dopant ions. In the

final position of this jump it is in 1NN to one yttrium dopant and in 2NN to the other. Following the model, the difference in the migration energies between jump (Y-Y-Zr) and back jump (Zr-Y-Y) should be the energy difference between 1NN and 2NN and therefore 0.08 eV. The calculations however, show a difference of (1.04 eV – 0.78 eV =) 0.26 eV and give additional arguments for deep trapping.

**Table 5.8: Validation of the pair interaction model.** Comparison between the calculated interaction energies for a cell containing two yttrium dopants and one oxygen vacancy (DFT) with the energies predicted by the model (Model). Vo-Y1, Vo-Y2 and Y1-Y2 depict the neighbourhood of the respective species. Interaction energies from figure 5.6 are used and an additional repulsive interaction between Y1 and Y2 in 1NN of 0.2 eV that was calculated by means of DFT. All energies are standardized on the case where all defects are far away from each other (meaning 10 Å or more).

| $V_O^{\bullet\bullet}$-Y1 | $V_O^{\bullet\bullet}$-Y2 | Y1-Y2 | *E*(Model) in eV | *E*(DFT) in eV | Δ*E* in eV |
|---|---|---|---|---|---|
| 1NN | 1NN | 1NN | −0.52 | −0.74 | 0.22 |
| | 2NN | 1NN | −0.44 | −0.48 | 0.04 |
| | 2NN | 2NN | −0.63 | −0.65 | 0.02 |
| | far away | far away | −0.36 | −0.36 | 0.00 |
| 2NN | 2NN | 1NN | −0.36 | −0.33 | −0.03 |
| | 2NN | 2NN | −0.55 | −0.47 | −0.08 |
| | 2NN | 3NN | −0.58 | −0.57 | −0.01 |
| | 2NN | 4NN | −0.48 | −0.35 | −0.13 |
| | 2NN | 5NN | −0.56 | −0.36 | −0.2 |
| | far away | 3NN | −0.3 | −0.33 | 0.03 |
| far away | far away | far away | 0 | 0 | |

The interaction between two oxygen vacancies (Fig. 5.6, right) cannot be understood in terms of Coulomb's law only. Again, one reason lies in the distortion of the oxygen octahedra a vacancy causes. Adding another vacancy, this effect can be intensified or attenuated, depending on its position.

Additionally, another effect predominates strongly. Looking at the distance of 4.23 Å, one sees two interaction energies. This can be traced back to two different configurations that are possible with the same distance between both vacancies one with no ion between the vacancies and one with one zirconium ion between them. In the first case the energy is low but in the second case, there is a very high repulsive interaction energy of 2.3 eV. A similar effect was found in yttrium-doped ceria.[98]. This effect is repeated after one more unit cell at 8.46 Å. In the structure with one zirconium ion between both vacancies, the distortion of the oxygen octahedra is very small due to symmetry reasons, which contributes to the very high site energy of about 0.4 eV.

The interaction between one oxygen vacancy and one proton can be understood easily (Fig. 5.6).

There is a very strong repulsive interaction at the shortest distance, making it unlikely for a proton to be located next to an oxygen vacancy. This coincides with the knowledge that protons have to be bound to an oxygen ion. The interaction energy between oxygen vacancies and protons is used for calculations in partially hydrated acceptor-doped $BaZrO_3$ (chapter 9).
Migration energies for oxygen vacancies are calculated by means of CI-NEB analogous to those for protons. In the case of oxygen vacancies, there are eight possible translation jumps. Reorientation jumps cannot occur and longer translation jumps are excluded for the same reason as above. All migration energies are calculated in three differently sized supercells and finite-size corrected. They are listed in table 5.9. The barriers vary between 0.46 and 1.16 eV depending on the dopant configuration.

**Table 5.9: Oxygen vacancy migration energies for translation jumps.** All eight possible permutations of the occupation of the zirconium sites in the first nearest neighbourhood of the initial and final positions of the oxygen vacancy translation jump. Zirconium is shown in green, yttrium in blue, oxygen in red and the oxygen vacancy is a square. The corresponding migration energies were calculated explicitly by means of DFT and they were finite-size corrected.

| Configuration | Name | $E_{mig}$ in eV | Configuration | Name | $E_{mig}$ in eV |
|---|---|---|---|---|---|
| 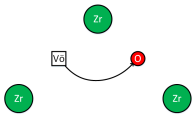 | Zr-Zr-Zr | 0.66 | 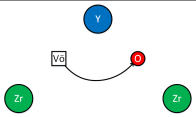 | Zr-Y-Zr | 1.16 |
| 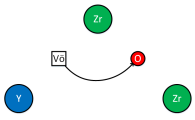 | Y-Zr-Zr | 0.54 | 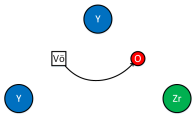 | Y-Y-Zr | 1.04 |
| 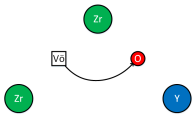 | Zr-Zr-Y | 0.46 | 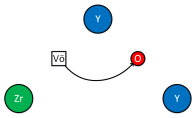 | Zr-Y-Y | 0.78 |
| 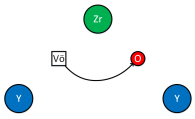 | Y-Zr-Y | 0.64 | 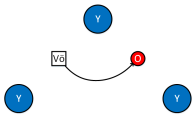 | Y-Y-Y | 0.88 |

Oxygen vacancy jumps in the Zr-Zr-Zr configuration, meaning in pure $BaZrO_3$, have a migration energy of 0.66 eV. Stokes *et al.* calculated the migration energy of oxygen vacancies in $BaZrO_3$ to 0.65 eV.[99] This fits perfectly with our results but it does not depict the doped configurations where migration barriers differ. One trend is remarkable: If zirconium position 2 (at the top of the triangle) is doped with yttrium, the migration energy is much larger (up to 0.5 eV) than in the corresponding configuration with zirconium. The reason lies in the higher ionic radius of yttrium: $r_Y = 0.90$ Å and $r_{Zr} = 0.72$ Å[100] and therefore, the distance between the oxygen ion and the ion on Zr-Position 2 in the transition state is about 0.13 Å larger when position 2 is occupied with yttrium.

Accordingly, the "jump window", between yttrium and the two barium above and below the jump path becomes smaller, leaving less space for the jumping oxygen ion, which enlarges the migration energy.

## 5.4 Other dopants

Although yttrium is the most common dopant ion for $BaZrO_3$, it is not the only one. In this work, interactions with four more dopants are investigated further following one work of Björketun *et al.*:[59] gallium, gadolinium, indium and scandium.

### Defect interactions

Interaction energies between those dopants and both mobile species are calculated by means of DFT and shown in figure 5.7. Due to the high computational demands, no finite-size correction could be applied for these interaction energies. They are calculated in the 4 × 4 × 4 super cell, which which has proven to be reliable.

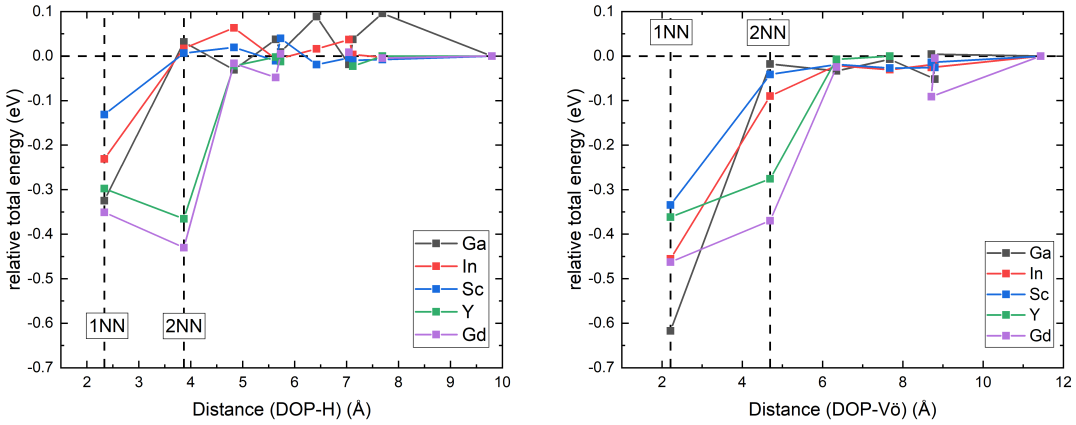


**Figure 5.7: Interaction energies between five different dopant ions and protons or oxygen vacancies, respectively.** Left: The relative total energy of a supercell that contains one dopant ion and one proton at different distances. Right: The relative total energy of a supercell that contains one dopant ion and one oxygen vacancy at different distances. In both cases, the energies are related to the energy of the position with the largest distance, which is set to zero. Calculations were performed in a 320-atom supercell.

The dopants – above all – differ in their trapping behaviour. Gallium, indium and scandium trap oxygen vacancies as well as protons only in 1NN to the dopant whereas yttrium and gadolinium trap both in 1NN and 2NN. When proton trapping on 2NN occurs, it is stronger than on 1NN but not the oxygen vacancy trapping. This behaviour correlates with the dopants ionic radius. Ions that trap only in 1NN have a small radius ($r_{Ga}$ = 0.62 Å, $r_{Sc}$ = 0.745 Å and $r_{In}$ = 0.80 Å) whereas yttrium and gadolinium have large radii ($r_{Y}$ = 0.90 Å and $r_{Gd}$ = 0.938 Å) compared to zirconium

($r_{Zr}$ = 0.72 Å).[100] In contrast to the radius, no general trend for the depth of the trapping zone can be seen. It seems that the small gallium traps both mobile species very deep while indium and scandium trap protons moderately and trap oxygen vacancies comparable to yttrium. Gadolinium is larger and its traps are deeper than those around yttrium.
In the model used in the subsequent KMC simulations, all five dopant ions are incorporated but in a simplifying approach, the interaction energy is artificially smoothed, which means that no interaction energies besides the trapping are incorporated.

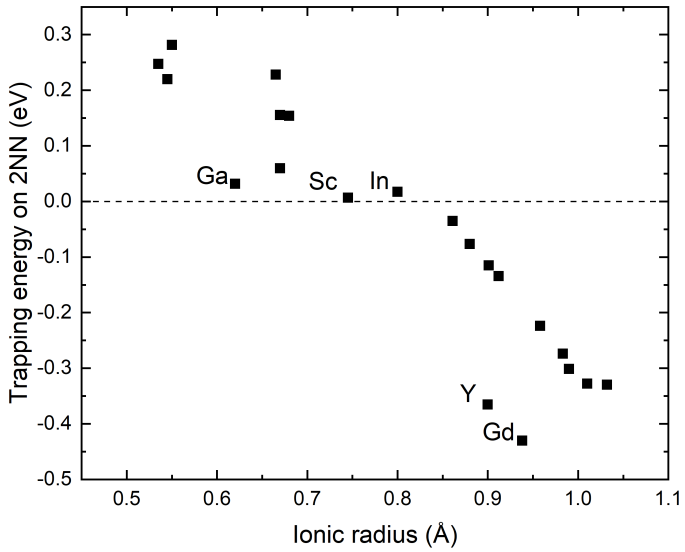


**Figure 5.8: Proton trapping energy on 2NN for different dopant ions.** The order of the values from low ionic radii to high ionic radii is: Al, Co, Fe, Ga, Rh, Mn, Ti, Ru, Sc, In, Lu, Tm, Y, Ho, Dy, Gd, Sm, Nd, Pr, Ce and La. For the sake of clarity only Ga, Sc, In, Y and Gd have a caption. The exact ionic radii and trapping energies can be taken from table 5.10.

During his research project, Jordy Peulen[57] calculated interaction energies between dopants and protons for a lot more dopant ions (see Tab. 5.10). It was found that all tested dopant ions trap protons in 1NN but the behaviour on 2NN differs. Some dopants, like yttrium and most of the lanthanoids, trap protons on 2NN with different depths. These dopants all have in common that their ionic radii are very large. Some ions, like gallium, scandium, indium and aluminium, do not trap protons on 2NN, the trapping energy is around 0 eV and some ions even repel protons on 2NN. To stay in the same language, these dopant ions have an "anti-trapping" in 2NN, a positive energy barrier that has to be overcome for protons to come close to the ion. A clear trend can be seen when plotting this against the ionic radius of the dopant ions (see Fig. 5.8): The larger the ion, the deeper the trapping in 2NN. For ions with a radius below 0.7 Å it is very likely to have "anti-trapping" on 2NN. This energy barrier is in the order of magnitude of migration energies for protons. It is interesting, whether these barriers keep protons out of the trapping zones or on the contrary strengthen the trapping.

**Table 5.10: The relative total energy of a supercell that contains one dopant ion and one proton at different distances.** The energies are related to the energy of the position with a distance larger than 10 Å, which is set to 0.0 eV. Calculations were performed in a 320-atom supercell. Graphics for every ion are included in the appendix.

| Ion | $R_{ion}$ in Å | $E_{trap,1NN}$ in eV | $E_{trap,2NN}$ in eV | $E_{trap,3NN}$ in eV |
|---|---|---|---|---|
| $Al^{3+}$ | 0.535 | −0.28 | 0.25 | 0.10 |
| $Co^{3+}$ | 0.545 | −0.29 | 0.22 | 0.05 |
| $Fe^{3+}$ | 0.55 | −0.21 | 0.28 | 0.12 |
| $Ga^{3+}$ | 0.62 | −0.32 | 0.03 | −0.03 |
| $Rh^{3+}$ | 0.665 | −0.06 | 0.23 | 0.06 |
| $Mn^{3+}$ | 0.67 | −0.06 | 0.16 | 0.78 |
| $Ti^{3+}$ | 0.67 | −0.25 | 0.06 | 0.00 |
| $Ru^{3+}$ | 0.68 | −0.03 | 0.15 | −0.01 |
| $Sc^{3+}$ | 0.745 | −0.13 | 0.01 | 0.02 |
| $In^{3+}$ | 0.8 | −0.23 | 0.02 | 0.06 |
| $Lu^{3+}$ | 0.861 | −0.10 | −0.04 | 0.03 |
| $Tm^{3+}$ | 0.88 | −0.10 | −0.08 | 0.02 |
| $Y^{3+}$ | 0.9 | −0.30 | −0.37 | −0.02 |
| $Ho^{3+}$ | 0.901 | −0.10 | −0.11 | 0.01 |
| $Dy^{3+}$ | 0.912 | −0.10 | −0.13 | 0.01 |
| $Gd^{3+}$ | 0.938 | −0.35 | −0.43 | −0.02 |
| $Sm^{3+}$ | 0.958 | −0.10 | −0.22 | −0.03 |
| $Nd^{3+}$ | 0.983 | −0.09 | −0.27 | −0.06 |
| $Pr^{3+}$ | 0.99 | −0.10 | −0.30 | −0.07 |
| $Ce^{3+}$ | 1.01 | −0.10 | −0.33 | −0.09 |
| $La^{3+}$ | 1.032 | −0.10 | −0.33 | −0.09 |

## Proton migration energies

Migration energies for proton jumps are calculated for gallium-, scandium-, indium- and gadolinium-doped $BaZrO_3$ as described above and the tables 5.6 and 5.7 are expanded in tables 5.11 and 5.12.

All proton migration energies for reorientation jumps lay in a narrow range of values between 0.07 and 0.22 eV. This jump is the shortest and therefore, like in yttrium-doped $BaZrO_3$, protons will rotate around oxygen ions very easily and mostly independent from the dopant ion.

Migration energies for proton translation jumps differ much more. They range from 0.04 eV to 1.05 eV, depending on the dopant configuration. For dopants that trap protons in 1NN only, the

**Table 5.11: Proton migration energies for reorientation jumps.** All three possible permutations of the occupation of the zirconium sites in the first nearest neighbourhood of the initial and final positions of the reorientation jump. Zirconium is shown in green, the dopant in blue, oxygen in red and the proton in white. The corresponding migration energies were calculated explicitly by means of DFT and finite-size corrected.

| Dopant | | $Ga^{3+}$ | $Sc^{3+}$ | $In^{3+}$ | $Y^{3+}$ | $Gd^{3+}$ |
|---|---|---|---|---|---|---|
| Ionic radius | | 0.62 Å | 0.745 Å | 0.80 Å | 0.90Å | 0.938 Å |
| 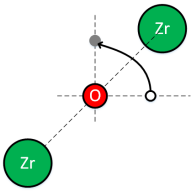 | R-Zr-Zr | 0.15 | 0.15 | 0.15 | 0.15 | 0.15 |
| 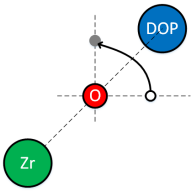 | R-Zr-DOP | 0.17 | 0.21 | 0.14 | 0.22 | 0.07 |
| 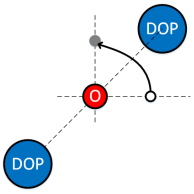 | R-DOP-DOP | 0.15 | 0.13 | 0.10 | 0.13 | 0.16 |

trapping energy can be calculated as the difference between the DOP-Zr-Zr and Zr-Zr-DOP jump or DOP-DOP-Zr and Zr-DOP-DOP jump. Sometimes the difference between the DOP-Zr-Zr and Zr-Zr-DOP jump differs slightly from the difference between the DOP-DOP-Zr and Zr-DOP-DOP jump, although it should be equal. This can be traced back to uncertainties in the finite-size correction. In those cases, the mean was formed and set as trapping. The resulting error was in all cases < 0.04 eV, which makes it a good approximation.

Apart from trapping, we see no blocking effect between Zr-Zr-Zr and Zr-DOP-Zr proton jumps for any dopant. The migration energy for the latter one is half the size of the first one at most. For yttrium-doped $BaZrO_3$, this is the main reason, why protons move faster in trapping zones than outside. For many different dopants, this jump was investigated further by Jordy Peulen.[57] He found out that for all dopants, the migration energy of this jump is lower than in the Zr-Zr-Zr configuration.

For most other configurations in table 5.12 we see a blocking by the dopant ions. This means, comparing the proton jumps in the DOP-Zr-Zr-, Zr-Zr-DOP-, and DOP-Zr-DOP-configuration with the corresponding jumps with a dopant on the second position, the migration energy is generally higher. Indium is the exception, where the opposite is always the case. Indeed, migration

**Table 5.12: Proton migration energies for translation jumps.** All eight possible permutations of the occupation of the zirconium sites in the first nearest neighbourhood of the initial and final positions of the translation jump. Zirconium is shown in green, the dopant in blue, oxygen in red and the proton in white. The corresponding migration energies were calculated explicitly by means of DFT and they were finite-size corrected.

| Dopant | | $Ga^{3+}$ | $Sc^{3+}$ | $In^{3+}$ | $Y^{3+}$ | $Gd^{3+}$ |
|---|---|---|---|---|---|---|
| Ionic radius | | 0.62 Å | 0.745 Å | 0.80 Å | 0.90Å | 0.938 Å |
| 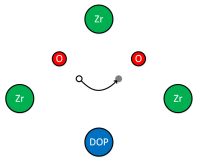 | Zr-Zr-Zr | 0.41 | 0.41 | 0.41 | 0.41 | 0.41 |
|  | Zr-DOP-Zr | 0.17 | 0.18 | 0.17 | 0.22 | 0.06 |
| 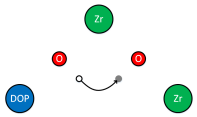 | DOP-Zr-Zr | 0.51 | 0.33 | 0.44 | 0.35 | 0.28 |
| 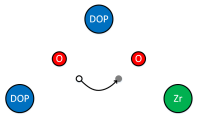 | DOP-DOP-Zr | 0.62 | 0.43 | 0.23 | 0.37 | 0.52 |
| 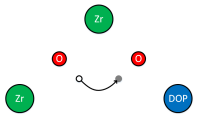 | Zr-Zr-DOP | 0.04 | 0.17 | 0.33 | 0.35 | 0.35 |
| 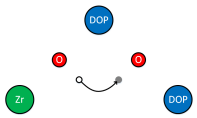 | Zr-DOP-DOP | 0.14 | 0.20 | 0.05 | 0.37 | 0.58 |
| 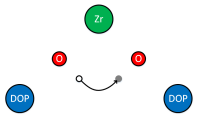 | DOP-Zr-DOP | 0.84 | 0.61 | 0.45 | 0.55 | 0.37 |
| 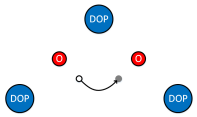 | DOP-DOP-DOP | 1.05 | 0.42 | 0.27 | 0.66 | 0.67 |

energies with indium dopants are lower than (or in the range of) the one in pure $BaZrO_3$, making it a very promising dopant for proton conduction. The same also applies in a weakened form for scandium as a dopant.

Gallium, on the other hand, stands out with very high migration energies for proton jumps out of the trapping zone and in highly doped configurations (like Ga-Ga-Ga). It is therefore expected to have a very low proton conductivity.

Gadolinium shows very low migration energies for the Zr-Gd-Zr-, Gd-Zr-Zr- and Zr-Zr-Gd-

jumps. In addition with its large trapping zone, this makes it promising for proton conduction.

## Oxygen vacancy migration energies

**Table 5.13: Oxygen vacancy migration energies for translation jumps.** All eight possible permutations of the occupation of the zirconium sites in the first nearest neighbourhood of the initial and final positions of the translation jump of the oxygen vacancy. Zirconium is green, the dopant is blue, oxygen is red and the oxygen vacancy is a black square. The corresponding migration energies were calculated explicitly by means of DFT and they were finite-size corrected.

| Dopant | | $Ga^{3+}$ | $Sc^{3+}$ | $In^{3+}$ | $Y^{3+}$ | $Gd^{3+}$ |
|---|---|---|---|---|---|---|
| Ionic radius | | 0.62 Å | 0.745 Å | 0.80 Å | 0.90Å | 0.938 Å |
| 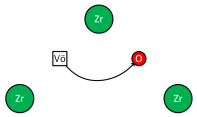 | Zr-Zr-Zr | 0.66 | 0.66 | 0.66 | 0.66 | 0.66 |
| 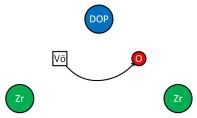 | Zr-DOP-Zr | 0.60 | 0.92 | 0.94 | 1.16 | 1.19 |
| 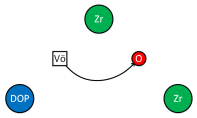 | DOP-Zr-Zr | 0.81 | 0.67 | 0.67 | 0.54 | 0.51 |
| 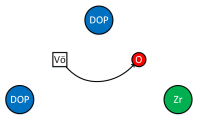 | DOP-DOP-Zr | 0.77 | 0.91 | 0.98 | 1.04 | 1.06 |
| 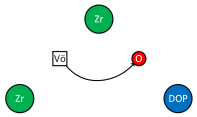 | Zr-Zr-DOP | 0.18 | 0.42 | 0.35 | 0.46 | 0.47 |
| 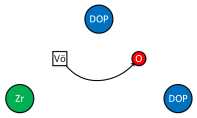 | Zr-DOP-DOP | 0.14 | 0.63 | 0.59 | 0.78 | 0.73 |
| 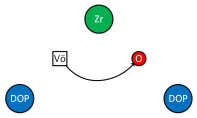 | DOP-Zr-DOP | 0.39 | 0.58 | 0.53 | 0.64 | 0.65 |
| 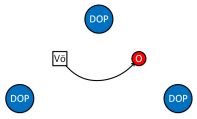 | DOP-DOP-DOP | 0.35 | 0.81 | 0.82 | 0.88 | 0.83 |

Migration energies for oxygen vacancy jumps are calculated for gallium-, scandium-, indium- and gadolinium-doped $BaZrO_3$ as described above and shown in table 5.13. Oxygen vacancy migration energies are dominated by the blocking effect. For scandium, indium, yttrium and gadolinium, the migration energy of a jump is always lower than the one of the corresponding jump with a dopant

ion on the central position (e.g. compare oxygen vacancy migration energies for the configurations Zr-Zr-Zr and Zr-DOP-Zr). For gallium, the opposite is always the case. Both can be explained with the ionic radii: zirconium has a radius of 0.72 Å[100], therefore, gallium is the only ion that is smaller. The smaller an ion is, the shorter is the jump pathway and thus, the smaller is the migration energy. For example for the Zr-DOP-Zr-jump, an almost linear trend between ionic radius and migration energy is observable. This also fits for all other jumps with a dopant on the central position.
For gadolinium, an additional deep trapping (compare previous chapter) of 0.24 eV was found analogous to yttrium-doped $BaZrO_3$ and is therefore included in the model.
From that, a very high oxygen vacancy conductivity in gallium-doped $BaZrO_3$ is expected in opposite to all four other dopants.

## 5.5 Co-doping

Additionally, co-doping becomes possible and was done in several experimental studies.[74,75,89,101] Therefore interaction energies between two dopants are calculated. They can be used in MMC-calculations to equilibrate the lattice. Although the interaction energies between different dopant

**Table 5.14: Interation energies between different dopants at certain distances.** They were calculated by means of DFT. All values in eV.

| Interaction | 4.23 Å | 5.982 Å | 7.327 Å | 8.46 Å | 9.459 Å |
|---|---|---|---|---|---|
| Y-Y | 0.20 | 0.01 | −0.02 | 0.08 | 0.00 |
| Y-Ga | −0.05 | 0.00 | 0.00 | −0.04 | 0.00 |
| Y-Gd | 0.23 | 0.00 | −0.03 | 0.10 | 0.00 |
| Y-In | 0.11 | 0.01 | −0.01 | 0.00 | 0.00 |
| Y-Sc | 0.07 | 0.01 | −0.01 | 0.02 | 0.00 |
| Ga-Ga | 0.07 | 0.00 | 0.03 | 0.03 | 0.00 |
| Ga-Gd | −0.08 | 0.00 | 0.00 | −0.05 | 0.00 |
| Ga-In | 0.04 | 0.01 | 0.01 | −0.01 | 0.00 |
| Ga-Sc | 0.01 | 0.00 | 0.01 | 0.00 | 0.00 |
| Gd-Gd | 0.27 | 0.00 | −0.03 | 0.12 | 0.00 |
| Gd-In | 0.09 | 0.01 | −0.02 | 0.03 | 0.00 |
| Gd-Sc | 0.07 | 0.01 | −0.01 | 0.02 | 0.00 |
| In-In | 0.11 | 0.01 | 0.00 | 0.01 | 0.00 |
| In-Sc | 0.04 | 0.01 | 0.00 | 0.01 | 0.00 |
| Sc-Sc | 0.04 | 0.00 | 0.01 | 0.02 | 0.00 |

ions are calculated (Fig. 5.14), KMC calculations with co-doping cannot be realized yet. That's because many migration energies for many different configurations would have to be calculated,

*e.g.* for Ga-Y-Zr or Ga-Ga-Y jumps, etc. To the present day, this is still work in progress, but a promising project for the future.

# 6

# Proton Conduction

"Je weiter das Experiment von der Theorie entfernt ist, desto näher ist es am Nobelpreis."

- Irène Joliot Curie, physicist, chemist and Nobel Prize winner.

In chapter 5 a pair interaction model with migration energies and some assumptions and simplifications was introduced. This model was referred to as the *simplified model* and it is now used to perform KMC-simulations in fully hydrated yttrium-doped $BaZrO_3$. All migration energies for proton jumps are used in these simulations but no oxygen vacancies or polarons are incorporated in this chapter. The attempt frequencies are used as described in the previous chapter.
Parts of this chapter have already been published.[13] Here, the insights gained are discussed deeper and in more detail.

## 6.1 Simulation and Experiment

At first, the ionic conductivity of protons $\sigma_H$ is simulated as a function of the yttrium dopant fraction $x$ and temperature $T$. $\sigma_H$ is calculated after equation 2.8 as $\sigma_H = q_H \cdot u_H \cdot c_H$ and shown in figure 6.1, left. While $e$ is constant, $c_H$ increases linearly with the dopant fraction. Therefore, all non-linear behaviour must come from the ionic mobility which is shown in figure 6.1, right. The proton conductivity increases with the dopant fraction until $x \approx 0.45$ and then decreases again. It must be said here, that the highest dopant fraction that could experimentally be achieved is $x = 0.4$[95] making simulations on higher fractions of academic interest only.

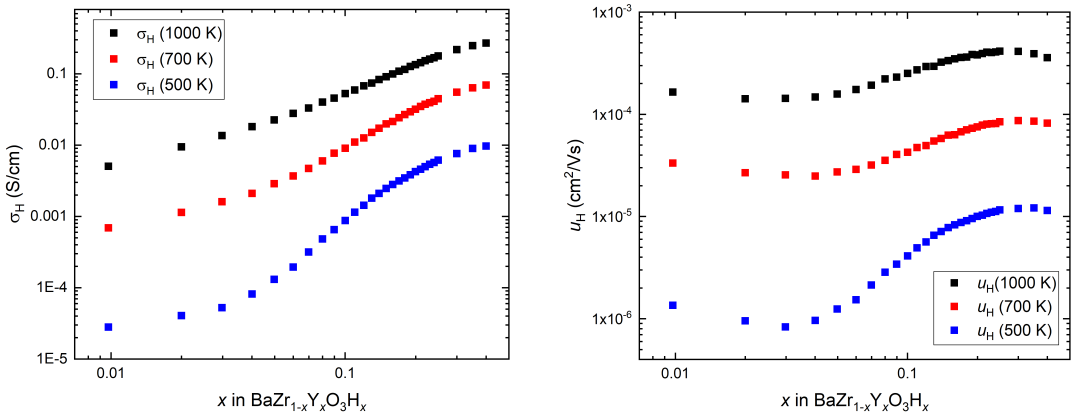


**Figure 6.1: Simulated proton conductivities and mobilities in yttrium-doped $BaZrO_3$.** Left: Simulated proton conductivities as a function of the yttrium dopant fraction at different temperatures. Right: Simulated proton mobilities as a function of the yttrium dopant fraction at different temperatures. They are simulated within the *simplified model* in fully hydrated $BaZrO_3$ in a 16×16×16 supercell. The dopants are distributed randomly in the simulation cell.

The proton mobility decreases at low dopant fractions, reaches a minimum and increases again until a maximum at $x \approx 0.3$ after which it decreases again. The first decrease can be explained through trapping zones around yttrium dopants. They are isolated in the crystal and trap protons, that do contribute less to the overall conductivity as a consequence. This effect is overcompensated by the increasing proton concentration, which results in increased conductivity. The increase in mobility is explained by trapping zones start to overlap and form nanoscale percolation pathways. The migration barriers inside of the trapping zone are smaller than outside. Therefore, trapped protons move faster than those outside, resulting in increased mobility and conductivity. The adjective 'nanoscale' clarifies the fact, that no complete pathways are needed for this acceleration. Even parts of percolation pathways are sufficient to overcompensate the higher migration barrier for jumps out of the trapping zones. The dopant fraction after which this percolation phenomenon predominates, meaning the one with the lowest proton mobility is called percolation threshold $x_{min}$. Figure 6.2 shows the nanoscale percolation pathways for four different random dopant distributions.

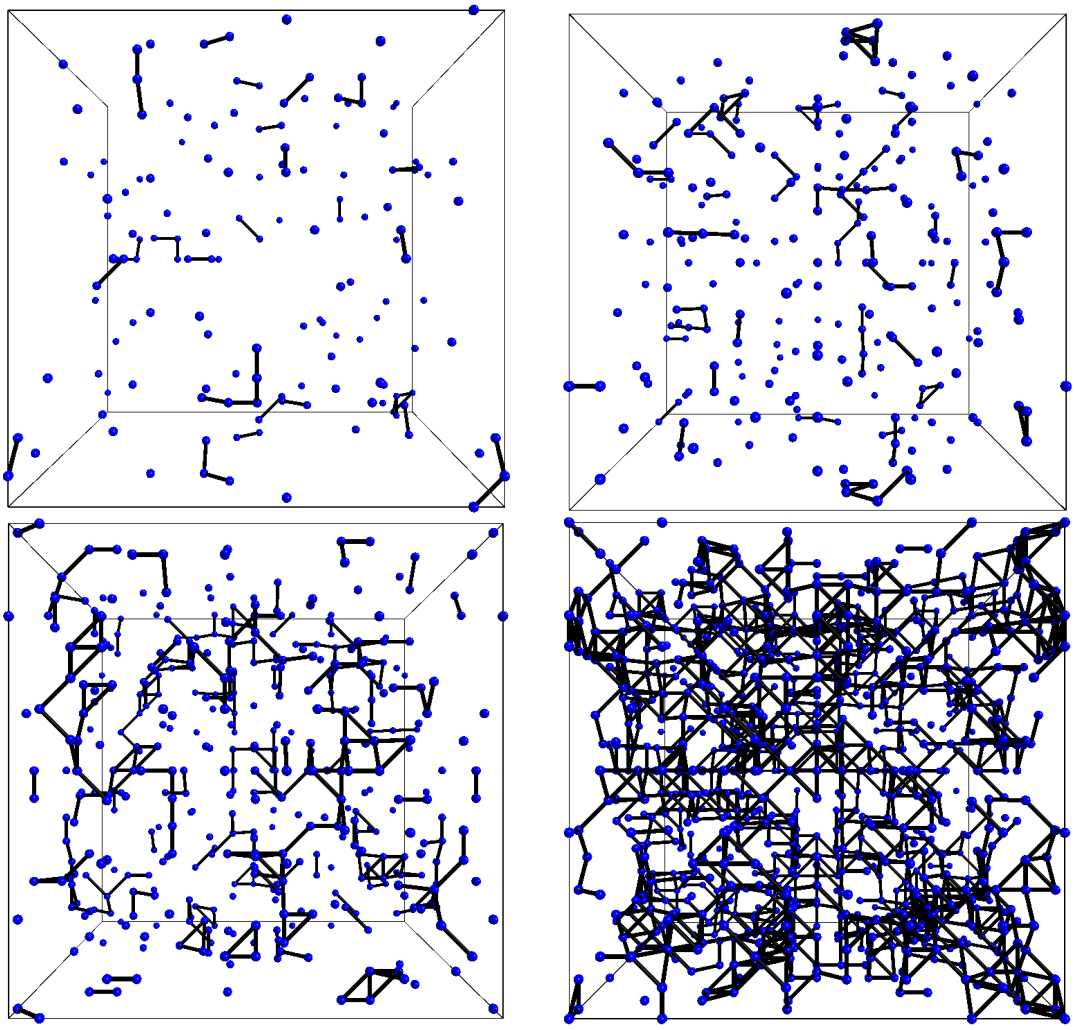

**Figure 6.2: Nanoscale percolation pathways for four different random dopant distributions.**[13] Blue dots symbolize yttrium dopants in a 16 × 16 × 16 super cell and black lines symbolize overlapping trapping zones. Four different dopant fractions are shown. Top left: $x = 0.03$, top right: $x = 0.05$, bottom left: $x = 0.09$ and bottom right: $x = 0.25$.

At high dopant fractions of 0.3 – 0.45, the mobility decreases. This can be explained by the more frequent occurrence of jumps in the Y-Y-Y configuration (Tab. 5.12) that have high migration barriers. From a certain concentration, these jumps are unavoidable, slowing the protons down.
In experiments, dopant fractions of 0.1 and 0.2 are very common. Therefore, our simulated conductivities are compared at both dopant fractions with experimental results from the literature and also activation energies for protons are calculated. All values are plotted in an Arrhenius-plot with $\ln(\sigma_H T) = \ln(a) - E_a/RT$, with $a$ as the pre-exponential factor and $E_a$ as the activation energy (Fig. 6.3). All the experimental values in figures 6.3 were measured with electrochemical impedance spectroscopy. Differences in the experimental values may come from different sources:

- The sintering process and sintering time. The sample density could vary as well as the dopant distribution in the crystal.
- The Analysis. The separation of bulk and grain boundary conductivities in the polycrystalline samples could also vary.
- Differences in the real dopant fraction.
- Samples, that are not fully hydrated.

Of special interest are the extrapolated values from the experimental work from Kreuer *et al.*,[26] where measurements on single crystals have been performed. This excludes the first two error sources. Our simulations can reproduce the absolute conductivity values as well as the activation energies very precisely, although it has to be admitted that our simulations were performed at different temperatures than the measurements. The values from Pornprasertusk *et. al.*[102] are also well reproduced while the other values are at least one order of magnitude lower. Nevertheless, the activation energy from Shirpour *et al.*[92] still fits to ours. The activation energies for proton con-

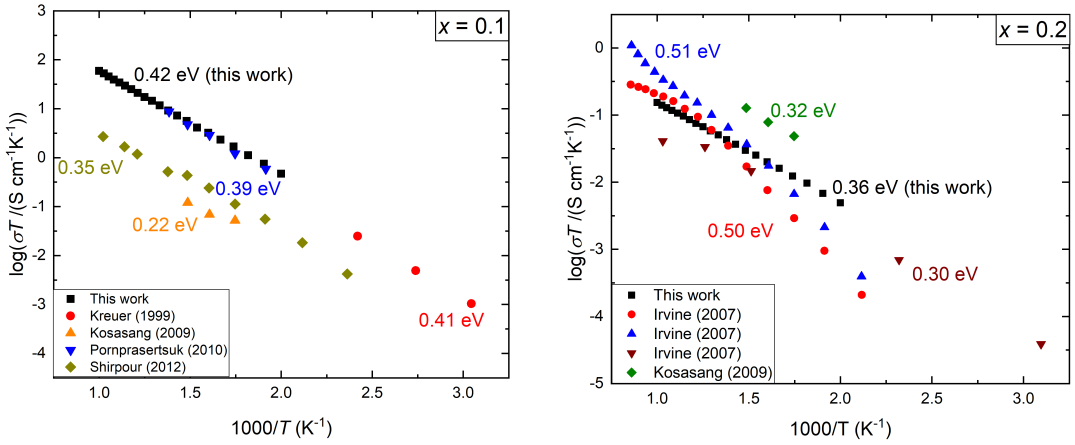


**Figure 6.3: Simulated proton conductivities and mobilities in yttrium-doped $BaZrO_3$ in comparison with experiments.** Left: Proton conductivities in $BaZr_{0.9}Y_{0.1}O_3H_{0.1}$. Black symbols show the simulated proton conductivities dependent on the simulation temperature in fully hydrated $BaZrO_3$ from this work. They are compared to experimental studies from Kreuer[103], Kosasang *et al.*[95], Pornprasertsuk *et al.*[102] and Shirpour *et al.*.[92] Right: Proton conductivities in $BaZr_{0.8}Y_{0.2}O_3H_{0.2}$. Black symbols show the simulated proton conductivities dependent on the simulation temperature from this work. They are compared to experimental studies. from Kosasang *et al.*[95] and Irvine *et al.*.[104]

ductivity are 0.42 eV for $x = 0.1$ and 0.36 eV for $x = 0.2$, respectively. This also fits well to literature values.[6,26,92,95,102,104–106] The decisive factor is, that our model is based on microscopic migration energies. The activation energies come from sufficiently long KMC studies (Fig. 6.3), providing a link between microscopic and macroscopic world. In the present simulations, the average proton displacement is about 350 nm corresponding to the typical grain size in polycrystalline powders.

Activation energies for proton conductivity were calculated analogously for all dopant fractions from $x = 0.01$ to $x = 0.4$ in yttrium-doped $BaZrO_3$ (Fig. 6.4). Starting with about 0.5 eV at $x = 0.01$, the activation energy increases up to a maximum around $x = 0.03$ which is in good agreement with the position of the minimum of the proton mobility (Fig. 6.1). Isolated yttrium dopants trap protons and reduce their contribution to the overall conductivity. Therefore, the activation energy increases until the nanoscale percolation pathways come into effect. With increasing dopant fraction and therefore increasing number and length of the pathways, the activation energy stays on one level around 0.35 eV. This level refers to proton jumps in the dopant configurations Y-Zr-Zr, Zr-Zr-Y, Y-Y-Zr and Zr-Y-Y that cannot be avoided during the simulation. Therefore, the activation barrier will not decrease further, although many migration energies involved are below 0.35 eV (all reorientation jumps and the translation jump in Zr-Y-Zr configuration).

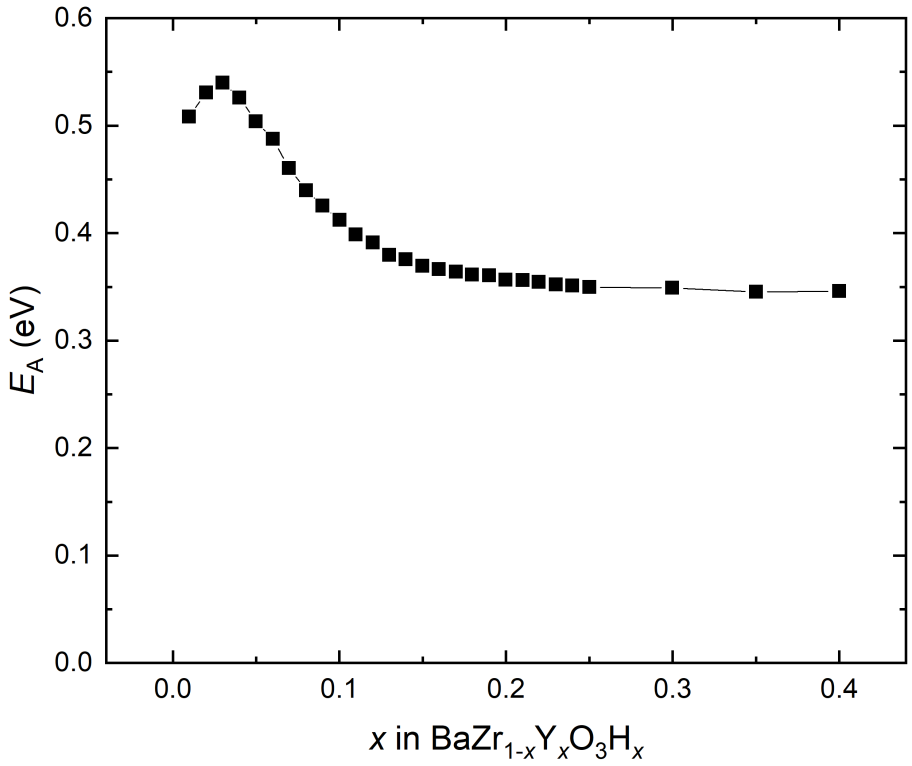


**Figure 6.4: Activation energies of the proton conductivity of yttrium-doped $BaZrO_3$.** All activation energies were received from Arrhenius-plots of the simulated proton conductivities of yttrium-doped $BaZrO_3$ at three different temperatures: 1000 K, 700 K and 500 K.

## 6.2 Dopant Superstructures

Percolation pathways cause a significant increase in proton mobility. For this reason, they are investigated in more detail. Simulation cells with dopant superstructures in 1D, 2D and 3D are artificially designed and the proton conductivity in these cells is compared to cells with a random distribution but with the same dopant fraction.

Eight superstructures are introduced: The first has a complete percolation pathway from one side of the supercell to the other (number 1 in Fig. 6.5 and on top in Fig. 6.6). For the second, it was taken into consideration, that only nanoscale percolation pathways are necessary to improve the conductivity. Therefore, a superstructure was built with one dotted line-like percolation pathway with alternating zirconium and yttrium ions (number 2 in Fig. 6.5 and bottom in Fig. 6.6). Two of these dotted line-like pathways are placed in supercell 3 and 4 – once close together and once far away from each other. They have as many yttrium dopants as one complete pathway. Their conductivity is therefore directly comparable.

A 2D superstructure is created in supercell 7 with one yttrium dopant plane in the cell and three 3D superstructures are built in supercells 5, 6 and 8. In one case, the yttrium dopants are arranged in a primitive cubic superstructure (6), a bcc superstructure (5) and a fcc superstructure (8).

Results in figure 6.6 show the proton mobility with the electric field arranged parallel to the 1D or 2D superstructure. If it was vertically arranged, no mobility increase would be measurable compared to the random distribution. In every case except superstructure 8, the proton mobility is generally higher in the ordered structure. For one complete percolation pathway an increase of 9 % is obtained. The same applies to the dotted line-like pathway. The increase comes in both cases through the occurrence of the energetically favourable Zr-Y-Zr-Jump with $E_{mig}$ = 0.22 eV and although the proton has to overcome the border of the trapping zone several times this has no negative effect in the dotted line-like pathway. The opposite is the case: If two of these paths are created far apart, the mobility increases by 20 % – that's 11 % more than the complete pathway with the same dopant fraction. This increase is dampened if both pathways are next to each other, because this enforces the occurrence of Y-Zr-Y-configurations with $E_{mig}$ = 0.55 eV. These jumps are unlikely and therefore slow the protons down. Nevertheless, the increase in mobility for two dotted line-like pathways next to each other is 17 % compared to the random structure – still 6 % more than the complete pathway.

In the supercell with the 2D yttrium dopant plane, proton mobility is increased by 20 %. Inside of the plane there are energetically unfavourable Y-Y-Y-configurations ($E_{mig}$ = 0.66 eV). Those are avoided by the protons, lowering the possible number of jump pathways for them. An 'interrupted plane', meaning single complete pathways, that are separated by zirconium atoms should have a higher mobility.

This is the case for the cubic primitive superstructure (6). This corresponds to dotted line-like pathways everywhere in the supercell separated through paths with no dopants. In this way, in ev-

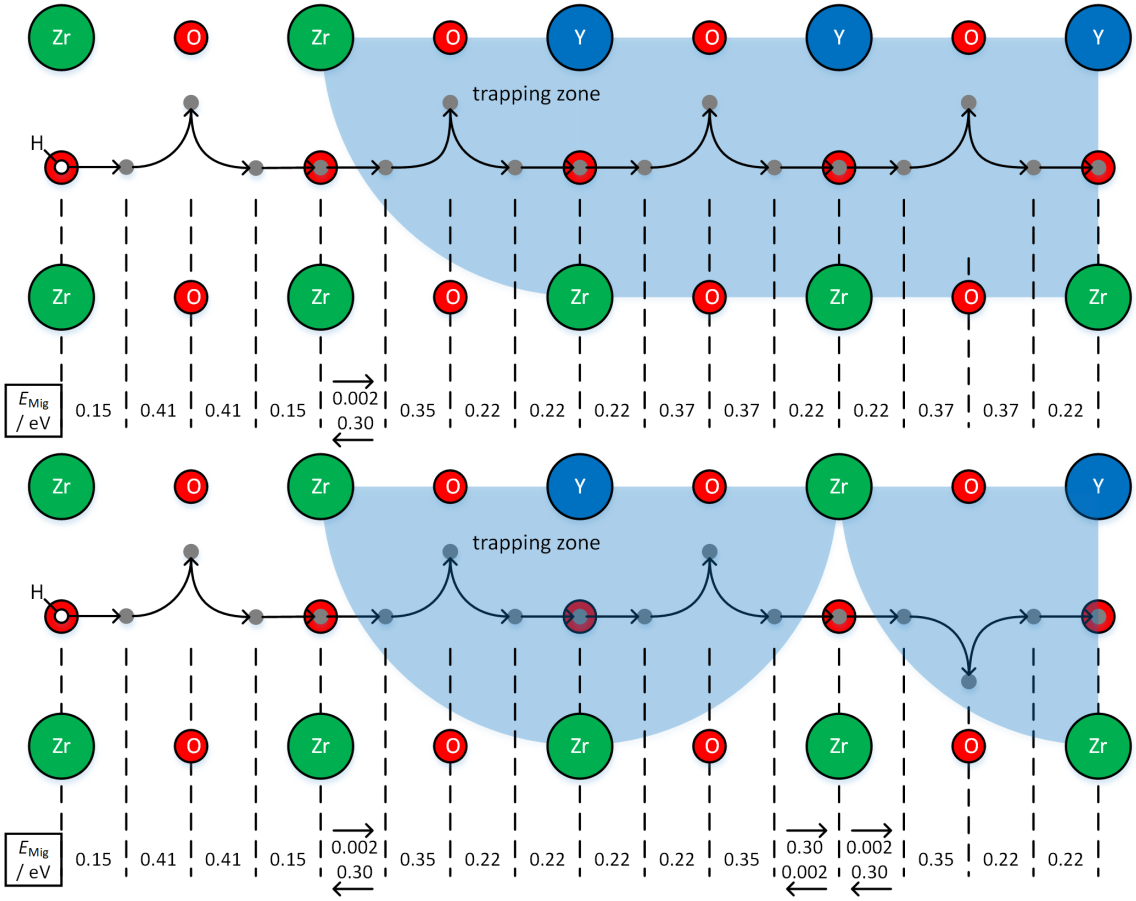


**Figure 6.5: 2D cuts through $BaZrO_3$, showing dopant superstructures in detail.**[13] Top: On the left-hand side, proton jumps in pure $BaZrO_3$ are shown. On the right-hand side a continuous percolation pathway is shown corresponding to super structure 1 in figure 6.6. Bottom: On the left-hand side, proton jumps in pure $BaZrO_3$ are shown, whereas on the right-hand side a dotted line-like percolation pathway is shown corresponding to super structure 2 in figure 6.6. Yttrium dopant atoms and their trapping zones are shown in blue and light blue, respectively. The possible proton positions are grey and the proton is white. The migration energies $E_{mig}$ of each jump are given below the jump.

ery space diagonal there is always an alternating sequence of yttrium and zirconium resulting in a dopant fraction of 0.125. An increase in proton mobility of 78 % is observed which is the highest increase in all superstructures.

The highest total proton mobility, however, is observed for the bcc superstructure (5) with $x = 0.25$, with an increase of 62 % from the already high, proton mobility of the random superstructure. Here, the simple cubic superstructure is taken and one yttrium atom is added in the center of every simple cubic cell. This is the most dense packing of dotted line-like pathways that is geometrically possible. Every single yttrium dopant that is added builds areas in the supercell where energetically unfavourable Y-Y-Y-jumps cannot be avoided. Therefore, in superstructures with higher dopant fractions than 0.25, no further increase in mobility is to be expected. On the contrary, a decrease

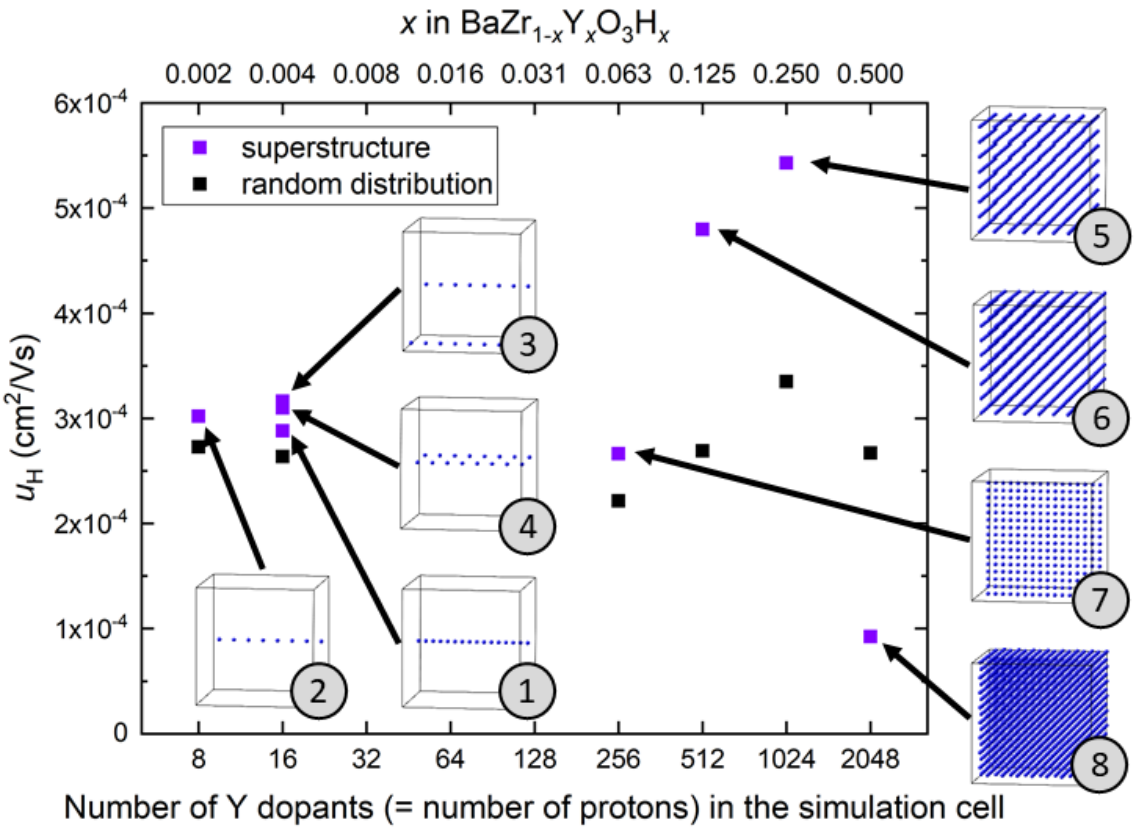


**Figure 6.6: Calculated proton mobilities for different 1D, 2D and 3D dopant superstructures in comparison to a random dopant distribution.**[13] Supercell 1 shows a 1D percolation pathway with dopant atoms in first nearest neighbourhood along the (100) direction. Supercell 2 shows a 1D dotted line-like percolation pathway with dopant atoms in the second nearest neighbourhood along the (100) direction. Supercells 3 and 4 show two 1D dotted line-like percolation pathways next to each other (4) and far away from each other (3). Supercell 6 shows a 3D simple cubic dopant superstructure, supercell 5 a 3D bcc dopant superstructure, supercell 7 a 2D superstructure with dopant atoms next to each other within the x–y plane and supercell 8 a 3D superstructure with dopants on every other Zr position. Each supercell contains 4096 Zr positions, and all the simulations were performed at a temperature of $T$ = 1000 K.

to 34 % is observed for the fcc superstructure (8).

All values that are discussed above are simulated at a temperature of 1000 K. Going to lower temperatures, proton mobilities generally also decrease. Nevertheless, the influence of the migration energies becomes more important. This can be made clear in the case of the simple cubic superstructure. At 1000 K, the proton mobility increases by 78 %, but at 700 K, the increase is 170 % and at 500 K 240 % although the absolute values are highest at 1000 K.

## 6.3 Parameter Study

The general advantage of a computer model lies in its adaptability. Within the *simplified model*, several parameters such as the trapping radius, the depth of the trapping zone, the migration energies or the difference between trapping in 1NN and 2NN can be varied. This way, many other dopants are conceivable. Therefore, the influence of these parameters is investigated and discussed below.
One parameter with a large influence is the trapping radius. Therefore two simulation series are performed, one where the trapping radius has been decreased from 4.3 Å for yttrium to 3 Å where protons are only trapped in 1NN and to 0 Å, disabling the trapping. In both series all other parameters from the model for yttrium dopants are used, and they are both compared to the case with yttrium dopants (Fig. 6.7).

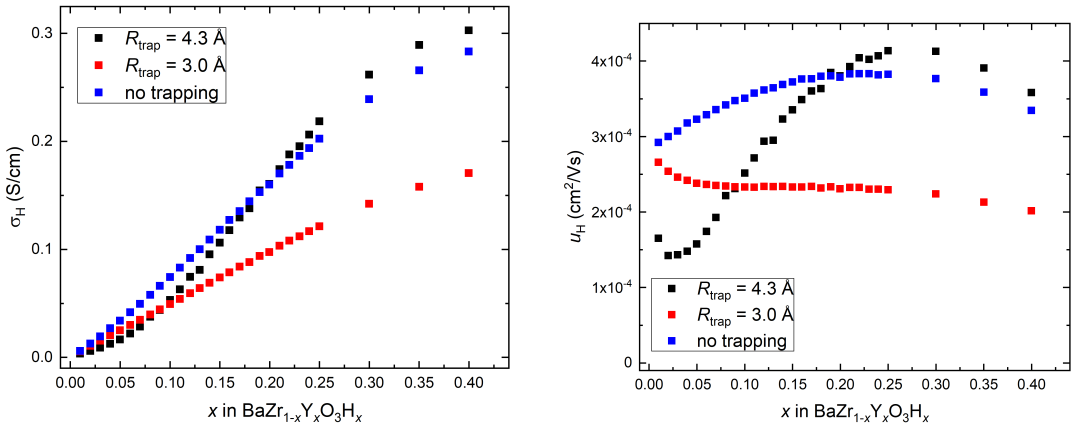


**Figure 6.7: Simulated proton conductivities (left) and mobilities (right) in doped $BaZrO_3$ dependent on the dopant fraction and the radius of the trapping zone.** They are simulated within the basis set of the *simplified model* in fully hydrated $BaZrO_3$ in a 16×16×16 supercell at $T = 1000$ K.

For $x \to 0$ the proton conductivities are necessarily the same. Going to higher fractions the conductivity curves for different trapping radii extend similar for very low dopant fractions. But for both curves with trapping there is a dopant concentration at which the conductivity increases much stronger than for the case without trapping. In the mobility plot (Fig. 6.7, right), this dopant fraction is found at the local minimum of the curve and called $x_{min}$.
The larger the zone, the lower is $x_{min}$ and vice versa. For a trapping range of 4.3 Å, its around $x = 0.03$ and for 3 Å around $x = 0.1$ and very flat. Without a trapping zone no percolation occurs, the mobility increases but this increase weakens due to a tendency of the protons to block each other during the simulation.
It was discovered that the threshold does not only depend on the number of proton positions that are trapped, but on $E_{trap}$ whose variation is shown in figure 6.8. In the extreme case with a very deep trap (-10 eV), the percolation threshold appears at a dopant fraction of $x = 0.10$ and below no ionic conductivity is measurable at all. Therefore, we may conclude, only at fractions of 0.10 and

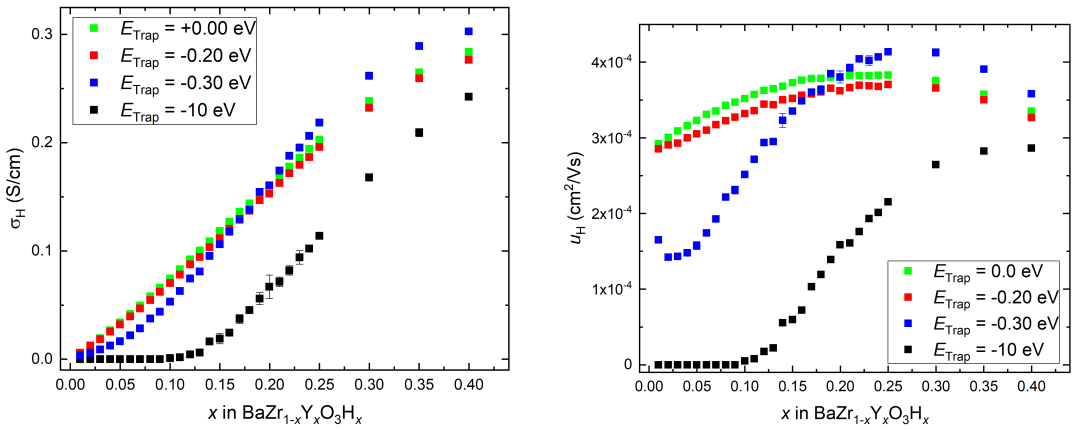


**Figure 6.8: Simulated proton conductivities (left) and mobilities (right) in doped $BaZrO_3$ dependent on the dopant fraction and the depth of the trapping zone.** They are simulated within the *simplified model* in fully hydrated $BaZrO_3$ in a 16×16×16 supercell at $T$ = 1000 K.

higher complete percolation pathways are built for any trapping energy. Below this, only nanoscale percolation pathways increase the conductivity.

If the trapping zone is flat ($E_{trap}$ = −0.2 eV and $E_{trap}$ = 0.0 eV) the percolation phenomenon disappears as the probability for jumps out of the trapping zone becomes very high.

Applying an additional energy amount for the trapping in 2NN, $E_{2NN}$ had effects similar to the change of the whole trapping zone. Lowering led to decreasing conductivity and vice versa.

Varying the migration energy at the edge of the trapping zone artificially is not the same as varying $E_{trap}$. Referring to figure 5.4, it is the difference between $E_{mig}$ in the figure and $E_{conf}$, to which $E_{trap}$ contributes. Increasing $E_{trap}$ also increases the migration barrier for jumps out of the zone but decreases the barrier for jumps into the zone. Enhancing the migration energy at the edge increases both barriers by the same value. Nevertheless, similar trends in conductivity or mobility are observed. Also, the percolation threshold increases with increasing migration energies at the edge, just like with increasing $E_{trap}$.

The variation of migration energies inside of the trapping zone lead to results that follow logically from the variation of $E_{trap}$: Decreasing the migration energies leads to a lowering of $x_{min}$. Therefore, with increasing migration energies inside of the trapping zone, $x_{min}$ is moved to higher values until it disappears when they become higher than the energy barrier for jumps out of the zone.

This applies in particular just for the variation of the migration energy of the translation jumps $E_{in,T}$. When varying the reorientation jumps $E_{in,R}$, even at very high barriers of 0.4 eV, a percolation threshold at $x$ = 0.75 is detectable. During the simulation both reorientation and translation jumps must take place, so an increase in either $E_{in,T}$ or $E_{in,R}$ increases $x_{min}$ but not equally strong. Translation jumps seem to have a greater impact on the conductivity and mobility: $E_{in,T}$ = 0.4 eV with $E_{in,R}$ = 0.1 eV leads to significantly lower values than as if both energies were reversed.

During the variation of the migration barriers outside of the trapping zone no significant differ-

ence between varying $E_{out,R}$ or $E_{out,T}$ was observed, neither in the absolute values nor in the dopant fraction of the percolation threshold. In both cases, the threshold is moved to lower fractions with increasing barrier outside, which is complementary to the decrease of the barriers inside of the trapping zone. Changes in the migration barriers outside though have a much lower effect on $x_{min}$. This is due to the fact that the main part of the proton migration takes place inside of the zone for most dopant fractions. As shown above, no later than for $x = 0.1$, complete percolation pathways are build which means that for higher fractions the proton migration outside of the pathway becomes minor important.

## 6.4 Other Dopant Ions

The theoretical parameter studies become useful for understanding proton conductivities and mobilities in variously doped $BaZrO_3$. Migration and interaction energies for four more dopants were calculated (see Chapter 5) and used in KMC simulations: gallium, scandium, indium and gadolinium. These differ in parameters like trapping radius (gallium, scandium and indium trap only in 1NN, yttrium and gadolinium in 1NN and 2NN), depth of the trapping zone (ranging from −0.48 eV for gallium to only −0.15 eV for indium) and their migration energies (see tab. 5.11 and 5.12).
In each simulation series, there was only one dopant ion at a time, no co-doping was applied and each system was fully hydrated. The simulations were performed in a 10×10×10 supercell (for performance reasons no 16×16×16 supercell was used) for 10000 MCSP. The results of the simulated conductivity are shown in figure 6.9 and the simulated mobility in figure 6.13.
The different dopants are discussed in detail in the following.

### Gallium-doped $BaZrO_3$

Gallium dopants trap protons very strongly with −0.48 eV in 1NN. In 2NN protons are not trapped. Here, the simplified model is not applied, meaning, one proton within the trapping radius of two gallium dopants is not only trapped with $E_{trap}$ *once* but twice. Thereby, around two gallium dopants on neighbouring sites, a stair-like trapping zone with a trapping energy of −0.96 eV between both ions and −0.48 eV on every other trapped position is formed (see Fig. 6.10).
Although the migration energies for jumps into the trapping zone ($E_{Mig,Zr-Zr-Ga}$ = 0.04 eV) and around one gallium atom ($E_{Mig,Zr-Ga-Zr}$ = 0.17 eV) are very low, jumps out of the trapping zone have a high migration energy of 0.51 eV. This strong trapping and the high migration energies for higher doped configurations ($E_{Mig,Ga-Zr-Ga}$ = 0.84 eV, $E_{Mig,Zr-Ga-Ga}$ = 0.61 eV and $E_{Mig,Ga-Ga-Ga}$ = 1.05 eV) lead to a very low proton conductivity compared to all other dopants (Fig. 6.9).
Despite the fact that the absolute conductivity is very low, the curves for conductivity and mobility show an unexpected behaviour (Fig. 6.11): With increasing dopant fraction, the conductivity increases until it reaches a maximum around $x = 0.2$. This can be explained by the combination of

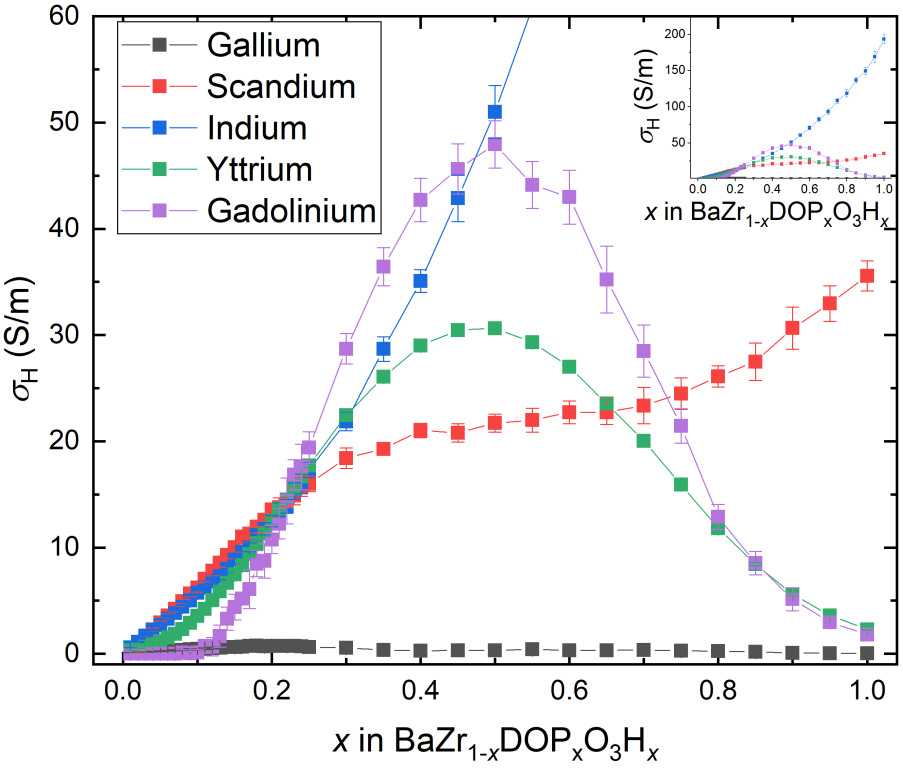


**Figure 6.9: Simulated proton conductivities in doped $BaZrO_3$ dependent on the dopant fraction and the dopant ion.** They are simulated in fully hydrated $BaZrO_3$ in a 10×10×10 supercell at 1000 K. The lines are a guide to the eye. The inset shows the same data on a different scale to bring the proton conductivity in indium-doped $BaZrO_3$ into perspective.

trapping and blocking: The more protons are brought into the system, the higher the conductivity gets. But with increasing dopant fraction, the probability of protons to become trapped also increases. Inside of these traps, protons move fast ($E_{Mig,Zr-Ga-Zr}$ = 0.17 eV) but they rarely escape them ($E_{Mig,Ga-Zr-Zr}$ = 0.51 eV). As soon as gallium dopants start to build clusters, configurations with very high migration energies ($E_{Mig,Ga-Zr-Ga}$ = 0.84 eV and $E_{Mig,Ga-Ga-Ga}$ = 1.05 eV) play a bigger role. This generally leads to a decrease in conductivity. Due to the trapping, however, the proton mobility decreases with increasing dopant fraction. This is overcompensated by the increasing concentration which leads overall to the increasing conductivity up to $x$ = 0.2. At higher dopant fractions it is no longer overcompensated.

At $x$ = 0.4 eventually, there is a peculiarity: The conductivity has a minimum after which it increases again. The mobility has a plateau until around $x$ = 0.7. This cannot be explained by the formation of percolation pathways, because these are not beneficial for protons. Additionally (in anticipation of chapter 9), at different degrees of hydration, this minimum occurs at drastically different dopant fractions. Therefore, geometrical arguments can be excluded.

An additional observation can be made at the site trapping: The occurrence of site trapping events

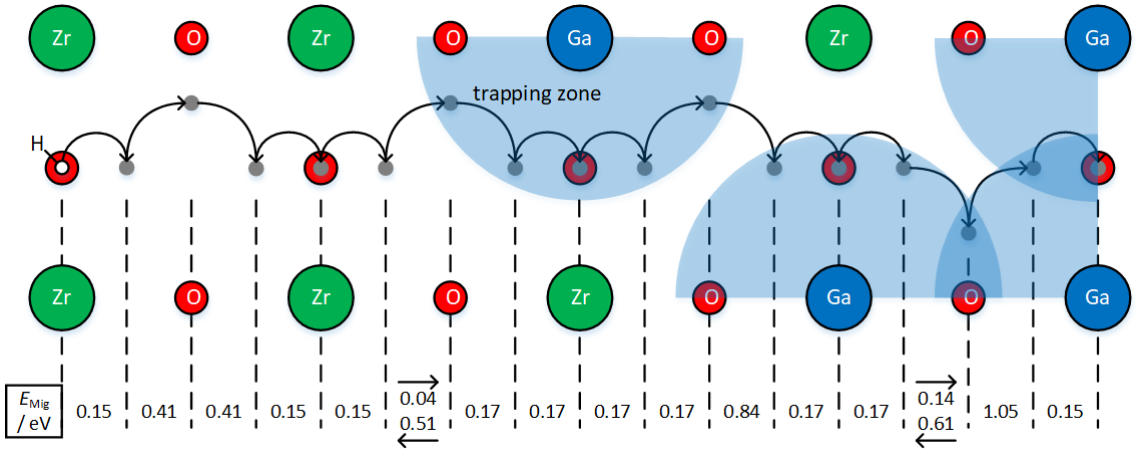


**Figure 6.10: One possible jump path for a proton through gallium-doped $BaZrO_3$.** On the left hand side, jumps in pure $BaZrO_3$ are shown while there are on the right hand side configurations with more gallium ions. The stair-like trapping with a twice as deep trap between two gallium ions is shown in darker blue.

increases linearly up to $x = 0.25$ and then stays on one level, maybe with a slight decrease. The greatest frequency of site trapping will occur inside of the trapping zones, because here, the protons are trapped an a very small volume. The fact that site trapping does not increase after $x = 0.25$ suggests, that the number of protons inside of the trapping zones does not increase further. Therefore, since the overall number of protons increases, more and more are kept outside of the zones. Here, they move with a migration energy of $E_{Mig,Zr-Zr-Zr} = 0.41$ eV, which is less worth than being trapped. This leads to the increased proton conductivity and the plateau in mobility.

Another indicator is the large sizes of the error bars at high dopant fractions. If protons are kept outside of the percolation pathways, there can be randomly ordered simulation cells where this is more true than in others. Therefore, in some simulations, the conductivity is significantly larger, and since every data point is the average of 12 calculations, this leads to large error bars.

This whole phenomenon can be explained through protons inside of the trapping zones hindering those outside to enter them. They occupy positions at the border of the trapping zones but to effectively shield the zones, there are many trapped protons necessary. Therefore, this effect takes place only at high dopant fractions. Nevertheless, for $x \geq 0.7$, the conductivity decreases rapidly, because jumps in the Ga-Ga-Ga configurations with $E_{Mig,Ga-Ga-Ga} = 1.05$ eV can no longer be avoided.

The solubility of gallium in $BaZrO_3$ however, is low compared to yttrium. Regardless of some disagreements between different literature sources, the solubility limit is somewhere between $x = 0.075$[63] and $x = 0.1$[75]. In this area, gallium-doped $BaZrO_3$ is a bad proton conductor, which is confirmed in literature.[2,74,75,107] The reported conductivity values in general seem to be even lower than our simulated ones (Fig. 6.11). There are a few approaches that add gallium as

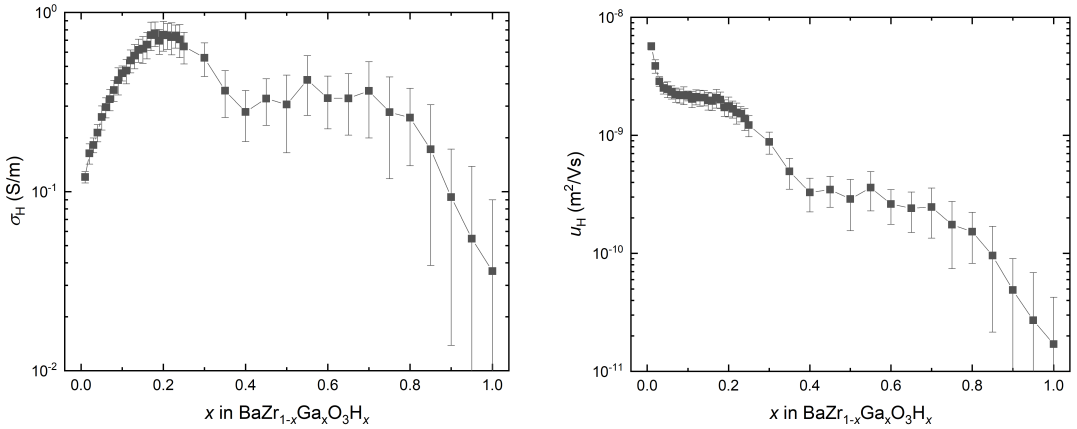


**Figure 6.11: Simulated proton conductivities (left) and mobilities (right) in gallium-doped $BaZrO_3$ dependent on the dopant fraction.** They are simulated in fully hydrated $BaZrO_3$ in a 10×10×10 supercell at 1000 K. The lines are a guide to the eye.

a co-dopant to yttrium-doped $BaZrO_3$, to improve the sintering process,[63,74,75] but even there, gallium is problematic, because it lowers the conductivity noticeably.

There is also one theoretical study, that calculated microscopical migration energies in a 2×2×2 supercell with one gallium atom, which corresponds to $x = 0.125$.[62] These migration energies deviate far from our values, which can be explained by the insufficient size of the supercell and their method of determination for the migration energy. The transition point was merely estimated but not calculated with an established algorithm.

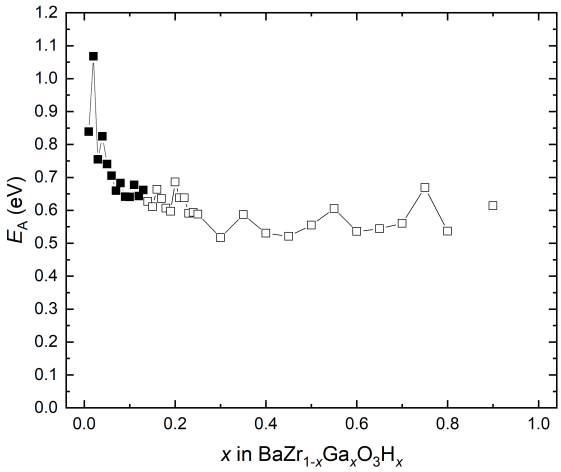


| Dopant Fraction | $E_a$ (this work) | $E_a$ (Literature) |
|---|---|---|
| 0.016 | 1.07 | 0.59[59] |
| 0.037 | 0.82 | 0.59[59] |
| 0.1 | 0.64 | 0.83[75] |
| 0.1 | 0.64 | 0.72[59] |
| 0.125 | 0.66 | 0.62[59] |

**Figure 6.12: Activation energies of the proton conductivity of gallium-doped $BaZrO_3$.** Left: All activation energies were received from Arrhenius-plots of the simulated proton conductivities of gallium-doped $BaZrO_3$ at three different temperatures: 1000 K, 700 K and 500 K. Right: Selected simulated values from this work are compared to available literature values. All activation energies in eV. Hollow symbols are used for calculations beyond the solubility limit.

Activation energies of the proton conductivity of gallium-doped $BaZrO_3$ were calculated via Arrhenius-plots and they are shown in figure 6.12 for all dopant fractions. Selected simulated data are compared to available literature values. As discussed earlier, the error of the calculated conductivities is high, which leads to a strong scattering of the activation energies. Nevertheless, a general trend can be read from the data: With increasing dopant fraction, the activation energy decreases until it reaches a plateau around 0.6 eV. One other study showed an activation energy of 0.62 eV at $x = 0.125$[59], which is in good agreement with our data as well as for $x = 0.1$, with a value of 0.72 eV. For low dopant fractions, however, their calculated values of 0.59 eV are much lower than ours. The only experimental study[75] showed a much higher value at $x = 0.1$ than the calculated ones. Here, more experiments and longer simulations would be necessary to get more clarity but since the proton conductivity in gallium-doped $BaZrO_3$ is low, it is questionable whether it is worth it.

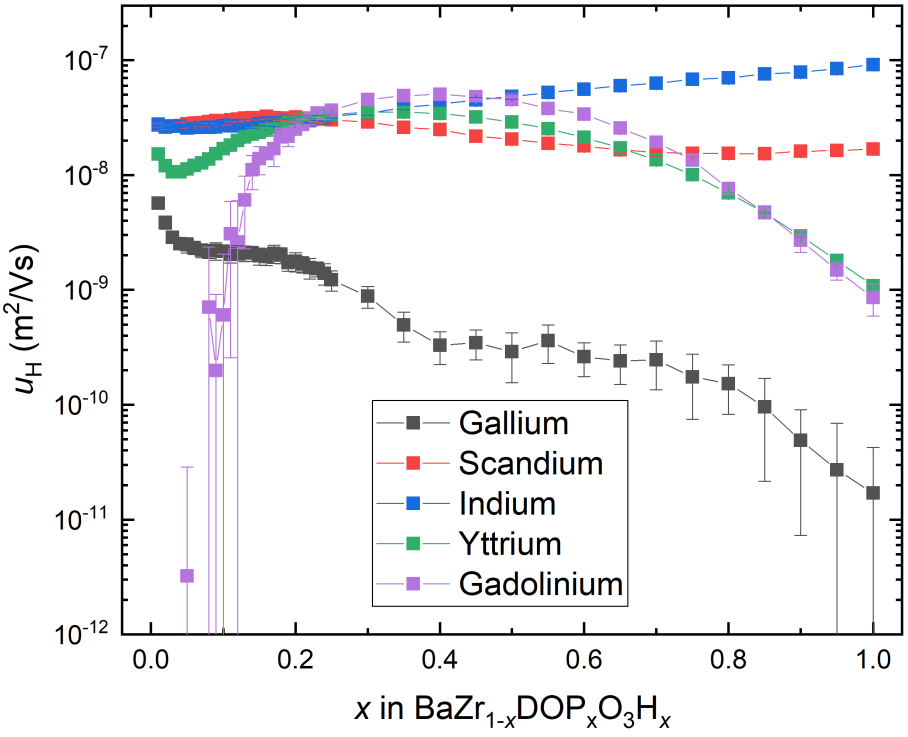


**Figure 6.13: Simulated proton mobilities in acceptor-doped $BaZrO_3$ dependent on the dopant fraction and the dopant ion.** They are simulated within in fully hydrated $BaZrO_3$ in a 10×10×10 supercell at $T = 1000$ K. The lines are only a guide to the eye.

## Scandium-doped $BaZrO_3$

Scandium dopants in $BaZrO_3$ trap protons also only in 1NN but the trapping is not as deep as for gallium dopants: −0.20 eV is not even half as deep. Nevertheless, the deep trapping at positions that are double trapped by two scandium ions was found as well. The migration energies are generally low. Because of that, it is not to be expected that blocking plays an important role in the KMC simulations.

The conductivity increases constantly with increasing dopant fraction with two changes in slope: one around $x = 0.3$ and one around $x = 0.7$. Between both values, the conductivity increases slower. The mobility however, increases, reaches a maximum around $x = 0.2$ and decreases again until $x = 0.7$, whereafter it increases again slightly. The minimum at $x = 0.02$ is caused by fluctuations in the error range and is not significant. This region was resolved more finely in steps of $x = 0.001$ and it was found, that the mobility stays constant until $x = 0.025$ (see Fig. 6.13).

The strong increase in mobility until $x = 0.2$ can be explained by the acceleration of protons in trapping zones. Jumps into the zone, around one scandium ion and even out of the zone have migration energies that are smaller than those outside of the trapping zone ($E_{Mig,Zr-Zr-Sc} = 0.17$ eV, $E_{Mig,Zr-Sc-Zr} = 0.18$ eV and $E_{Mig,Zr-Zr-Sc} = 0.33$ eV against $E_{Mig,Zr-Zr-Zr} = 0.41$ eV). Thus, it is always beneficial for protons to be trapped and the mobility is enhanced by percolation pathways and even parts of percolation pathways. As a result of that, the conductivity is higher than in the yttrium-doped case until $x = 0.2$. There, the scandium concentration is high enough that the higher migration energies start playing a bigger role ($E_{Mig,Sc-Sc-Zr} = 0.43$ eV, $E_{Mig,Sc-Zr-Sc} = 0.61$ eV and $E_{Mig,Sc-Sc-Sc} = 0.42$ eV). This leads to a decrease in mobility with increasing dopant fraction, which

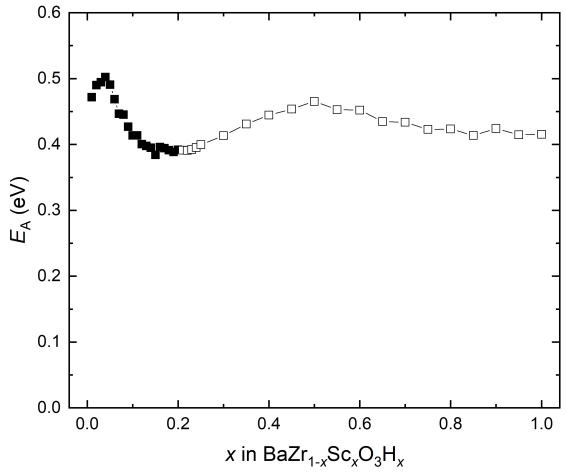


| Dopant Fraction | $E_a$ (this work) | $E_a$ (Literature) |
|---|---|---|
| 0.016 | 0.44 | 0.45[59] |
| 0.037 | 0.47 | 0.46[59] |
| 0.1 | 0.41 | 0.50[26] |
| 0.125 | 0.40 | 0.49[59] |
| 0.15 | 0.38 | 0.53[63] |
| 0.2 | 0.39 | 0.51[60] |
| 0.2 | 0.39 | 0.50[58] |

**Figure 6.14: Activation energies of the proton conductivity of scandium-doped $BaZrO_3$.** Left: All activation energies were received from Arrhenius-plots of the simulated proton conductivities of scandium-doped $BaZrO_3$ at three different temperatures: 1000 K, 700 K and 500 K. Right: Selected simulated values from this work are compared to available literature values. All activation energies in eV. Hollow symbols are used for calculations beyond the solubility limit.

is overcompensated by the growing proton concentration. In the extreme case with $x \geq 0.7$, most of the proton jumps are in the Sc-Sc-Sc configuration whose migration energy is smaller than the corresponding one from Y-Y-Y and therefore the conductivity (and even mobility) increases further in this area.

Again, activation energies of the proton conductivity in scandium-doped $BaZrO_3$ were calculated through Arrhenius-plots and compared to literature values – if available (Fig. 6.14). Our simulated activation energies are in good agreement with literature values for dopant fractions of $x = 0.016$ and $x = 0.037$. For higher fractions until $x = 0.2$, they turn out to be a little too low (around 0.4 eV against 0.5 eV). Simulations beyond the solubility limit of $x = 0.2$ show an increase in the activation energy until around 0.45 eV at $x = 0.5$. The activation energy can be explained analogously to the proton mobility: low activation energies lead to a strong increase in mobility and vice versa. The small maximum around $x = 0.05$ is explained by the building of (nanoscale) percolation pathways as in the case with yttrium-doped $BaZrO_3$.

### Indium-doped $BaZrO_3$

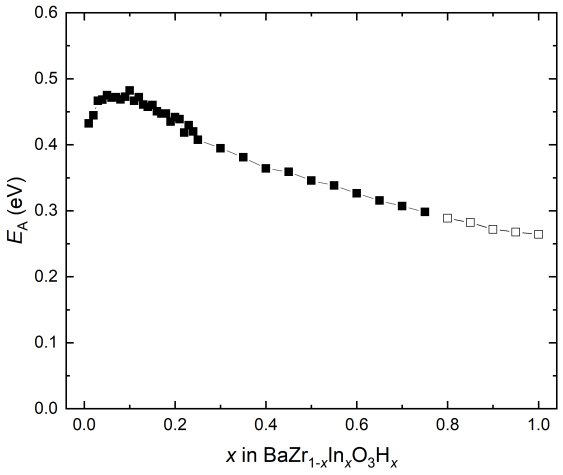


| Dopant Fraction | $E_a$ (this work) | $E_a$ (Literature) |
|---|---|---|
| 0.016 | 0.44 | 0.31[59] |
| 0.037 | 0.47 | 0.33[59] |
| 0.1 | 0.48 | 0.48[26] |
| 0.125 | 0.46 | 0.36[59] |
| 0.15 | 0.46 | 0.481[63] |
| 0.17 | 0.45 | 0.50[60] |
| 0.2 | 0.44 | 0.48[58] |
| 0.25 | 0.41 | 0.28[84] |
| 0.5 | 0.35 | 0.38[108] |
| 0.75 | 0.3 | 0.40[109] |

**Figure 6.15: Activation energies of the proton conductivity of indium-doped $BaZrO_3$.** Left: All activation energies were received from Arrhenius-plots of the simulated proton conductivities of indium-doped $BaZrO_3$ at three different temperatures: 1000 K, 700 K and 500 K. Right: Selected simulated values from this work are compared to available literature values. All activation energies in eV. Hollow symbols are used for calculations beyond the solubility limit.

Indium in $BaZrO_3$ traps protons only in 1NN with a very flat trap of −0.15 eV, again with double trapping between two indium ions. Almost no migration energy is higher than in the Zr-Zr-Zr configuration only In-Zr-Zr and In-Zr-In are in the same range ($E_{Mig,In-Zr-Zr} = 0.44$ eV and $E_{Mig,In-Zr-In} = 0.45$ eV). Therefore, no blocking effect is to be expected. In general, all these points lead to a very high proton conductivity in indium-doped $BaZrO_3$ although the mobility decreases

until around $x = 0.1$ (see Fig. 6.13). This can be explained by the trapping of protons. Because though they are not deeply trapped, the migration energy to leave the trap is one of the highest making it difficult for protons to leave the trap. This effect disappears as soon as percolation pathways are built through the crystal and the mobility of protons in indium-doped $BaZrO_3$ increases strongly between $x = 0.1$ and $x = 1$. This causes the conductivity to skyrocket up to values that are much larger than for any other dopant ion, even yttrium.

The activation energies gained from our simulations are in excellent agreement with literature, especially with experimental values (all literature references in Fig. 6.15 are experimentally measured except [59]). This is remarkable, because of the high solubility limit of indium in $BaZrO_3$ of $x = 0.75$ and our model fits well to any dopant fraction.

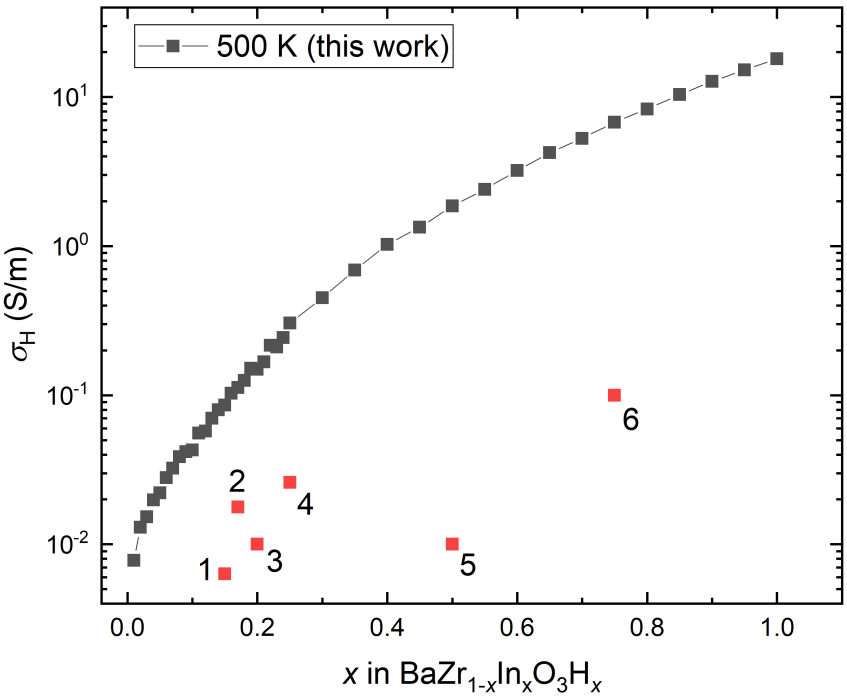


**Figure 6.16: Simulated proton conductivities in indium-doped $BaZrO_3$ in comparison with experiments.** Black symbols show the simulated proton conductivities dependent on the dopant fraction in fully hydrated indium-doped $BaZrO_3$ at 500 K from this work. They are compared to experimental studies from Imashuku *et al.*[63] (Nr. 1, at 500 K), Han *et al.*[60] (2, at 573 K), Gilardi *et al.*[58] (3, at 500 K) and Ahmed *et al.* (4[84], at 573 K, 5[108] and 6,[109] both at 500 K).

Comparing absolute values with literature, however, there are differences (Fig. 6.16). The simulation results turn out to be too high compared with experimental values by at least one order of magnitude. Nevertheless, this difference is in the same range as it was for yttrium-doped $BaZrO_3$ (compare Fig. 6.3). Hence, it is a reasonable assumption that the same reasons may apply: Samples, that are not fully hydrated, therefore, differences in the real dopant fraction could occur and the sintering process with the density and the analysis with the separation of bulk and grain boundary

conductivity is still difficult.

### Gadolinium-doped $BaZrO_3$

Gadolinium traps protons in 1NN and 2NN. Here, the simplified model analogous to the yttrium-doped case is applied with a trapping zone that is −0.39 eV deep. Migration energies are generally lower than for the yttrium-doped case, as long as configurations with more than one gadolinium ion are rare. Nevertheless, the proton conductivity is very low and the mobility is close to zero. The reason for this is the depth of the trapping zone. The only jump out of the zone is the R-Zr-Zr jump with a migration energy of 0.15 eV. Within the model, half of the depth of the trapping zone is applied to the migration energy for jumps out of the zone resulting in 0.345 eV and vice versa for jumps into the trapping zone resulting in −0.04 eV. A negative value for this migration energy means, that within the model, this position is not stable and the structure would relax spontaneously by dragging the proton back into the trapping zone. Therefore, once trapped, a proton will never again leave the trapping zone and higher values for mobility and conductivity are only observable for values of $x \geq 0.1$, where the first complete percolation pathways are built. This behaviour corresponds to the case with infinitely deep trapping zones as discussed in the chapter before.

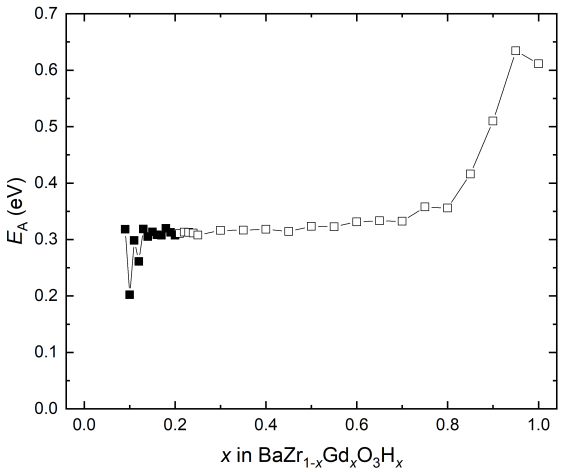


| Dopant Fraction | $E_a$ (this work) | $E_a$ (Literature) |
|---|---|---|
| 0.016 | | 0.32[59] |
| 0.037 | | 0.34[59] |
| 0.1 | 0.2 | 0.47[26] |
| 0.125 | 0.32 | 0.33[59] |
| 0.15 | 0.31 | 0.51[63] |
| 0.2 | 0.31 | 0.51[60] |
| 0.2 | 0.31 | 0.45[58] |
| 0.2 | 0.31 | 0.58[81] |

**Figure 6.17: Activation energies of the proton conductivity of gadolinium-doped $BaZrO_3$.** Left: All activation energies were received from Arrhenius-plots of the simulated proton conductivities of gadolinium-doped $BaZrO_3$ at three different temperatures: 1000 K, 700 K and 500 K. Right: Selected simulated values from this work are compared to available literature values. All activation energies in eV. Hollow symbols are used for calculations beyond the solubility limit.

With complete pathways, protons can move very quickly with very low migration energies through the simulation cell ($E_{Mig,Zr-Gd-Zr} = 0.06$ eV!) which leads to high proton conductivities and mobilities that behave qualitatively like the yttrium-doped case, just with higher values.
These low migration energies of course lead to very small activation energies from the Arrhenius-plots. Due to the trapping, it is not possible to determine activation energies for $x \leq 0.09$. For

all higher values up to the highest found dopant fraction of $x = 0.2$[81], activation energies around 0.3 eV are found which are lower than the experimental literature values of around 0.5 eV. The only study using theoretical calculations (Björketun *et al.*[59]) specifies a value of 0.33 eV in perfect agreement with our results (Fig. 6.17).

# 7

# Oxygen Vacancy Conduction

"A candle burned in this air with an amazing strength of flame; and a bit of red hot wood crackled and burned with a prodigious rapidity, exhibiting an appearance something like that of iron glowing with a white heat and throwing out sparks in all directions."

- One of the first descriptions of oxygen given by Joseph Priestley in 1775.

The conductivity of oxygen ions that are mobile via oxygen vacancies was calculated using KMC techniques as a function of the dopant fraction. Therefore, the finite-size corrected migration energies and long-range interactions were used as shown in chapter 5. Here, the so-called "dry case" was investigated. The yttrium dopant's charge is compensated by oxygen vacancies only. No protons are incorporated in this system.

## 7.1 The Dry Case

The calculated oxygen ion conductivity $\sigma_O$ (Fig. 7.1), the oxygen ion mobility $u_{O_O^\times}$ (Fig. 7.2, left) and the oxygen vacancy mobility $u_{V_O^{\bullet\bullet}}$ (Fig. 7.2, right) are analysed in dependence of the dopant fraction from $x = 0.0$ to $x = 1.0$, although dopant fractions larger than $x = 0.4$ are of academic interest only.

At the limiting case ($x = 0.0$), the ionic conductivity is necessarily zero because no oxygen vacancies are in the simulation cell and therefore no oxygen ion can move. With increasing dopant fraction, three "areas" are observable in the conductivity curve. Between a dopant fraction of $x = 0.0$ and about $x = 0.2$, an increase in conductivity can be seen that flattens and reaches a plateau. For $0.2 \leq x \leq 0.6$, the conductivity curve drops slightly for temperatures of 500 K, 1000 K and 1500 K or stays on one level (for 2000 K). In the third area at dopant fractions higher than $x = 0.6$, the conductivity increases again.

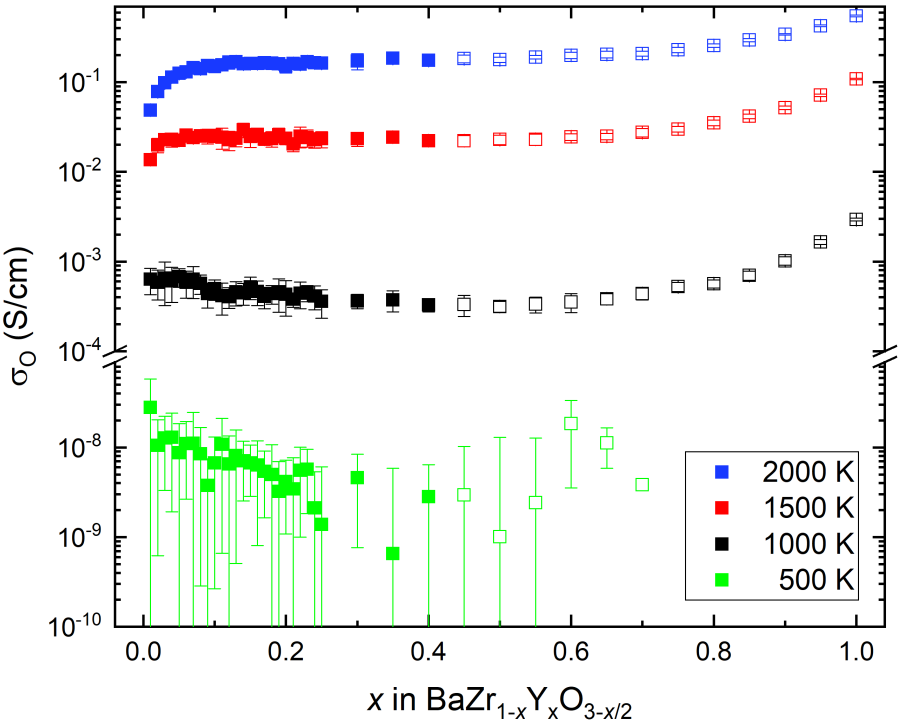


**Figure 7.1: Simulated oxygen ion conductivity in dependency of the dopant fraction in yttrium-doped $BaZrO_3$.** Finite-size corrected parameters listed in chapter 5 were used in a 16 × 16 × 16 simulation cell at four different temperatures.

The oxygen conductivity curve can always be explained from two different points of view: From the viewpoint of oxygen ions or the position of oxygen vacancies. Oxygen ions and oxygen vacancies exchange sites during the jump process, the oxygen ion conductivity can therefore be written as:

$$\sigma_O = u_{O_O^\times} \cdot c_{O_O^\times} \cdot |q_{O_O^\times}| = u_{V_O^{\bullet\bullet}} \cdot c_{V_O^{\bullet\bullet}} \cdot |q_{V_O^{\bullet\bullet}}|. \tag{7.1}$$

Since $|q_{O_O^\times}|$ and $|q_{V_O^{\bullet\bullet}}|$ are equal, the mobilities and concentrations of both species have to differ.
In the first area of figure 7.1, the initial increase of the conductivity can be explained by the increasing number of vacancies in the simulation cell. The vacancy concentration increases strongly, which leads to an increase in conductivity as well. The amount of oxygen ions however, decreases. A dopant fraction of $x = 0.2$ corresponds to $BaZr_{0.8}Y_{0.2}O_{2.9}$ and therefore a drop from 3 to 2.9 oxygen ions per formula unit. Here, the increase in conductivity is explained through the strong increase in the ionic mobility of the oxygen ions. At low fractions, most of them are immobile due to their occupied neighbouring sites, but this changes with increasing oxygen vacancy concentration.
The reason for the flattening of the curve, however, is the trapping of oxygen vacancies: If one oxygen vacancy is close to a yttrium dopant it becomes trapped, meaning, it is less likely to be moved away from it. Therefore, its contribution to the conductivity lowers. This becomes even more extreme when "deep trapping" becomes possible. Two yttrium dopants on 1NN form a deep trap with an additional energy amount of −0.22 eV (see Chapter 5). An oxygen vacancy that enters this deep trap has only a very small chance of leaving it ever again during the simulation. This can be seen at different values: A strong increase in denied Monte Carlo steps, for example, and also in an increase in site trapping in addition, because the probability of residence for oxygen vacancies is higher inside of the trapping zone. Therefore, jumps onto the deep trapped oxygen position are more likely to be chosen and when this position is already occupied, the site-blocking increases. These effects lead to the flattening of the curve and the maximum.
Additionally to the trapping, blocking comes into play with increasing dopant fraction. Table 5.9 contrasts oxygen vacancy jumps with zirconium on the central position (left side) and yttrium (right side). The migration energies on the right side are higher by 0.24 to 0.5 eV, depending on the jump environment. This means dopants do not only trap oxygen vacancies but also block their way by providing pathways with high migration energies.
Both effects – trapping and blocking – become stronger with increasing dopant fraction. Therefore, the conductivity decreases (or stagnates) at fractions higher than $x = 0.2$.
Around $x = 0.6$ though, the conductivity increases again. Around this dopant fraction, there are enough yttrium dopants in the system that complete pathways are built through the crystal. Similar to the percolation pathways for protons, these pathways allow oxygen vacancies to move from one deep trap to a neighbouring one and therefore negate their effect. Complete percolation pathways are built at a dopant fraction of about $x = 0.1$ (compare Chapter 6), but proton trapping zones range up to 2NN. Deep traps are formed in 1NN and only between two dopants. Therefore, a pathway consisting of two lanes of yttrium dopants next to each other has to be formed which takes much higher dopant fractions to be possible.
In all three areas, the oxygen ion concentration does not change that much as described above. Therefore, the oxygen ion conductivity depends almost linearly on the oxygen ion mobility. Since they depend linearly on each other ($u_{V_O^{\bullet\bullet}} = u_{O_O^\times} \cdot c_{O_O^\times}/c_{V_O^{\bullet\bullet}}$), the oxygen ion conductivity also de-

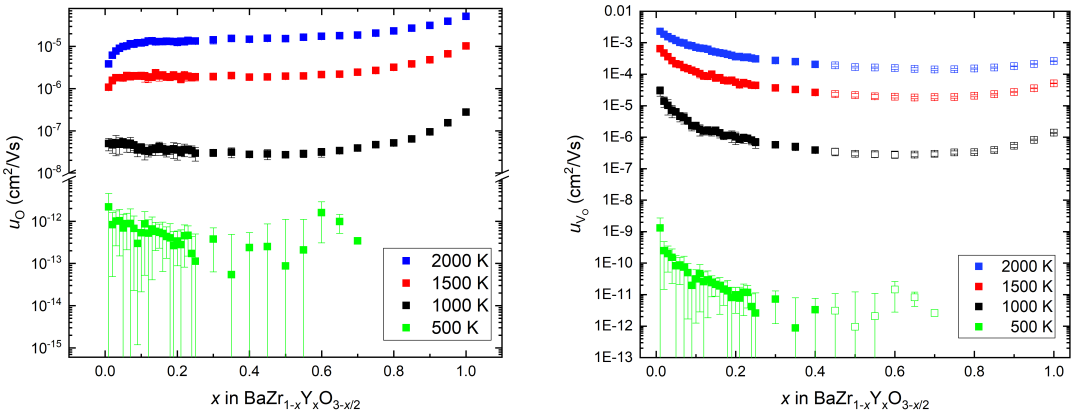


**Figure 7.2: Simulated oxygen ion mobility (left) and oxygen vacancy mobility (right) in dependency of the dopant fraction in yttrium-doped $BaZrO_3$.** Finite-size corrected parameters listed in chapter 5 were used in a 16 × 16 × 16 simulation cell at four different temperatures.

pends linearly on the oxygen vacancy mobility. It follows, that all three trends of the conductivity can be seen in the mobility as well (Fig. 7.2, left).

The oxygen vacancy mobility however, behaves differently: For very low dopant fractions, the mobility is extremely high and for increasing dopant fractions, it drops rapidly. The high initial values can be explained by the very high acceptance rates in the simulation combined with the missing deep trapping and the very low probability of site-blocking. With increasing dopant fraction, all these factors develop negatively resulting in the decreased mobility. In the first area, this can be overcompensated by the increasing concentration, resulting in an overall increase in conductivity. In the second area, this is no longer the case.

At very high fractions, in the third area, there is a slight increase again. The reason for this lies in the pathways, that are built as described above. They enable oxygen vacancies to move again.

At last, temperature-dependent KMC simulations with fixed dopant fractions of $x = 0.1$ and 0.2 were performed. Through an Arrhenius plot (see Fig. 7.3), activation energies were obtained which were compared to experimental and theoretical studies from literature (see tab. 7.1).

The simulated activation energies of the oxygen ion conductivity fit perfectly to experimental values for $x = 0.1$ and very well to those data for $x = 0.2$. The little discrepancy can be traced back to the occurrence of "deep trapping". Especially at a dopant fraction of $x = 0.2$, the probability for deep traps is high, but the probability for complete pathways, the oxygen vacancies could use, is not yet high enough. Therefore, the activation energies turn out a little higher than the experimental. Nevertheless, comparing the simulated oxygen ion activation energies to the experimental one, the agreement is comparably good as the simulated proton activation energies and their experimental values.

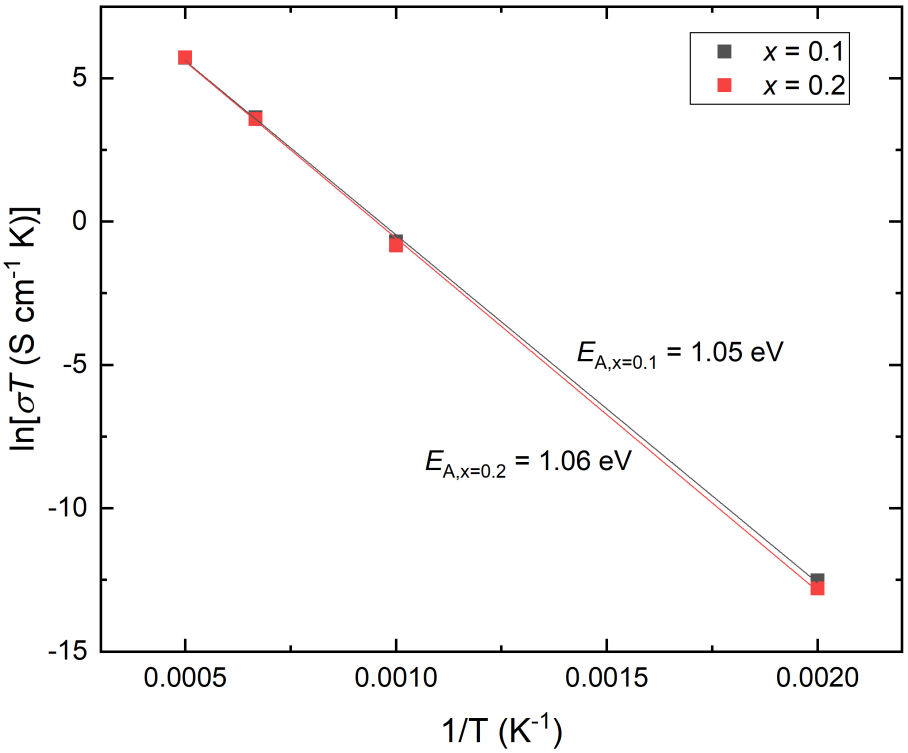


**Figure 7.3: Simulated oxygen vacancy conductivity in yttrium-doped $BaZrO_3$ depending on the inverse temperature and dopant concentration.** Finite-size corrected parameters listed in table 5.9 were used in a 16×16×16 simulation cell.

## 7.2 Other Dopant Ions

The ionic conductivity of oxygen vacancies in acceptor-doped $BaZrO_3$ was investigated for four more dopant ions, each with different properties like trapping radius, depth of the trapping zone or the migration energies. They are described in chapter 5. The conductivity and mobilities are calculated as a function of the dopant fraction (from $x = 0$ to $x = 1$) and temperature (1000 K, 1500 K and 2000 K). $BaZrO_3$ was always doped with just one dopant ion at a time, i.e. no co-doping was applied. The results are shown exemplarily for $T = 2000$ K in figure 7.4 and discussed in the following.

Generally speaking, three trends in the conductivity curves are observable: For gallium-doped $BaZrO_3$, the conductivity increases monotonously. For indium or scandium doping, the curve increases but decreases again after reaching a maximum. Finally, for yttrium or gadolinium dopants, the conductivity increases, decreases and increases again.

**Table 7.1: Activation energies of oxygen ion migration in $BaZrO_3$ in comparison to literature values.**

| $x$(Y) | $E_A$ (eV) | Method and Reference |
|---|---|---|
| 0.1 | 1.05 | DFT+KMC (this work) |
| 0.1 | 1.0 | exp.[3] |
| 0.1 | 1.1 | exp.[110] |
| 0.2 | 1.06 | DFT+ KMC (this work) |
| 0.2 | 0.93 | exp.[3] |
| 0.2 | 0.95 | DFT+MD[111] |

### Gallium-doped $BaZrO_3$

Gallium in $BaZrO_3$ builds very deep traps not only for protons but also for oxygen vacancies ($E_{trap}$ = −0.63 eV). The migration energy for an oxygen vacancy to fall into this trap is very low compared to the migration energy in pure $BaZrO_3$ ($E_{mig,Zr-Zr-Ga}$ = 0.18 eV vs. $E_{mig,Zr-Zr-Zr}$ = 0.66 eV) making it very likely for them to become trapped. Inside of the trapping zone jumps around one gallium dopant are favored ($E_{mig,Zr-Ga-Zr}$ = 0.60 eV) over jumps out of the zone ($E_{mig,Ga-Zr-Zr}$ = 0.81 eV). This leads at low dopant fractions to a decrease in oxygen vacancy mobility. This is overcompensated by the increasing number of vacancies, resulting in an increase of conductivity that is – at low dopant fractions – less steep than for all other dopants except gadolinium.

Oxygen vacancy conductivity and mobility is shown in more detail in figure 7.5. At a dopant fraction of around $x$ = 0.05, the vacancy mobility has a minimum after which it increases again. As a result, the conductivity also increases strongly and for $x \geq 0.3$ it reaches values higher than any other dopant.

This can be explained by the formation of percolation pathways or even parts of them: When gallium ions are close to each other, the trapping zones overlap and the migration energies for oxygen vacancy jumps are low ($E_{mig,Ga-Zr-Ga}$ = 0.39 eV and $E_{mig,Ga-Ga-Ga}$ = 0.35 eV). Therefore, they can move faster inside of percolation pathways especially, because they do not have to overcome the trapping energy so often. The mobility minimum occurs at dopant fractions that are too low for complete pathways. For ions, that trap in 2NN, complete pathways are built for $x \geq 0.1$ (compare proton conductivity in gadolinium-doped $BaZrO_3$). For ions that only trap in in 1NN, complete pathways occur at higher dopant fractions. Therefore, again, only parts of percolation pathways are sufficient to cause this effect.

Around $x$ = 0.2, there is a small plateau in the conductivity curve and corresponding to that, there is a local minimum in the mobility curve. Additionally, the site-blocking reaches its highest values for dopant fractions of $x$ = 0.25. Here, oxygen vacancies are somehow hindered on their way through the percolation pathways. This effect occurs in a network of parts of percolation pathways that has a bottleneck, say at one position in the path, the vacancies have to leave it. If one vacancy

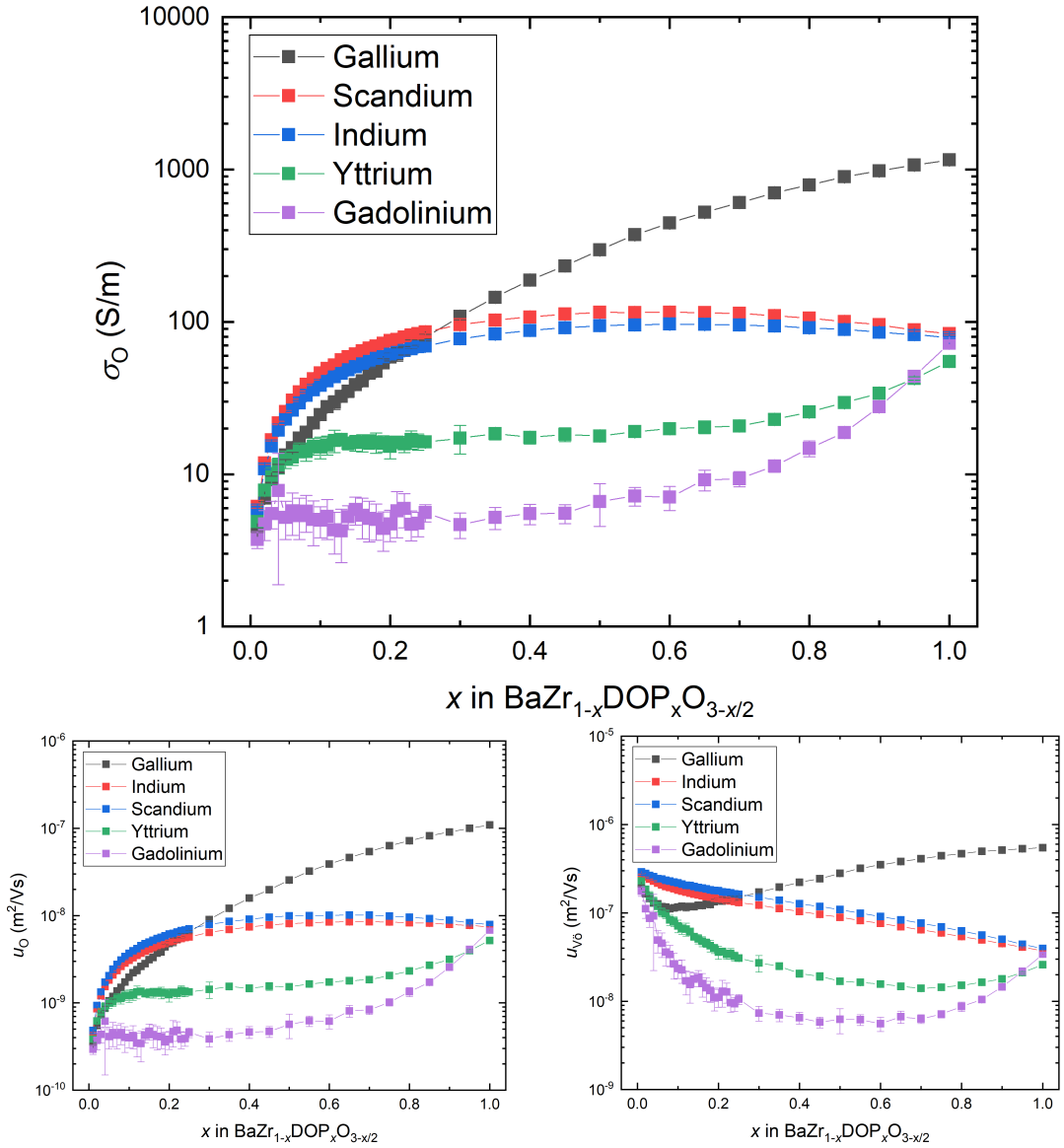


**Figure 7.4: Simulated oxygen ion conductivities and mobilities in doped $BaZrO_3$ dependent on the dopant fraction and the dopant ion.** Top: Simulated oxygen ion conductivities, bottom left: simulated oxygen ion mobilities and bottom right: Simulated oxygen vacancy mobilities. They are simulated within dry $BaZrO_3$ in a 10×10×10 supercell at $T$ = 2000 K. The lines are only a guide to the eye.

reaches this end, the jump out of the zone is much less likely than the jump of one other vacancy behind the first one. This way, the other vacancies have to wait for the first one until it completes its jump before they can move on (compare Fig. 7.6).

This works analogous to a highway, that is narrowed from three lanes to one. At this point, a traffic jam is very likely if a critical number of cars on the highway is exceeded. Here, this critical con-

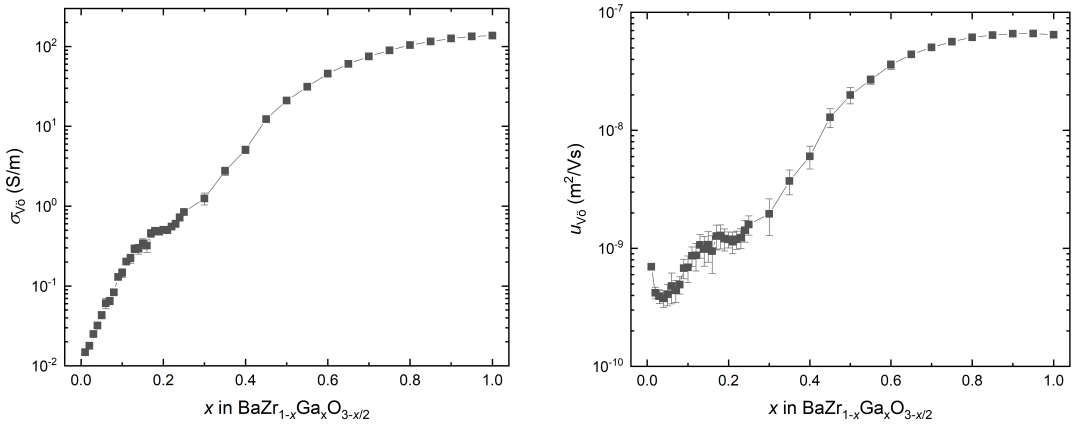


**Figure 7.5: Simulated oxygen vacancy conductivities (left) and mobilities (right) in gallium-doped $BaZrO_3$ dependent on the dopant fraction.** They are simulated within fully hydrated $BaZrO_3$ in a 10×10×10 supercell at $T$ = 1000 K. The lines are only a guide to the eye.

centration is reached at $x$ = 0.2. If the dopant fraction is even higher, the network of percolation pathways is getting denser and more alternative ways for the vacancies are given. This again leads to a strong increase in mobility and therefore conductivity until $x$ = 1.0.

The solubility limit for gallium in $BaZrO_3$ is specified at $x$ = 0.075[63] or $x$ = 0.1[75]. In this region, gallium performs worse than most other dopants, but it is sufficient enough to measure the mobility minimum. If one would find a way to improve the solubility (*e.g.* with co-doping or different synthesis routes) gallium-doped $BaZrO_3$ could work as a good oxygen conductor despite its bad proton-conducting properties.

### Scandium and Indium-doped $BaZrO_3$

Oxygen vacancy conductivity in scandium-doped $BaZrO_3$ is very similar to indium-doped $BaZrO_3$, which is, why they are summarized in one chapter. The calculations were done with only one dopant each, no co-doping was applied.

The conductivity increases strongly for low dopant fractions, reaches a maximum at around $x$ = 0.5 and decreases slightly afterwards (see Fig. 7.4). The oxygen vacancy mobility on the other hand, decreases steadily with increasing dopant fraction. This can be explained classically with trapping, blocking and the oxygen vacancy concentration. The increasing conductivity is always a result of increased oxygen vacancy concentration. The trapping of oxygen vacancies is lower than in gallium-doped $BaZrO_3$ ($E_{trap,Sc}$ = −0.25 eV and $E_{trap,In}$ = −0.32 eV) but on the other hand, both dopants block jumps around them with migration energies above 0.9 eV. Except for the Zr-DOP-DOP jump, all jumps around the dopant are blocking. Therefore, forming percolation pathways is not beneficial for the oxygen vacancy mobility and at dopant fractions above $x$ = 0.5, this can no longer be overcompensated by the increasing vacancy concentration.

The effect of blocked percolation pathways as discussed for gallium-doped $BaZrO_3$ cannot be ob-

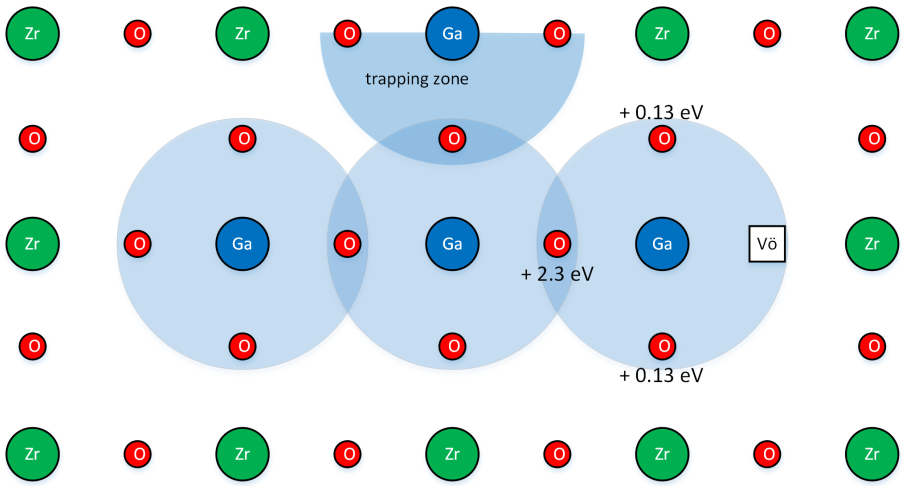


**Figure 7.6: One possible incomplete percolation pathway.** One oxygen vacancy blocks the way for all following vacancies. The numbers are energy contributions given by the vacancy only. The trapping energies are not shown explicitly. The electric field drags the vacancy to the right side. Gallium is shown in blue, the trapping zone in light blue, zirconium in green, oxygen in red and the vacancy as a black square.

served for scandium or indium-doped $BaZrO_3$ although both dopants trap in 1NN only. Here, the energy barrier for jumps out of the trapping zones is too low to cause a "vacancy jam" inside of the path. They can jump out of the pathway and reenter it later on.

### Gadolinium-doped $BaZrO_3$

Just like yttrium, gadolinium traps oxygen vacancies in 1NN and 2NN. It has the largest ionic radius and therefore also the highest blocking effect on jumps around it. The migration energy of the Zr-Gd-Zr jump is 1.19 eV and almost twice as large as the migration energy for jumps in pure $BaZrO_3$ being 0.66 eV. Additionally, a deep trapping of 0.24 eV between two gadolinium ions is found just analogous to yttrium dopants. This combination of strong trapping and blocking leads to very low oxygen vacancy conductivities (see Fig. 7.4). Even at $T$ = 2000 K, the values are significantly lower than for all other dopants. Due to the fact that the migration energies of configurations with more gadolinium ions are lower compared to the above mentioned ($E_{\mathrm{mig,Gd-Zr-Gd}}$ = 0.65 eV or $E_{\mathrm{mig,Gd-Gd-Gd}}$ = 0.83 eV), the conductivity increases at $x \geq 0.4$. The solubility limit of gadolinium, however, is around $x$ = 0.2, making this result of academic interest only.

# 8

# Vehicle Mechanism

"Travel is better with friends."
- unknown.

Parts of this chapter are subject of a previous research project from Jordy Peulen.[112]
It is generally accepted that proton transport in $BaZrO_3$ takes place by a hopping mechanism from one oxygen ion to another with a reorientation step in between. There is, however, another possible mechanism for ion transport, the vehicle mechanism. There, protons are not moving alone, but as a part of a bigger ion. It has been proposed in the early 80's by Kreuer *et al.* for proton conduction in solid lithium hydrazinium sulfate[113,114] and since then it has rarely been mentioned for crystals[115–124] and if so, for completion's sake only. It seems to have greater relevance for proton conduction in wide and open structures like zeolites and metal-organic networks often in contact with water, where larger vehicles can move around more easily and where the hopping mechanism is hindered by big distances between oxygen ions and therefore proton sites.
The vehicle, in general, can be different and it's properties depend strongly on the material. In a zeolite, for example, it might be an ammonium ion[114] or in the solid lithium hydrazinium sulfate, it could also be $N_2H_5^+$.[113] In $BaZrO_3$, the vehicle would be a hydroxide ion located on a oxygen site $(OH)_O^\bullet$. As shown in figure 8.1, three start configurations for the vehicle are possible and therefore also three end configurations. Two different transition states are found via CI-NEB depending on start and end configuration.

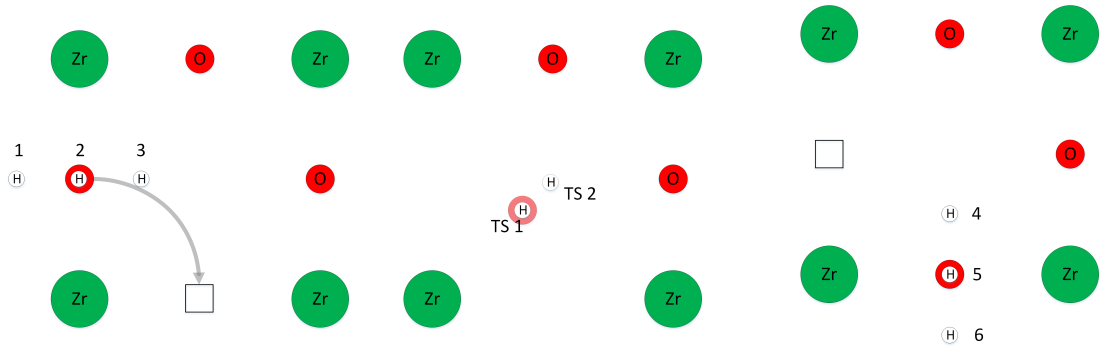


**Figure 8.1: Cut through a schematic $BaZrO_3$ unit cell showing three possible orientations of the $(OH)_O^\bullet$ vehicle.** Shown are the initial state (position 1, 2 and 3) next to an oxygen vacancy (left) and the final state (position 4, 5 and 6) (right). In the middle, the two possible transition states (TS) are drawn on the migration pathway. In position 2, 5 and TS 1, the proton is above the oxygen ion. Zirconium is shown in green, oxygen in red and proton positions in white.

Resulting from these positions and transition states, 18 vehicle jumps are possible in the undoped case (3 starting positions · 2 transition states · 3 end positions). Those could be further reduced to only two possible jumps. No vehicle jump was found from (or to) position 1. Instead, the proton first performed a reorientation jump and then the vehicle jumped from position 2. Additionally, no minimum energy pathway was found between starting position 2 and transition state 2 (TS2) or position 3 and transition state 1 (TS1). The only two remaining vehicle jumps are therefore 2-TS1-5 (in the following 2-5 jump) with a migration energy of 0.67 eV and 3-TS2-4 (in the following 3-4 jump) with $E_{mig}$ = 0.39 eV (both in the undoped case). Based on these migration energies, it is imaginable that the vehicle mechanism might play a bigger role than expected in acceptor-doped $BaZrO_3$.

The migration energy of the 3-TS2-4 jump is in the range of proton migration energies while the one of the 2-TS1-5 jump is comparable to those of oxygen vacancy jumps. This can be explained by stabilization of the transition state caused by surrounding oxygen ions. In both transition states, the proton was found to be attracted to nearby oxygen ions. In transition state 1 it was deflected to the oxygen ion above the zirconium in the bottom left corner and in transition state 2 it came closer to the oxygen ion on the right side (Fig. 8.2). In both cases, the stabilization is expected to lower the energy of the transition state.

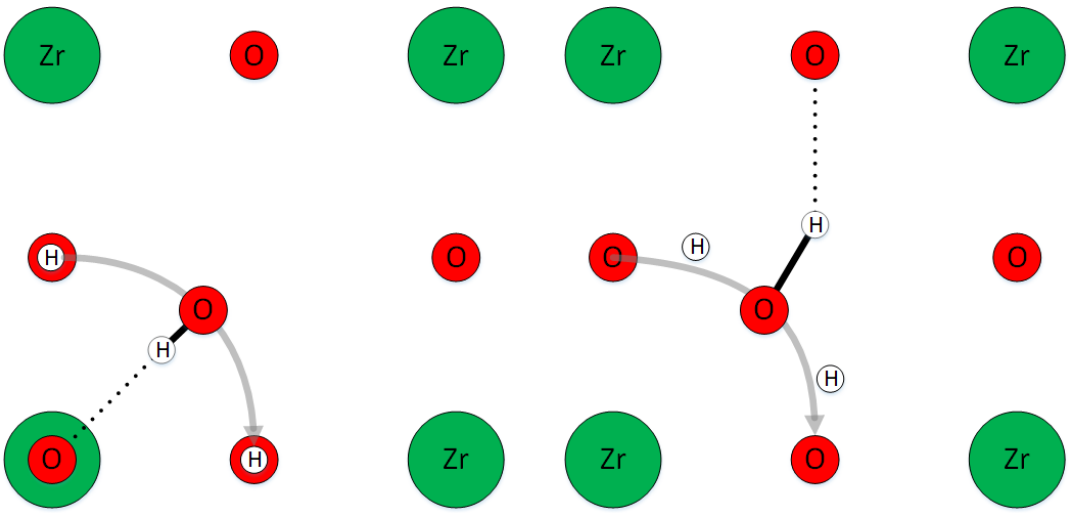


**Figure 8.2: Two possible transition states for vehicle jumps and their start and end configurations.** Left: The proton in transition state 1 is deflected in the direction of the oxygen ion above zirconium which is also deflected. Right: the proton in transition state 2 is attracted by the oxygen ion at the top. Zirconium is shown in green, oxygen in red and proton positions in white.

## 8.1 Yttrium Doping

The dependence on the dopant environment was investigated for both vehicle jumps. Therefore, zirconium was doped with yttrium on all three positions in 1NN to the jump start or end position. For both jumps, eight possible configurations were found. They correspond to proton or oxygen vacancy jumps and their nomenclature is held accordingly. In his research project, Jordy Peulen[112] calculated migration energies for vehicle jumps in the 240 atom supercell. In that supercell, however, it was not possible to calculate jumps in the Y-Y-Y configuration, which is why they were calculated in the 320 atom supercell. For comparability, all other migration energies were then calculated again in the 320 atom supercell. The results of those calculations are shown in table 8.1.
Generally, it emerges, that the migration energies of the 3-4 jump are very low and in the range or even below proton migration energies. Those of the 2-5 jump, on the other hand, are comparable to oxygen vacancy migration energies but yet, they are still lower.
The highest migration energy for vehicle jumps in pure $BaZrO_3$ with $E_{mig}$ = 0.41 eV is equal to the corresponding proton jump with $E_{mig}$ = 0.41 eV. The jump around one yttrium dopant is similar ($E_{mig,Zr-Y-Zr}$ = 0.44 eV) and thus higher than the proton counterpart but still only 1/3 of the oxygen vacancy jump. For all other 3-4 jump configurations, the migration energies drop dramatically to values around or below 0.2 eV.
Of special interest are those configurations, that are asymmetrically doped: Y-Zr-Zr and Zr-Zr-Y and Y-Y-Zr and Zr-Y-Y, respectively. Vehicle jumps away from the dopant ion are energetically favoured ($E_{mig,Y-Zr-Zr}$ = 0.10 eV) over those towards the dopant ($E_{mig,Zr-Zr-Y}$ = 0.14 eV), meaning,

that the trapping of the particle moving in the opposite direction, namely the oxygen vacancy is dominating this jump.

At this point, our model reaches its limits, because the energetic difference of one oxygen vacancy in 1NN and 2NN to a yttrium ion is −0.08 eV (compare chapter 7) and not only −0.04 eV as the difference in migration energies implies. This difference can be traced back to the missing finite-size correction for the vehicle jumps. Therefore, for the KMC simulations, an assumption is made and an energy difference of -0.08 eV is applied resulting in $E_{\mathrm{mig,Y-Zr-Zr}} = 0.08$ eV and $E_{\mathrm{mig,Zr-Zr-Y}} = 0.16$ eV. Since both energies are still very low, no major influence on the KMC outcome is expected. The difference in migration energies between Y-Y-Zr and Zr-Y-Y jump is 0.11 eV, which also fits the model well and again, the oxygen vacancy interaction dominates. With $E_{\mathrm{mig,Zr-Zr-Y}} = 0.16$ eV and $E_{\mathrm{mig,Zr-Y-Y}} = 0.30$ eV for the vehicle jump from 1NN to 2NN, and vice versa for the vacancy, both jumps are very likely, especially when comparing them to the corresponding oxygen vacancy jump with 0.54 eV or 1.04 eV.

The same applies to Y-Y-Y jumps. The migration energy $E_{\mathrm{mig,Y-Y-Y}} = 0.18$ eV is extremely low, both compared to the corresponding proton or oxygen vacancy migration energy. The vehicle seems to be able to move very easily in this environment.

This is brought to extremes in the Y-Zr-Y jump, whose migration energy could not be calculated. The CI-NEB as implemented in VASP failed to find the transition state independent of the supercell size, the number of images or the convergence criteria. This is because in all cases, the energy of the transition state was found to be lower, than the one of the start or end configuration. This makes the result physically not sensible and in all cases brought the calculation to crash. Therefore, no migration energy is given and this jump is excluded from the KMC simulation.

Migration energies for all 2-5 jump configurations are generally higher than those for 3-4 jumps. The migration energy of the Zr-Zr-Zr jump ($E_{\mathrm{mig,Zr-Zr-Zr}} = 0.69$ eV) corresponds very well to the Zr-Zr-Zr jump of one oxygen vacancy. Here also, all asymmetric configurations show the same peculiarity as 3-4 jumps: The migration energies of jumps away from the dopant are lower than those of jumps towards it. Again, with minor adjustments, the energy model can be applied and even the deep trapping with one vacancy between two yttrium dopants is well depicted. The jump of one oxygen vacancy between two yttrium dopants is energetically favoured ($E_{\mathrm{mig,Y-Y-Zr}} = 0.56$ eV) over the Zr-Y-Y jump of the vehicle ($E_{\mathrm{mig,Zr-Y-Y}} = 0.76$ eV). Oxygen vacancies that are deeply trapped, could escape more likely via a vehicle jump than via a oxygen vacancy jump with 1.04 eV.

**Table 8.1: Migration energies for vehicle jumps in yttrium-doped $BaZrO_3$.** All eight possible permutations of the occupation of the zirconium sites in the first nearest neighbourhood of the initial and final positions of the translation jump of both possible vehicle jumps. Zirconium is shown in green, yttrium in blue, oxygen in red, the oxygen vacancy is a black square, the proton is white and the proton's final position is gray. The corresponding migration energies were calculated explicitly by means of DFT in a 320 atom supercell. For explanation concerning the *, see text.

| Y-Doping 3-4 jump | $E_{mig}$ /eV | Y-Doping 2-5 jump | $E_{mig}$ /eV |
|---|---|---|---|
| 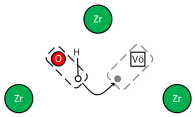 | 0.41 | 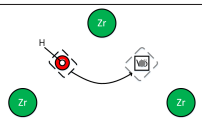 | 0.69 |
| 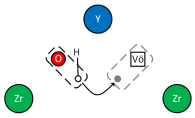 | 0.44 | 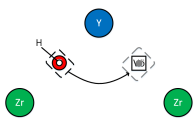 | 0.89 |
| 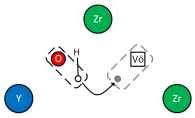 | 0.10 | 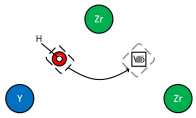 | 0.49 |
| 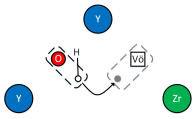 | 0.19 | 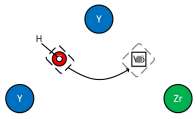 | 0.56 |
| 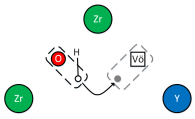 | 0.14 | 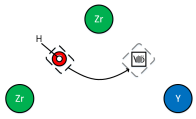 | 0.65 |
| 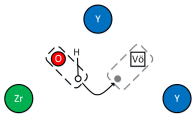 | 0.30 | 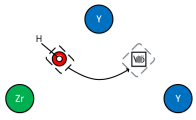 | 0.76 |
| 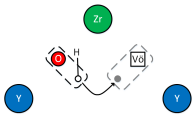 | * | 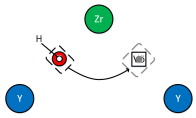 | 0.41 |
| 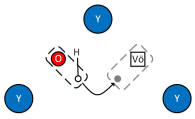 | 0.18 | 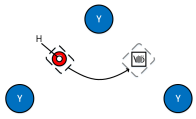 | 0.53 |

## 8.2 Dissociation Jump

With DFT calculations, it was found that the vehicle could dissociate during the jump. While both ions start the jump together, the oxygen ion jumps to the oxygen vacancy and the proton to another oxygen ion in 1NN. Figure 8.3 shows two "dissociation jumps" where the vehicle splits up into one oxygen ion and one proton. On the left-hand side in figure 8.3, the dissociation during the 2-5

jump is shown. The proton is already attracted to the oxygen ion above the zirconium ion anyway. Therefore, it is an energetically small step to leave the vehicle: $E_{mig,2-5,diss}$ = 0.47 eV instead of $E_{mig,2-5}$ = 0.69 eV. This migration energy for the dissociation is lower than most of the 2-5 jumps and should, therefore, be favoured.

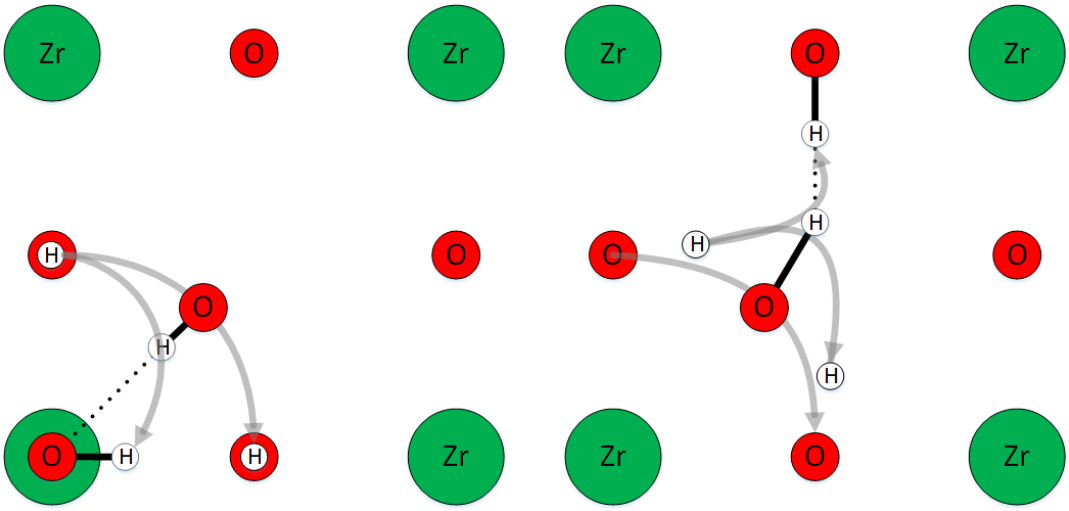


**Figure 8.3: Two possible "dissociation jumps", that were found in $BaZrO_3$.** Left: Dissociation during one 2-5 jump. Right: Dissociation during one 3-4-jump. The intended paths of oxygen and protons are shown as well as the actual pathway, the protons took in the dissociation. Zirconium is shown in green, oxygen in red and the proton in white. Calculations were performed in a 320 atom supercell via DFT.

The same applies to the 3-4 jump (Fig. 8.3, right), where the proton dissociates to one other oxygen ion in the plane with a migration energy of $E_{mig,3-4,diss}$ = 0.24 eV instead of $E_{mig,3-4}$ = 0.41 eV. Here, the dissociation should be favoured as well.
From that, it can be assumed that it is more likely for the vehicle to perform one dissociation jump than one normal vehicle jump. In many cases, not even one jump will be performed as the dissociation for example at 1000 K is 7 (3-4-jump) to 13 (2-5-jump) times more likely.

## 8.3 Vehicle Jumps in KMC Simulations

Because even without dissociation jumps, the vehicle can form during the simulation and separate again and that multiple times. To keep counting the steps of every single species on its own and together is a difficult task. Therefore, until today, the implementation of the vehicle mechanism in Mocassin is still experimental and although some tests were done all influences of vehicle jumps in KMC simulations in yttrium-doped $BaZrO_3$ in the following are hypothetical.
KMC simulations with protons and oxygen vacancies at the same time revealed that protons move much faster in the crystal and that they are not influenced by the presence of oxygen vacancies

(see Chapter 9). It is a necessary condition for one vehicle jump, that a vehicle forms next to an oxygen vacancy and additionally, neither the proton nor the oxygen vacancy may be selected for a ion jump before the vehicle moves. The probability of such a configuration forming up, is low compared to the number of configurations in which a proton could jump on its own. Therefore, it is not to be expected that the consideration of vehicle jumps does change anything significantly for proton conductivity or mobility. Protons will sometimes jump with one vehicle and far more often without one.

For oxygen ions and vacancies, on the other hand, things are different. The probability that a vehicle forms next to an vacancy is still low, but the huge difference in migration energies between the 3-4 vehicle jump and the oxygen vacancy jumps makes the acceptance of vehicle jumps very likely. As written above, it is a reasonable assumption that vehicle jumps are a way of de-trapping oxygen vacancies from yttrium ions, because the 3-4 Zr-Zr-Y jump with $E_{\mathrm{mig,Zr-Zr-Y}} = 0.14$ eV is very likely to happen and leads the vacancy away from the dopant. The probability that the vehicle is chosen again and performs the back jump is very low and if the vacancy is chosen and tries to jump to the yttrium in 1NN again, this would lead to a configuration with one proton next to a vacancy, which is energetically very unfavourable. That way, vacancies can be "forced" away from dopants.

This could play a role in simulations with many oxygen vacancies and consequently only few protons, where the probability of forming one vehicle next to an oxygen vacancy is highest.

# 9

# Mixed Ion Conduction

"Denn auf Mischung kommt es an."
- Johann Wolfgang von Goethe, German writer in "Faust".

Parts of this chapter are based on the research project of Isabel Sommerfeld.[125]
When $BaZrO_3$ is doped with yttrium, oxygen vacancies are built and protons can be brought into the system. When we ignore electron holes, both can compensate the dopant's charge. The limiting cases, the fully hydrated case and the dry case have now been discussed in great detail, but it is also imaginable – and in the experiment much more likely – that both, protons and oxygen vacancies coexists in the crystal. Both species move and therefore conduct ionic charge. In the following, the interplay between both species is investigated further. Therefore, simulations with these two species, being mobile at the same time, are performed and analysed. Though simulating both at once, the analysis will again be split up into two parts: protons and oxygen vacancies.
The thermodynamic behind it, which controls the ratio between protons and oxygen vacancies at a given temperature, cannot be predicted and is still unknown. The concentration of protons and oxygen vacancies is temperature dependent and still under investigation. Therefore, in this chapter, another approach is made: Many possible combinations of proton and oxygen vacancy concentrations are investigated. In this way, by varying the dopant fraction and the degree of hydration, a systematic grid is set up. At each point of the grid, the proton and oxygen ion conductivity is calculated as well as the proton, oxygen ion and oxygen vacancy mobility. This allows us to discuss

general trends and to lay a foundation for future work when the temperature dependence is known. Following equation 2.8, the total ionic conductivity can be written as the sum of the partial conductivities, in this case:

$$\sigma_{\text{Total}} = \sigma_{\text{H}} + \sigma_{\text{O}}. \tag{9.1}$$

The calculations are performed at 1000 K, which is a compromise between the high temperatures, oxygen vacancies need to be mobile and low temperatures, needed for high proton concentrations, because the solubility of water decreases with increasing temperature. Nevertheless, it is to expect that $\sigma_{\text{Total}}$ is dominated by the proton conductivity $\sigma_{\text{H}}$, which is at least one order of magnitude higher than the oxygen ion conductivity $\sigma_{\text{O}}$ from the same simulation. This is, why $\sigma_{\text{Total}}$ is not shown here and the analysis starts with $\sigma_{\text{H}}$.

## 9.1 Proton Conductivity and Mobility

In figure 9.1, the dopant fraction is varied as before at degrees of hydration ranging from $\alpha = 0.0$ to 1.0 in steps of 0.1. The dependence of $\sigma_{\text{H}}$ on the dopant fraction has been explained in detail in chapter 6 and stays the same for values of $\alpha$. With an increasing degree of hydration, an increase in conductivity is observable.

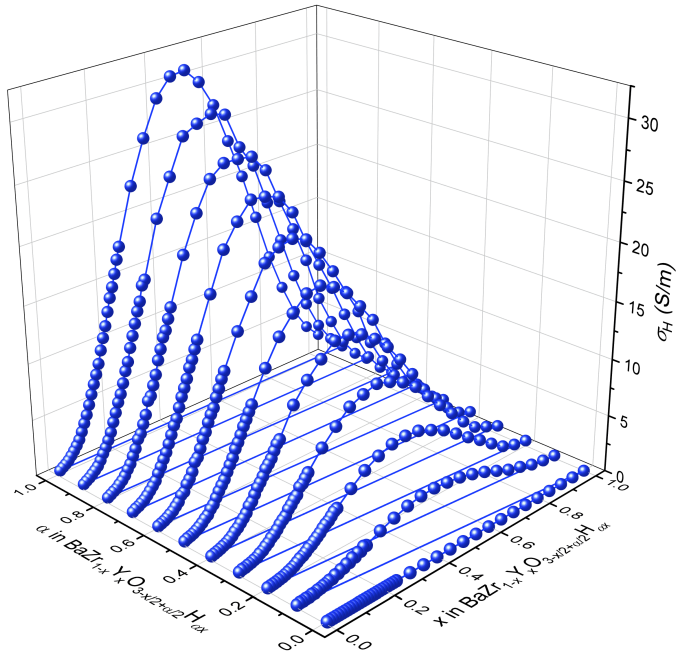


**Figure 9.1: Simulated proton conductivities in yttrium-doped $BaZrO_3$ dependent on the dopant fraction *x* and the degree of hydration $\alpha$.** They are simulated within the model as described in chapter 5 in partially hydrated $BaZrO_3$ in a 10×10×10 supercell at $T = 1000$ K. The lines are a guide to the eye, only.

This can be explained by equation 2.8: if the protons mobility and charge stayed the same, and the concentration changed, then the conductivity would change linearly as well. If the degree of hydration is raised from 0.1 to 0.2, the proton concentration doubles and so does the conductivity (at the same dopant fraction).

The assumption of constant proton mobility is checked in figure 9.2. The mobility is plotted for different degrees of hydration over varied dopant fractions in the same figure. Within the error bars, they are in good agreement. Therefore, the proton mobility is not dependent on the degree of hydration and can be seen as constant.

This leads to the conclusion that protons are not hindered at all by oxygen vacancies in the crystal. The presumption that vacancies could block percolation pathways due to their repellent properties against protons is wrong. Protons are that much faster than oxygen vacancies that they can easily circumvent them.

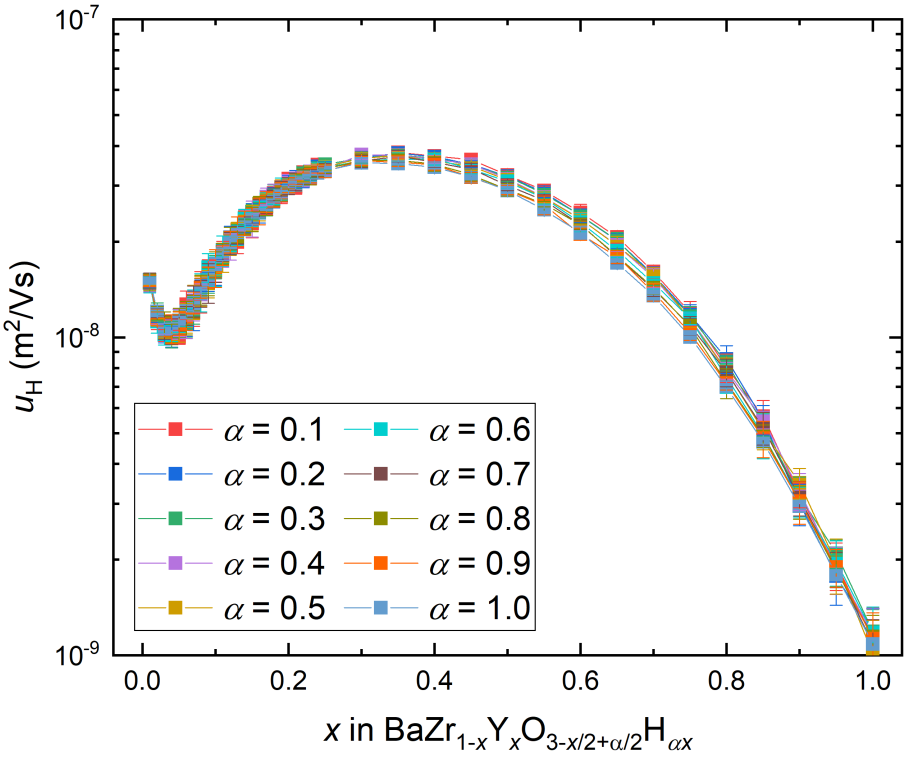


**Figure 9.2: Simulated proton mobilities in yttrium-doped $BaZrO_3$ dependent on the dopant fraction $x$ and the degree of hydration $\alpha$.** They are simulated within the model as described in chapter 5 in partially hydrated $BaZrO_3$ in a 10×10×10 supercell at $T$ = 1000 K. The lines are a guide to the eye, only.

## 9.2 Oxygen Vacancy Conductivity and Mobility

Due to their higher migration energies, oxygen vacancies are generally slower than protons and their contribution to the ionic conductivity therefore is by about two orders of magnitude smaller. Figure 9.3 shows the simulated oxygen vacancy conductivities and mobilities.
With increasing degree of hydration and thus decreasing oxygen vacancy concentration, the oxygen ion conductivity decreases. This can only partially be explained by the decrease in the number of charge carriers. This explanation is not sufficient, because the decrease in conductivity is stronger than it was to be expected. For example from $\alpha$= 0.0 to 0.9, the oxygen vacancy concentration drops to 10 %, but the ionic conductivity drops by 1.5 to 2 orders of magnitude.
Additionally, the mobilities for oxygen ions and vacancies both decrease as well. It follows that oxygen vacancies are hindered on their way through the crystal. There are two reasons imaginable for this:

1. protons block oxygen vacancies. There is an energy of 2.3 eV that a proton has to overcome to jump next to an oxygen vacancy. This leads to a configuration where the energy of the transition state is lower than the energy of the final state. Thus, this is treated as an unstable state, the jump is rejected and the start configuration is restored.
   This can also take place the other way around: If one oxygen vacancy tries to perform a jump that would end next to a proton, this jump is also immediately rejected.
   Despite the fact that it is contra-intuitive to understand that the fast protons can block the slower oxygen ions, this is a valid explanation in the simulation that knows no ionic mass. The higher the proton/oxygen vacancy ratio, the more likely this scenario will be and the strongest decrease in mobility can be seen at the highest values of $\alpha$.

2. the relatively larger number of dopant ions and therefore trapping zones has a negative effect. With increasing dopant fraction, the probability for deep traps (see chapter 7) increases. Additionally, yttrium dopants block oxygen vacancy jumps due to their higher migration energies. The higher $\alpha$, the higher is the dopant ion/oxygen vacancy ratio and therefore also the probability for vacancies to be trapped and blocked.

Both effects are plausible explanations for the lowering of the oxygen vacancy mobility. If protons block oxygen vacancies, the number of jumps that are rejected because of an unstable end configuration would increase and if the dopant ions more often trapped and blocked the oxygen vacancies, the number of rejected jumps would increase. Both effects apply and due to the large error bars, it is impossible to say which one dominates.

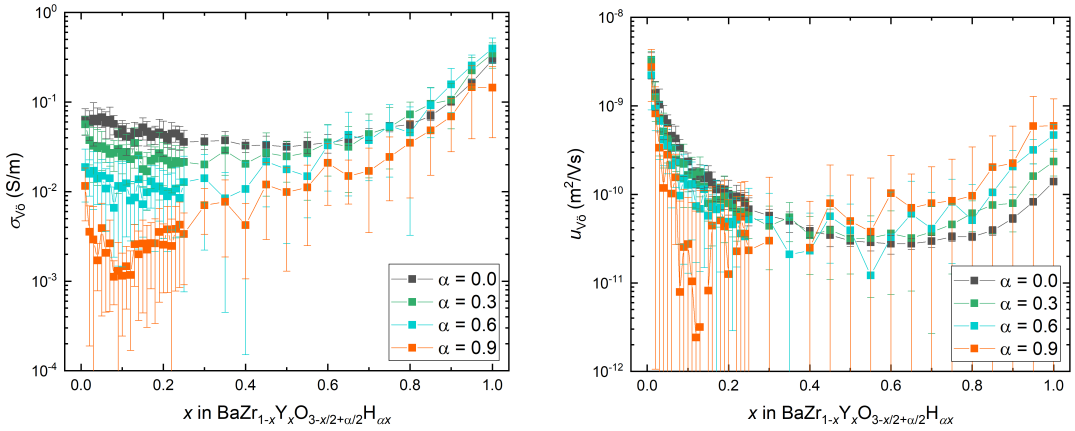


**Figure 9.3: Simulated oxygen ion conductivities (top), oxygen ion mobilities (bottom, left) and oxygen vacancy mobilities (bottom, right) in yttrium-doped $BaZrO_3$ dependent on the dopant fraction $x$ and the degree of hydration $\alpha$.** They are simulated within the model as described in chapter 5 in partially hydrated $BaZrO_3$ in a 10×10×10 supercell at $T$ = 1000 K. The lines are a guide to the eye, only.

## 9.3 Transference Numbers

The ion transport or transference numbers are a measure of the charge transported by each ion. The protons transference numbers are calculated according to:

$$t_H = \frac{\sigma_H}{\sigma_{Total}}. \tag{9.2}$$

From the simulations, the proton transference number can be easily calculated and the results depending on dopant fraction and degree of hydration are shown in figure 9.4. In almost every simulation that included protons, $t_H$ is very close to 1. This was expected because of the much higher mobility and conductivity of the protons. Only in simulations with very low values of $\alpha$ and very low dopant fractions, the oxygen transference number would play a role at all.

## 9.4 Other Dopants

Since it takes a large number of simulations and therefore large effort, simulations of gallium, indium, scandium and gadolinium-doped $BaZrO_3$ were carried out of just one degree of hydration in the first place. For that, $\alpha$ = 0.2 was chosen arbitrarily, and compared to $\alpha$ = 0.0 and $\alpha$ = 1.0. Here, proton conduction in gallium takes a special place (Fig. 9.5). Three particularities attract attention and are explained in the following.

1. Shifting of the conductivity maximum to lower dopant fractions.
   In fully hydrated gallium-doped $BaZrO_3$, the maximum in conductivity occurs at $x$ = 0.2

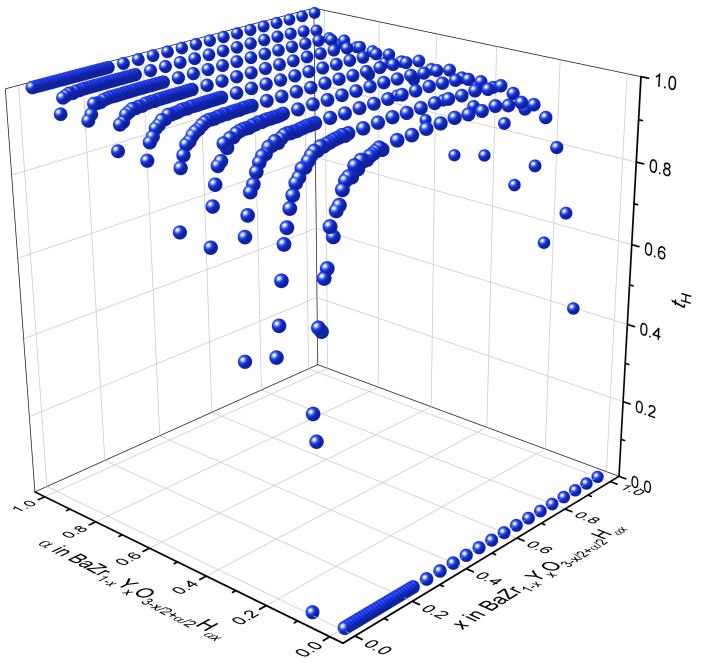


**Figure 9.4: Calculated proton transference numbers in yttrium-doped $BaZrO_3$ dependent on the dopant fraction $x$ and the degree of hydration $\alpha$.** Simulations were performed within the model as described in chapter 5 in partially hydrated $BaZrO_3$ in a 10×10×10 supercell at $T = 1000$ K.

while the (local) maximum in conductivity for $\alpha = 0.2$ occurs at $x = 0.12$. At $x \leq 0.12$, the differences in both curves can be explained by the number of charge carriers: A five times higher proton concentration leads to a just as high increase in conductivity. The concentration of ions is low enough in both cases that no difference can be noticed. This changes around $x = 0.12$. Here, the higher number of traps strengthens the trapping effect. The probability for every proton to become trapped on its way is the same in both cases but there are fever protons in the system. Therefore, every proton that is trapped and does contribute less to the conductivity matters more. This is also expressed in a stronger decrease in proton mobility between $x = 0.12$ and 0.35 (Fig. 9.5, right).

2. Shifting of the conductivity minimum to lower dopant fractions.
   At $x = 0.25$ (for $\alpha = 0.2$) or $x = 0.4$ (for $\alpha = 1.0$), respectively, there is a minimum in the conductivity. As described in chapter 6, the proton conductivity increase is caused by protons that are kept outside of the trapping zones by site blocking of the protons inside. Protons outside cove faster due to the lower migration energies. At $\alpha = 0.2$, protons are not only kept outside by other protons but by oxygen vacancies that repel them. At lower dopant fractions, this effect is caused by oxygen vacancies than with protons. Although oxygen vacancies are

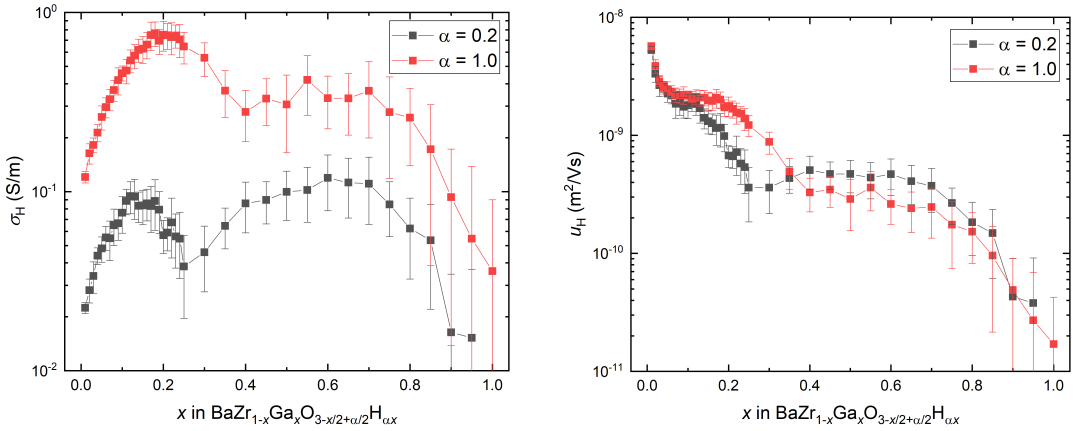


**Figure 9.5: Simulated proton conductivities (left) and mobilities (right) in gallium-doped $BaZrO_3$ dependent on the dopant fraction and the degree of hydration.** They are simulated within in fully hydrated $BaZrO_3$ in a 10×10×10 supercell at $T$ = 1000 K. The lines are only a guide to the eye.

very mobile in gallium-doped $BaZrO_3$, this is insufficient as an explanation, since the pure number of charge carriers is lower and their mobility is not higher than the one of the protons. A possible explanation is treating it like an overlay of two effects that are independent of each other: The trapping of protons, which leads to a maximum and decrease in conductivity and the site blocking that leads to an increase. If the first effect is strong as described above, the increase and decrease appear at lower dopant fractions. Therefore, the impact of the second effect is visible earlier. This is also supported by the fact that the mobility at $\alpha$ = 0.2 is lower than at $\alpha$ = 1.0 until $x$ = 0.4

3. Stronger increase in conductivity at high dopant fractions.
   The ionic conductivity at $\alpha$ = 0.2 increases strongly at high dopant fractions with a global maximum at $x$ = 0.6. At $\alpha$ = 1.0, this rise turns out weaker and with only a local maximum. Additionally, in the fully hydrated case, the proton mobility turns out lower at $x \geq 0.4$. Hence, oxygen vacancies are more efficient in keeping protons out of the trapping zones. The reason for that cannot be explained, yet.

Oxygen vacancies in gallium-doped $BaZrO_3$ are very mobile and only marginally affected by the presence of protons. Their mobility is slightly lower at $\alpha$ = 0.2 than in the dry case. This is caused by the cases where one oxygen vacancy is repelled by one proton (most likely inside of the trapping zones). Therefore, the oxygen vacancy conductivity is also slightly lower at $\alpha$ = 0.2. Other than that, there are no notable differences.

Indium traps protons in $BaZrO_3$ in 1NN, just like gallium. Nevertheless, within the error bars, no difference in proton mobility between the fully hydrated case and the one with $\alpha$ = 0.2 is observable. The proton conductivity is lowered by a factor of 5 according to the differences in proton

concentration. It follows that the trapping effect in indium-doped $BaZrO_3$ is too low and protons can leave the trapping zones too easy to cause noticeable effects on the conductivity. The same applies – again within the error bars – for the oxygen vacancy mobility. They are unaffected by the presence of protons similar to gallium-doped $BaZrO_3$. Therefore, the oxygen vacancy conductivity is lowered by a factor of 5 according to the lower concentration of vacancies.
In scandium-doped $BaZrO_3$, the proton mobility is slightly lower at $\alpha = 0.2$. This can be explained by proton trapping that is higher than that of indium but lower than for gallium dopants. Therefore this can be seen as a "intermediate case". Here, effects as described above start to play a role but the effects are not comparably strong.
The oxygen vacancy mobility in scandium-doped $BaZrO_3$, however, is the same (within the error bars) as in the dry case. Due to the lower concentration of vacancies, the oxygen vacancy conductivity is decreased. On the other side, the concentration of oxygen ions does change even less, than in the dry case. Therefore, the oxygen ion mobility decreases, since it is less likely for one ion to be moved during the simulation.
In gadolinium-doped $BazrO_3$, there is no difference observable within the error bars for all mobilities. Therefore, all differences in conductivity can be traced back to the changes in concentration.

# 10

# Further Investigations

"Ich beschäftige mich nicht mit dem, was getan worden ist. Mich interessiert, was getan werden muss."

- Marie Curie, physicist, chemist and two-times Nobel Prize winner.

In this chapter, some further investigations are discussed that were done on acceptor-doped $BaZrO_3$ and did not fit in any other chapter. It has been said in chapter 5 that the choice of the supercell is of crucial importance for DFT calculations. Here, it is shown that even *within the same supercell*, different results can be calculated depending on the parameters. The oxygen ions build octahedrons around the zirconium position and the incorporation of one proton or vacancy causes a tilting of them. For cubic supercells with an odd multiplier, the periodic boundary conditions prevent this tilting but in supercells with an even multiplier, the tilting can be differently strong. The principle is shown in figure 10.1.[126]

To demonstrate this, DFT calculations were performed with the same starting configuration. The only different parameter was the convergence criterion of the electronic relaxation that was set to $10^{-3}$ eV and $10^{-5}$ eV, respectively. The calculation with $10^{-3}$ eV will be referred to as the "rough" calculation, whereas the other one as the "precise" one. Figure 10.2 shows the energy of the supercell during the geometry optimization for the precise calculation. At an absolute energy of -2962.97 eV convergence was reached. The rough calculation, however, stopped at -2962.64 eV, 0.33 eV higher. In both cases, VASP stated that the cell was completely relaxed and the calculation did not fail.

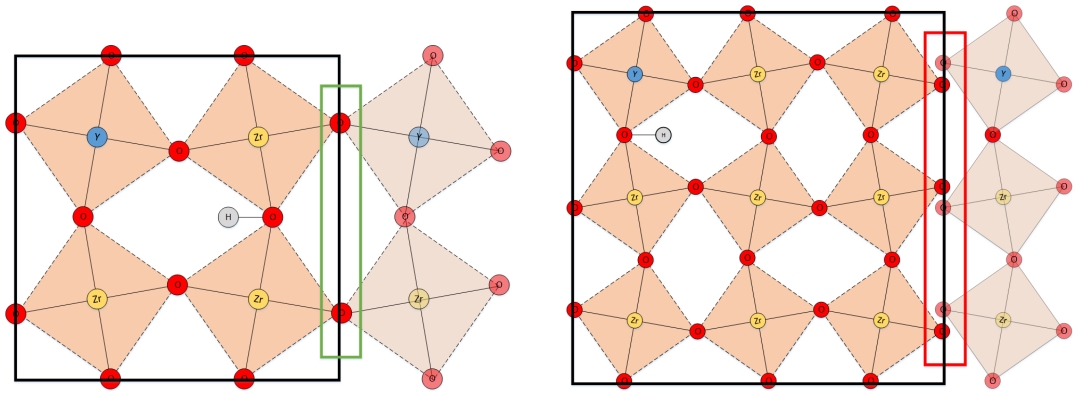

**Figure 10.1: 2D-projection of a 2×2×2 (left) and a 3×3×3 (right) supercell.** The octahedral tilting is exaggerated to show the principle. Oxygen is shown in red, zirconium in yellow, yttrium in blue and protons are grey. The oxygen octahedra are shown in orange. The box shows that octahedral tilting is possible while satisfying periodic boundary conditions in a 2×2×2 and impossible in a 3×3×3 supercell.[126]

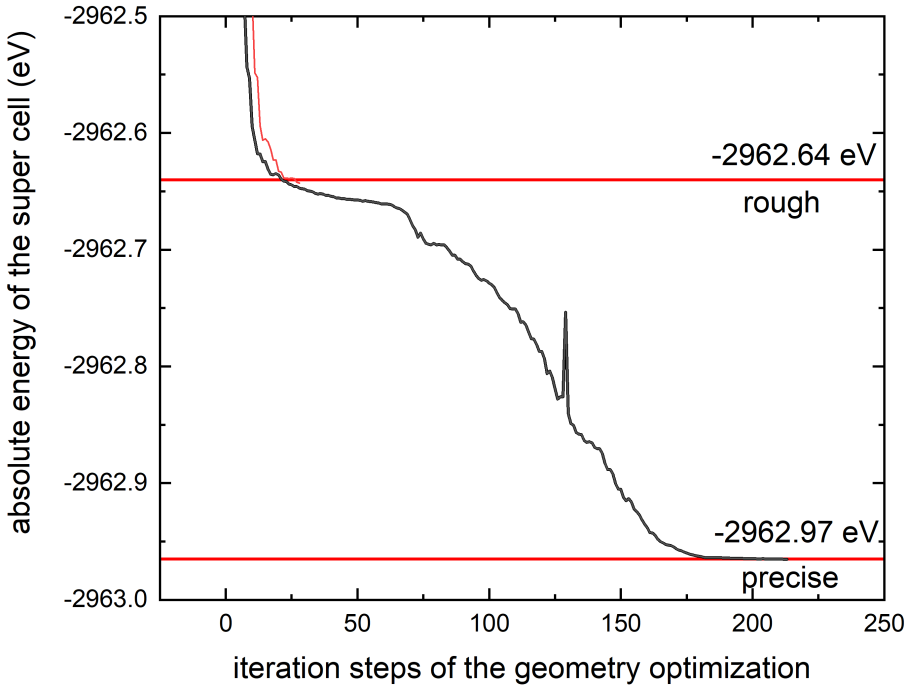


**Figure 10.2: Absolute energy of the supercell of a 4×4×4 supercell with two yttrium ions and one proton.** All defects are at least 10 Å away from each other. The convergence criterion of the electronic relaxation was $10^{-5}$ eV and the lower red line shows the energy value where the precise calculation converged. Additionally, the corresponding rough calculation is also shown (upper line).

It is visible that the energy course for the 'precise' calculation in figure 10.2 is very flat between step 25 and 75. Here, the tilting takes place. The energy difference between two calculation steps in this area are small enough that the convergence criterion for the rough calculation is reached. "Later" at a higher step count, the energy landscape becomes steeper before reaching the convergence criterium of the 'precise' calculation.

The energy difference between rough and precise calculations can be quantified and plotted for different configurations that all contain one proton and two yttrium dopants at different distances to each other in a 4×4×4 supercell (Fig. 10.3 (left)). In every configuration, large energy differences are found. They vary between 0.03 eV (2NN-3bNN) and 0.44 eV (3NN-3aNN) and no trend is observable. It seems that the differences are smaller when all defects are close to each other (1NN-1NN, 1NN-2aNN and 1NN-2bNN) but even in this case they are always lager than 0.05 eV, which is significantly higher than the calculation error and therefore cannot be ignored.

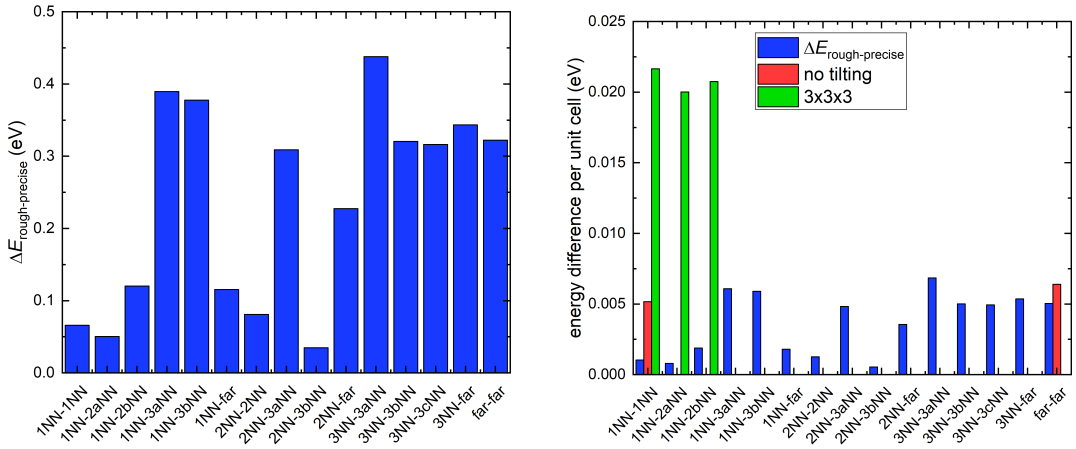


**Figure 10.3: Energy differences and energy differences per unit cell.** Left: The energy difference between rough and precise calculations with the defect ions being on different distances to each other. Right: The energy differences per unit cell between rough and precise calculation (blue), between "no tilting" and precise (red) and between "3×3×3" and precise (green) are shown. The first term depicts the H-Y1 neighborhood and the second the one between H and Y2. For example 1NN-1NN means that both yttrium ions are in 1NN to the proton. "far" means that the distance between the respective defects is larger than 10Å. All energies were calculated by means of DFT.

These differences become particularly important when browsing DFT literature data on acceptor-doped $BaZrO_3$. Several publications used – undoubtedly to accelerate the calculations – rough parameters,[106,127–132] many that used precise (or better) parameters[13,82,83,133–145] and some that are in between.[146,147] Data, calculated with different precisions should be compared with great care since the differences might be large as shown in figure 10.3 (left).

Since they can be calculated very fast, many groups use 3×3×3 supercells for DFT calculations in doped $BaZrO_3$. The deviation between precise calculations in a 4×4×4 supercell and those can only be approximated. Therefore, two possible approximations are used here:

1. In the first approximation, a 3×3×3 supercell with the same defect configuration as in the 4×4×4 supercell is calculated. Due to the smaller size of this supercell, only calculations with the configurations 1NN-1NN, 1NN-2aNN and 1NN-2bNN could be performed. This method is referred to as "3×3×3".

2. In the second approximation, a 4×4×4 supercell is used and some zirconium ions are fixed in position during the simulation (marked red in Fig. 10.4). This approximates the missing possibility of octahedral tilting in a 3×3×3 supercell. The advantage of this method lies in the correct number of atoms and it is referred to as "no tilting"

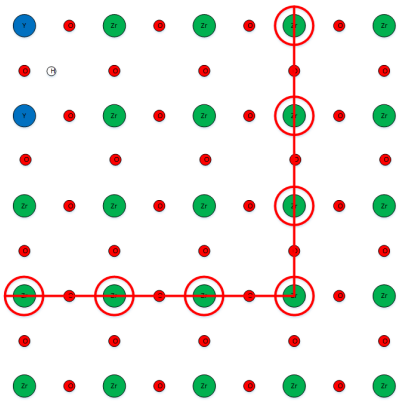

**Figure 10.4: Cut through a 4×4×4 supercell with the 1NN-1NN defect configuration.** Yttrium is shown in blue, zirconium in green, oxygen in red and the proton in white. The red marked zirconium ions are held fixed during the calculation to prevent octahedral tilting due to the periodic boundary conditions in a 3×3×3 supercell.

Figure 10.3 (right) shows the comparison between all methods. In every case, the precise calculation is used as the energy reference and the energy difference is normalized to one unit cell to establish comparability between different sized supercells.
It can be seen that the deviations between "3×3×3" and the precise calculations are in the range of one order of magnitude, which is huge. The "no tilting" approximation for the far-far configuration is as bad as the rough criterion. For 1NN-1NN, the error is also much larger, though better than for "3×3×3".
Comparing energy values calculated in a 3×3×3 supercell to those from 4×4×4 supercells again should be done with great care only.

# 11

# Conclusion

"If you tell the truth, you don't have to remember anything."
- Mark Twain, American writer.

In this work, density functional theory calculations and kinetic Monte Carlo simulations were combined to link microscopic properties of protons and oxygen vacancies and the macroscopic ionic conductivity in acceptor-doped $BaZrO_3$.
A simulation model was set up that included the pair interactions between protons, oxygen vacancies and five dopants: yttrium, gallium, indium, scandium and gadolinium. The model is expandable, more dopants are imaginable as well as the incorporation of polarons. It was especially used to investigate yttrium-doped $BaZrO_3$ since this is the most common dopant.
For yttrium-doped $BaZrO_3$ two limiting cases were investigated: The fully hydrated case, where only protons were available as mobile species and the dry case, where only oxygen vacancies were available. In the first case, it was found that the proton conductivity increases with increasing dopant fraction but the curve revealed a kink at low dopant fractions after which it increased even stronger. This was accompanied by a minimum in the proton mobility which increased with increasing dopant fraction after an initial decrease. This was traced back to the formation of (parts of) percolation pathways, in which the protons could move faster. Additionally, the perfect superstructure could be predicted to achieve a maximum in proton conductivity. Finally, activation energies could be obtained and the results were in good agreement with literature.

For oxygen ions in yttrium-doped $BaZrO_3$, the experimental finding could be confirmed that the ionic mobility is much lower than that of protons. Again, activation energies were obtained that fit well to experimental literature values. The percolation pathways were not beneficial in this case because oxygen vacancies were not able to move faster inside of them.

The knowledge gained was used to simulate proton and oxygen vacancy conductivity in gallium, indium, scandium and gadolinium-doped $BaZrO_3$. The trapping range of the first three dopants reached up to 1NN in contrast to yttrium's and gadolinium's trapping range including 1NN and 2NN. This had an influence on the building of percolation pathways that occurred at higher dopant fractions. The minimum in mobility and the even stronger increase in conductivity for dopant fractions above that of the mobility minimum was also found in various cases, in particular gallium-doped $BaZrO_3$. Here, an increase in conductivity was observed not because of protons inside of the percolation pathways but because of those who were kept outside. Additionally, it could be described how oxygen vacancies could block parts of those pathways.

Simulations were performed with protons and oxygen vacancies being mobile at the same time. To the best knowledge, this is the first time simulations like these were performed. It was found that oxygen vacancies in yttrium-doped $BaZrO_3$ had only a negligible influence on protons. The protons, on the other hand, influenced oxygen vacancies and were slowing them down by blocking their pathway.

In simulations with two mobile species and scandium or indium, the findings were similar to yttrium doping and in gadolinium-doped $BaZrO_3$ no influence of one species on another was found at all. In gallium-doped $BaZrO_3$ on the other hand, a decrease in proton mobility was found that was caused by the presence of oxygen vacancies and could not yet be explained completely.

Finally, the vehicle mechanism in $BaZrO_3$ was investigated and found to be a rare phenomenon with minimal influence on proton or oxygen vacancy conductivity due to the low probability of occurrence. Additionally, the importance of choosing the right size the of supercell was pointed out as well as choosing the parameter set for the density functional theory calculations carefully.

# References


[1] Federal Ministry for Economic Affairs and Energy, The National Hydrogen Strategy, **2020**.

[2] H. Iwahara, T. Yajima, T. Hibino, K. Ozaki, H. Suzuki, *Solid State Ionics* **1993**, *61*, 65–69.

[3] K. D. Kreuer, *Annual Review of Materials Research* **2003**, *33*, 333–359.

[4] L. Bi, E. Traversa, *Journal of Materials Research* **2014**, *29*, 1–15.

[5] K. Bae, D. Y. Jang, H. J. Choi, D. Kim, J. Hong, B.-K. Kim, J.-H. Lee, J.-W. Son, J. H. Shim, *Nature Communications* **2017**, *8*, 14553.

[6] Y. Yamazaki, F. Blanc, Y. Okuyama, L. Buannic, J. C. Lucio-Vega, C. P. Grey, S. M. Haile, *Nature materials* **2013**, *12*, 647–651.

[7] V. Tsidilkovski, A. Kuzmin, L. Putilov, V. Balakireva, *Solid State Ionics* **2017**, *301*, 170–175.

[8] K. Toyoura, W. Meng, D. Han, T. Uda, *Journal of Materials Chemistry A* **2018**, *6*, 22721–22730.

[9] G. Imai, T. Nakamura, K. Amezawa, *Solid State Ionics* **2017**, *303*, 12–15.

[10] L. Buannic, L. Sperrin, R. Dervişoğlu, F. Blanc, C. P. Grey, *Physical Chemistry Chemical Physics* **2018**, *20*, 4317–4328.

[11] M. A. Gomez, G. Kwan, W. Zhu, M. Chelliah, X. Zuo, A. Eshun, V. Blackmer, T. Huynh, M. Huynh, *Solid State Ionics* **2017**, *304*, 126–134.

[12] H. Takahashi, I. Yashima, K. Amezawa, K. Eguchi, H. Matsumoto, H. Takamura, S. Yamaguchi, *Chemistry of Materials* **2017**, *29*, 1518–1526.

[13] F. M. Draber, C. Ader, J. P. Arnold, S. Eisele, S. Grieshammer, S. Yamaguchi, M. Martin, *Nature materials* **2020**, *19*, 338–346.

[14] F. A. Kröger, H. J. Vink in *Solid state physics*, (Eds.: F. Seitz, D. Turnbull), Solid State Physics, Academic Press, New York, **1956**, pp. 307–435.

[15] J. Maier, *Physical chemistry of ionic materials: Ions and electrons in solids*, Wiley, Chichester and Hoboken NJ, **2004**.

[16] D. Ielmini, R. Waser, *Resistive switching: From fundamentals of nanionic redox processes to memristive device applications / edited by Daniele Ielmini and Rainer Waser*, Wiley-VCH, Weinheim, Germany, **2016**.

[17] A. Einstein, *Annalen der Physik* **1905**, *322*, 549–560.

[18] M. von Smoluchowski, *Annalen der Physik* **1906**, *326*, 756–780.

[19] G. E. Murch, *American Journal of Physics* **1979**, *47*, 958–960.

[20] W. Nernst, *Zeitschrift für Physikalische Chemie* **1888**, *2U*.

[21] H. D. Megaw, *Proceedings of the Physical Society* **1946**, *58*, 133.

[22] T. Ahmad, A. K. Ganguli, *Journal of the American Ceramic Society* **2006**, *89*, 3140–3146.

[23] G. Łupina, J. Dąbrowski, P. Dudek, G. Kozłowski, P. Zaumseil, G. Lippert, O. Fursenko, J. Bauer, C. Baristiran, I. Costina, H.-J. Müssig, L. Oberbeck, U. Schröder, *Applied Physics Letters* **2009**, *94*, 152903.

[24] J. Robertson, *Journal of Vacuum Science & Technology B: Microelectronics and Nanometer Structures* **2000**, *18*, 1785.

[25] S. Yamanaka, M. Fujikane, T. Hamaguchi, H. Muta, T. Oyama, T. Matsuda, S.-i. Kobayashi, K. Kurosaki, *Journal of Alloys and Compounds* **2003**, *359*, 109–113.

[26] K. D. Kreuer, St. Adams, W. Münch, A. Fuchs, U. Klock, J. Maier, *Solid State Ionics* **2001**, *145*, 295–306.

[27] R. Dronskowski, *Computational chemistry of solid state materials*, 1. repr. Aufl., Wiley-VCH, Weinheim, **2007**.

[28] D. S. Sholl, J. A. Steckel, *Density Functional Theory: A Practical Introduction*, 1st ed., Wiley, **2009**.

[29] M. Born, R. Oppenheimer, *Annalen der Physik* **1927**, *389*, 457–484.

[30] L. H. Thomas, *Mathematical Proceedings of the Cambridge Philosophical Society* **1927**, *23*, 542–548.

[31] E. Fermi, *Zeitschrift für Physik* **1928**, *48*, 73–79.

[32] P. Hohenberg, W. Kohn, *Phys. Rev.* **1964**, *136*, B864–B871.

[33] W. Kohn, L. J. Sham, *Phys. Rev.* **1965**, *140*, A1133–A1138.

[34] F. Bloch, *Zeitschrift für Physik* **1929**, *52*, 555–600.

[35] H. J. Monkhorst, J. D. Pack, *Phys. Rev. B* **1976**, *13*, 5188–5192.

[36] G. Henkelman, B. P. Uberuaga, H. Jónsson, *The Journal of chemical physics* **2000**, *113*, 9901–9904.

[37] D. Sheppard, P. Xiao, W. Chemelewski, D. D. Johnson, G. Henkelman, *The Journal of chemical physics* **2012**, *136*, 074103.

[38] J. P. Perdew, K. Burke, M. Ernzerhof, *Phys. Rev. Lett.* **1996**, *77*, 3865–3868.

[39] P. E. Blöchl, *Phys. Rev. B* **1994**, *50*, 17953–17979.

[40] G. Kresse, J. Furthmüller, *Phys. Rev. B* **1996**, *54*, 11169–11186.

[41] G. Kresse, D. Joubert, *Phys. Rev. B* **1999**, *59*, 1758–1775.

[42] F. Birch, *Physical Review* **1947**, *71*, 809–824.

[43] F. D. Murnaghan, *American Journal of Mathematics* **1937**, *59*, 235.

[44] G. Makov, M. C. Payne, *Phys. Rev. B* **1995**, *51*, 4014–4022.

[45] N. Metropolis, S. Ulam, *Journal of the American Statistical Association* **1949**, *44*, 335–341.

[46] N. Metropolis, A. W. Rosenbluth, M. N. Rosenbluth, A. H. Teller, E. Teller, *The Journal of chemical physics* **1953**, *21*, 1087–1092.

[47] G. E. Murch, *American Journal of Physics* **1979**, *47*, 78–80.

[48] G. E. Murch, *Solid State Ionics* **1982**, *6*, 295–302.

[49] B. Grope, T. Zacherle, M. Nakayama, M. Martin, *Solid State Ionics* **2012**, *225*, 476–483.

[50] Benjamin O. H. Grope, Dissertation, RWTH Aachen, Aachen, **2015**.

[51] J. P. Arnold, master thesis, RWTH Aachen, Aachen, **2018**.

[52] J. Koettgen, T. Zacherle, S. Grieshammer, M. Martin, *Phys. Chem. Chem. Phys.* **2017**, *19*, 9957–9973.

[53] P. Hein, B. O. Grope, J. Koettgen, S. Grieshammer, M. Martin, *Materials Chemistry and Physics* **2021**, *257*, 123767.

[54] S. Eisele, S. Grieshammer, *Journal of computational chemistry* **2020**, 1–15.

[55] M. Matsumoto, T. Nishimura, *ACM Trans. Model. Comput. Simul.* **1998**, *8*, 3–30.

[56] M. E. O'Neill, *ACM Trans. Math. Software* **2014**.

[57] J. J. A. Peulen, research work, RWTH Aachen, Aachen, **2020**.

[58] E. Gilardi, E. Fabbri, L. Bi, J. L. M. Rupp, T. Lippert, D. Pergolesi, E. Traversa, *The Journal of Physical Chemistry C* **2017**, *121*, 9739–9747.

[59] M. E. Björketun, P. G. Sundell, G. Wahnström, *Phys. Rev. B* **2007**, *76*, 054307.

[60] D. Han, K. Shinoda, S. Sato, M. Majima, T. Uda, *J. Mater. Chem. A* **2015**, *3*, 1243–1250.

[61] M. A. Gomez, F.-J. Liu, *Solid State Ionics* **2013**, *252*, 40–47.

[62] S. G. Kang, D. S. Sholl, *RSC Advances* **2013**, *3*, 3333.

[63] S. Imashuku, T. Uda, Y. Nose, G. Taniguchi, Y. Ito, Y. Awakura, *Journal of The Electrochemical Society* **2009**, *156*, B1–B8.

[64] D.-K. Lim, H.-N. Im, S.-Y. Jeon, J.-Y. Park, S.-J. Song, *Acta Materialia* **2013**, *61*, 1274–1283.

[65] K. H. Ryu, S. M. Haile, *Solid State Ionics* **1999**, *125*, 355–367.

[66] Y. Rao, S. Zhong, F. He, Z. Wang, R. Peng, Y. Lu, *International Journal of Hydrogen Energy* **2012**, *37*, 12522–12527.

[67] D. Han, K. Shinoda, T. Uda, *Journal of the American Ceramic Society* **2014**, *97*, 643–650.

[68] D. Han, N. Hatada, T. Uda, *Journal of The Electrochemical Society* **2016**, *163*, F470–F476.

[69] D. Kim, S. Miyoshi, T. Tsuchiya, S. Yamaguchi, *Solid State Ionics* **2014**, *262*, 875–878.

[70] D.-Y. Kim, S. Miyoshi, T. Tsuchiya, S. Yamaguchi, *Chemistry of Materials* **2014**, *26*, 927–934.

[71] P. P. Khirade, S. D. Birajdar, A. V. Humbe, K. M. Jadhav, *Journal of Electronic Materials* **2016**, *45*, 3227–3235.

[72] A. V. Kasyanova, A. O. Rudenko, N. G. Molchanova, A. I. Vylkov, J. G. Lyagaeva, D. A. Medvedev, *Mendeleev Communications* **2019**, *29*, 710–712.

[73] F. Giannici, A. Longo, K.-D. Kreuer, A. Balerna, A. Martorana, *Solid State Ionics* **2010**, *181*, 122–125.

[74] F. Iguchi, N. Sata, H. Yugami, *ECS Transactions* **2019**, *16*, 395–400.

[75] N. Ito, H. Matsumoto, Y. Kawasaki, S. Okada, T. Ishihara, *Solid State Ionics* **2008**, *179*, 324–329.

[76] M. Karlsson, I. Ahmed, A. Matic, S. G. Eriksson, *Solid State Ionics* **2010**, *181*, 126–129.

[77] M. E. Björketun, P. G. Sundell, G. Wahnström, *Faraday Discuss* **2007**, *134*, 247–65; discussion 315–29, 415–9.

[78] W. Zając, D. Rusinek, K. Zheng, J. Molenda, *Open Chemistry* **2013**, *11*, 156.

[79] V. P. Gorelov, V. B. Balakireva, Y. N. Kleshchev, V. P. Brusentsov, *Inorganic Materials* **2001**, *37*, 535–538.

[80] F. Iguchi, N. Sata, H. Yugami, *Journal of Materials Chemistry* **2010**, *20*, 6265.

[81] M. Irshad, Q. u. Ain, K. Siraj, R. Raza, A. N. Tabish, M. Rafique, R. Idrees, F. Khan, S. Majeed, M. Ahsan, *Journal of Alloys and Compounds* **2020**, *815*, 152389.

[82] T. S. Bjørheim, E. A. Kotomin, J. Maier, *Journal of Materials Chemistry A* **2015**, *3*, 7639–7648.

[83] A. Lindman, T. S. Bjørheim, G. Wahnström, *Journal of Materials Chemistry A* **2017**, *5*, 13421–13429.

[84] I. Ahmed, S. Eriksson, E. Ahlberg, C. Knee, M. Karlsson, A. Matic, D. Engberg, L. Borjesson, *Solid State Ionics* **2006**, *177*, 2357–2362.

[85] I. Ahmed, C. S. Knee, M. Karlsson, S. G. Eriksson, P. F. Henry, A. Matic, D. Engberg, L. Börjesson, *Journal of Alloys and Compounds* **2008**, *450*, 103–110.

[86] M. E. Björketun, P. G. Sundell, G. Wahnström, D. Engberg, *Solid State Ionics* **2005**, *176*, 3035–3040.

[87] T. Shimura, *Solid State Ionics* **2002**, *149*, 237–246.

[88] I. Oikawa, H. Takamura, *Chemistry of Materials* **2015**, *27*, 6660–6667.

[89] J. A. Dawson, I. Tanaka, *Journal of Materials Chemistry A* **2015**, *3*, 10045–10051.

[90] I. Ahmed, S. Eriksson, E. Ahlberg, C. Knee, H. Gotlind, L. Johansson, M. Karlsson, A. Matic, L. Borjesson, *Solid State Ionics* **2007**, *178*, 515–520.

[91] R. C. T. Slade, S. D. Flint, N. Singh, *Solid State Ionics* **1995**, *82*, 135–141.

[92] M. Shirpour, R. Merkle, C. T. Lin, J. Maier, *Phys. Chem. Chem. Phys.* **2012**, *14*, 730–740.

[93] N. Kitamura, J. Akola, S. Kohara, K. Fujimoto, Y. Idemoto, *The Journal of Physical Chemistry C* **2014**, *118*, 18846–18852.

[94] K. Kato, D. Han, T. Uda, *Journal of the American Ceramic Society* **2019**, *102*, 1201–1210.

[95] O. Kosasang, K. Somroop, P. Chindaudom, R. Pornprasertsuk, *ECS Transactions* **2009**, *19*, 145–151.

[96] D. Han, N. Hatada, T. Uda, *Journal of the American Ceramic Society* **2016**, *99*, 3745–3753.

[97] A. Lindman, P. Erhart, G. Wahnström, *Physical Review B* **2016**, *94*, 075204.

[98] S. Grieshammer, B. O. H. Grope, J. Koettgen, M. Martin, *Physical Chemistry Chemical Physics* **2014**, *16*, 9974–9986.

[99] S. J. Stokes, M. S. Islam, *Journal of Materials Chemistry* **2010**, *20*, 6258–6264.

[100] R. D. Shannon, *Acta Crystallographica Section A* **1976**, *32*, 751–767.

[101] F. J. Loureiro, N. Nasani, G. S. Reddy, N. R. Munirathnam, D. P. Fagg, *Journal of Power Sources* **2019**, *438*, 226991.

[102] R. Pornprasertsuk, O. Kosasang, K. Somroop, S. Jinawath, F. B. Prinz, *ECS Transactions* **2010**, *25*, 367–381.

[103] K. D. Kreuer, *Solid State Ionics* **1999**, *125*, 285–302.

[104] S. Tao, J. T. Irvine, *Journal of Solid State Chemistry* **2007**, *180*, 3493–3503.

[105] R. B. Cervera, Y. Oyama, S. Miyoshi, K. Kobayashi, T. Yagi, S. Yamaguchi, *Solid State Ionics* **2008**, *179*, 236–242.

[106] M. A. Gomez, M. Chunduru, L. Chigweshe, L. Foster, S. J. Fensin, K. M. Fletcher, L. E. Fernandez, *The Journal of chemical physics* **2010**, *132*.

[107] S. Kang, P. Heo, Y. H. Lee, J. Ha, I. Chang, S.-W. Cha, *Electrochemistry Communications* **2011**, *13*, 374–377.

[108] I. Ahmed, F. G. Kinyanjui, P. Steegstra, Z. J. Shen, S.-G. Eriksson, M. Nygren, *Electrochemical and Solid State Letters* **2010**, *13*, B130.

[109] I. Ahmed, S. Eriksson, E. Ahlberg, C. Knee, P. Berastegui, L. Johansson, H. RUNDLOF, M. Karlsson, A. Matic, L. Borjesson, *Solid State Ionics* **2006**, *177*, 1395–1403.

[110] H. G. Bohn, T. Schober, *Journal of the American Ceramic Society* **2000**, *83*, 768–772.

[111] van Duin, Adri C. T., B. V. Merinov, S. S. Han, C. O. Dorso, W. A. Goddard, *The Journal of Physical Chemistry A* **2008**, *112*, 11414–11422.

[112] J. J. A. Peulen, Bachelor Thesis, RWTH Aachen, Aachen, **2018**.

[113] K.-D. Kreuer, W. Weppner, A. Rabenau, *Solid State Ionics* **1981**, *3/4*, 353–358.

[114] K.-D. Kreuer, A. Rabenau, W. Weppner, *Angewandte Chemie* **1982**, *94*, 224–225.

[115] J. Bu, P. G. Jönsson, Z. Zhao, *Journal of Power Sources* **2014**, *272*, 786–793.

[116] P. Colomban, *Solid State Ionics* **2019**, *334*, 125–144.

[117] P. Knauth, M. L. Di Vona, *Solid state proton conductors: Properties and applications in fuel cells*, John Wiley & Sons, Chichester, West Sussex, U.K and Hoboken, **2012**.

[118] K.-D. Kreuer, *Chemistry of Materials* **1996**, *8*, 610–641.

[119] L. Li, J. C. Nino, *International Journal of Hydrogen Energy* **2013**, *38*, 1598–1606.

[120] J.-P. Melchior, K.-D. Kreuer, J. Maier, *Physical chemistry chemical physics : PCCP* **2016**, *19*, 587–600.

[121] T. Norby, *Solid State Ionics* **1990**, *40/41*, 857–862.

[122] R. Sato, S. Ohkuma, Y. Shibuta, F. Shimojo, S. Yamaguchi, *The Journal of Physical Chemistry C* **2015**, *119*, 28925–28933.

[123] S. Uchida, R. Hosono, R. Eguchi, R. Kawahara, R. Osuga, J. N. Kondo, M. Hibino, N. Mizuno, *Physical chemistry chemical physics : PCCP* **2017**, *19*, 29077–29083.

[124] H. Wang, X. Wang, B. Meng, X. Tan, K. S. Loh, J. Sunarso, S. Liu, *Journal of Industrial and Engineering Chemistry* **2018**, *60*, 297–306.

[125] I. K. Sommerfeld, research work, RWTH Aachen, Aachen, **2018**.

[126] A. H. H. Ramadan, Master thesis, RWTH Aachen, Aachen, **2012**.

[127] J. Balachandran, L. Lin, J. S. Anchell, C. A. Bridges, P. Ganesh, *The Journal of Physical Chemistry C* **2017**, *121*, 26637–26647.

[128] D.-H. Kim, B.-K. Kim, Y.-C. Kim, *Japanese Journal of Applied Physics* **2012**, *51*, 09MA01.

[129] D.-H. Kim, B.-K. Kim, Y.-C. Kim, *Journal of Electroceramics* **2013**, *30*, 19–23.

[130] J.-S. Kim, J.-H. Yang, B.-K. Kim, Y.-C. Kim, *Solid State Ionics* **2015**, *275*, 19–22.

[131] A. B. Muñoz-García, M. Tuccillo, M. Pavone, *Journal of Materials Chemistry A* **2017**, *5*, 11825–11833.

[132] J.-H. Yang, D.-H. Kim, B.-K. Kim, Y.-C. Kim, *Solid State Ionics* **2013**, *252*, 126–131.

[133] T. S. Bjørheim, M. Arrigoni, D. Gryaznov, E. Kotomin, J. Maier, *Physical Chemistry Chemical Physics* **2015**, *17*, 20765–20774.

[134] T. S. Bjørheim, M. Arrigoni, S. W. Saeed, E. Kotomin, J. Maier, *Chemistry of Materials* **2016**, *28*, 1363–1368.

[135] T. S. Bjørheim, A. Løken, R. Haugsrud, *Journal of Materials Chemistry A* **2016**, *4*, 5917–5924.

[136] R. A. Evarestov, *Physical Review B* **2011**, *83*, 014105.

[137] M. F. Hoedl, E. Makagon, I. Lubomirsky, R. Merkle, E. A. Kotomin, J. Maier, *Acta Materialia* **2018**, *160*, 247–256.

[138] E. Jedvik, A. Lindman, M. Þ. Benediktsson, G. Wahnström, *Solid State Ionics* **2015**, *275*, 2–8.

[139] J.-S. Kim, Y.-C. Kim, *Journal of the Korean Physical Society* **2017**, *70*, 75–80.

[140] A. Løken, S. W. Saeed, M. N. Getz, X. Liu, T. S. Bjørheim, *Journal of Materials Chemistry A* **2016**, *4*, 9229–9235.

[141] J. M. Polfus, T. S. Bjørheim, T. Norby, R. Bredesen, *Journal of Materials Chemistry A* **2016**, *4*, 7437–7444.

[142] N. Raja, D. Murali, S. V. M. Satyanarayana, M. Posselt, *RSC Advances* **2019**, *9*, 34158–34165.

[143] N. Raja, D. Murali, M. Posselt, S. V. M. Satyanarayana, *physica status solidi (b)* **2018**, *255*, 1700398.

[144] H. Takahashi, I. Oikawa, H. Takamura, *The Journal of Physical Chemistry C* **2018**, *122*, 6501–6507.

[145] Z. Wang, W. Yang, Z. Zhu, R. Peng, X. Wu, C. Xia, Y. Lu, *Journal of Materials Chemistry A* **2014**, *2*, 16707–16714.

[146] M. A. Gomez, F.-J. Liu, *Solid State Ionics* **2013**, *252*, 40–47.

[147] J.-S. Kim, Y.-C. Kim, *Journal of the Korean Ceramic Society* **2016**, *53*, 301–305.

# List of Figures

# List of Tables

# Figures

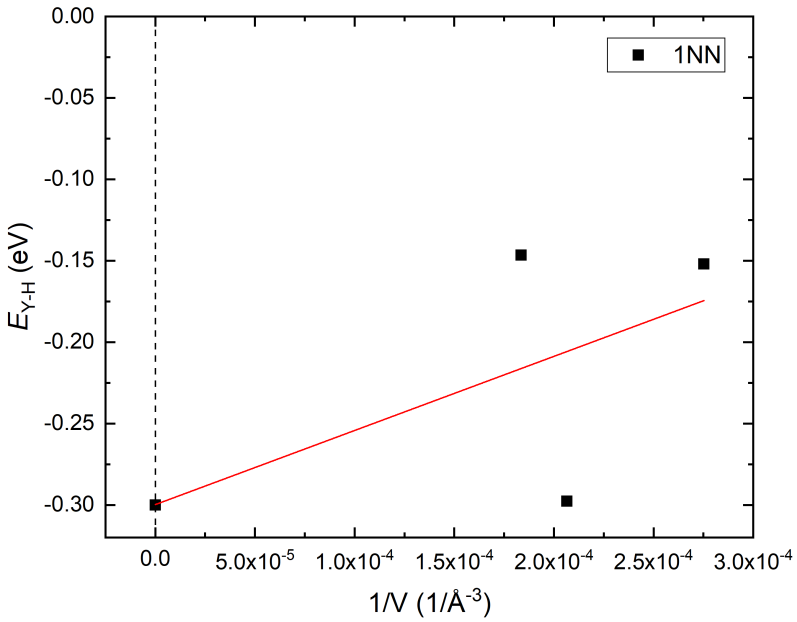


**Figure A.1: Finite size correction of the interaction energies of one yttrium ion with one proton in 1NN.** At least 3 different super cells were used for the calculations and extrapolated to $1/V = 0$.

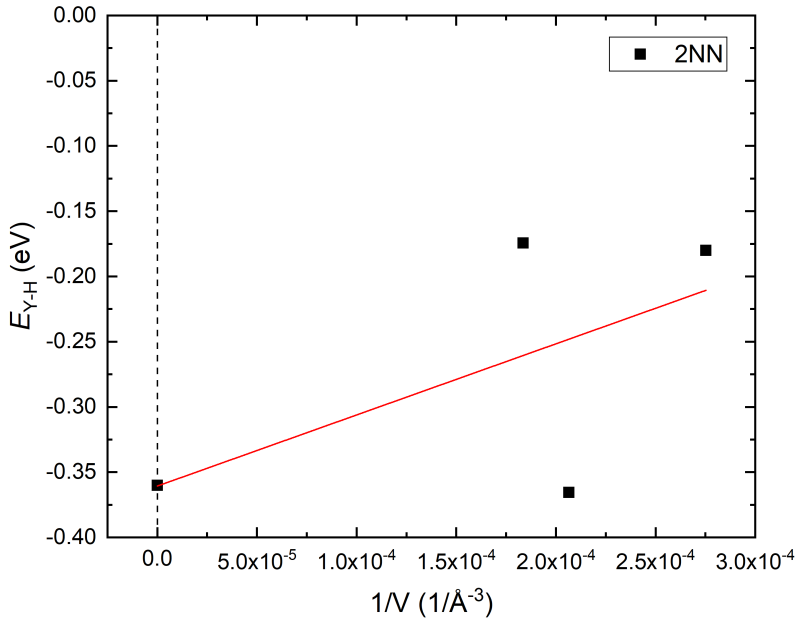


**Figure A.2: Finite size correction of the interaction energies of one yttrium ion with one proton in 2NN.** At least 3 different super cells were used for the calculations and extrapolated to $1/V = 0$.

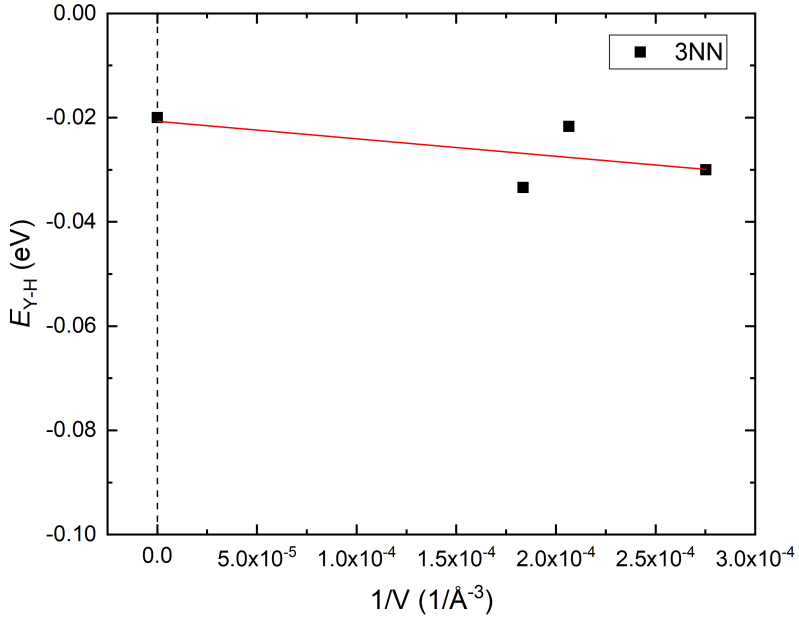


**Figure A.3: Finite size correction of the interaction energies of one yttrium ion with one proton in 3NN.** At least 3 different super cells were used for the calculations and extrapolated to $1/V = 0$.

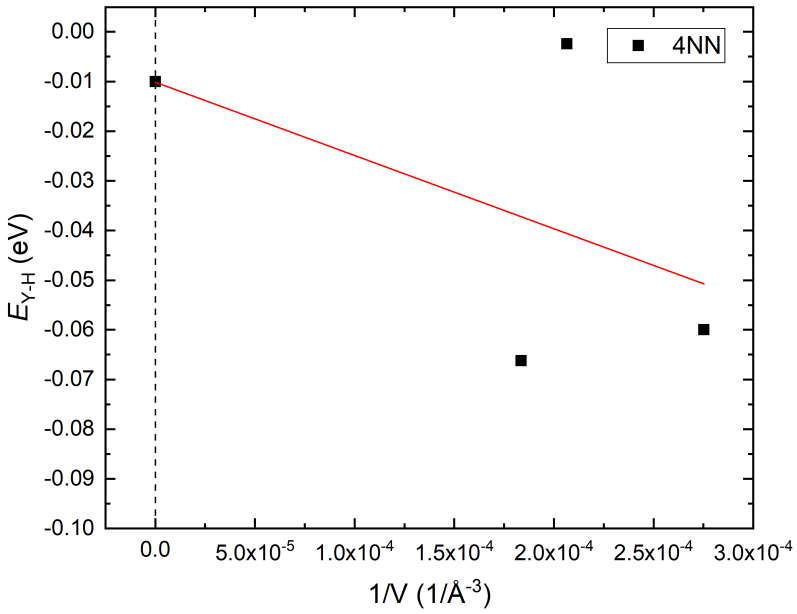


**Figure A.4: Finite size correction of the interaction energies of one yttrium ion with one proton in 4NN.** At least 3 different super cells were used for the calculations and extrapolated to $1/V = 0$.

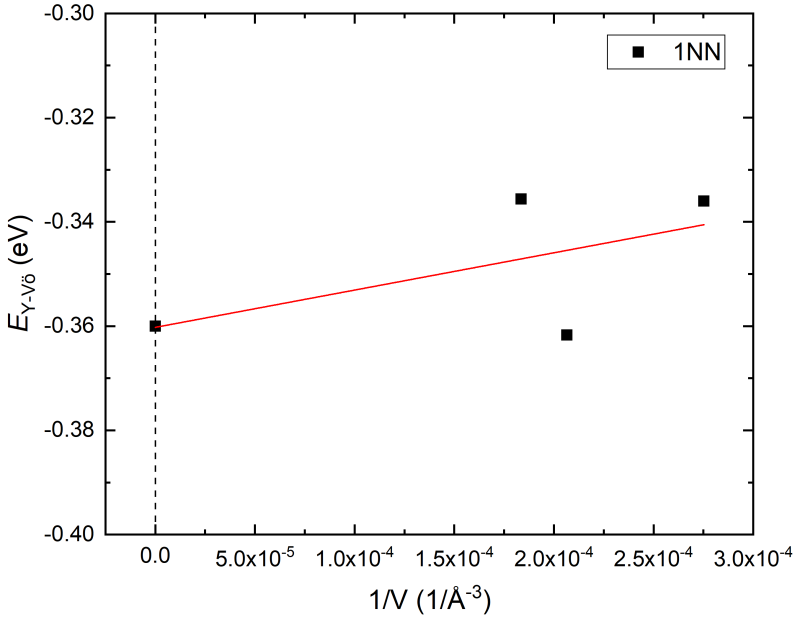


**Figure A.5: Finite size correction of the interaction energies of one yttrium ion with one oxygen vacancy in 1NN.** At least 3 different super cells were used for the calculations and extrapolated to $1/V = 0$.

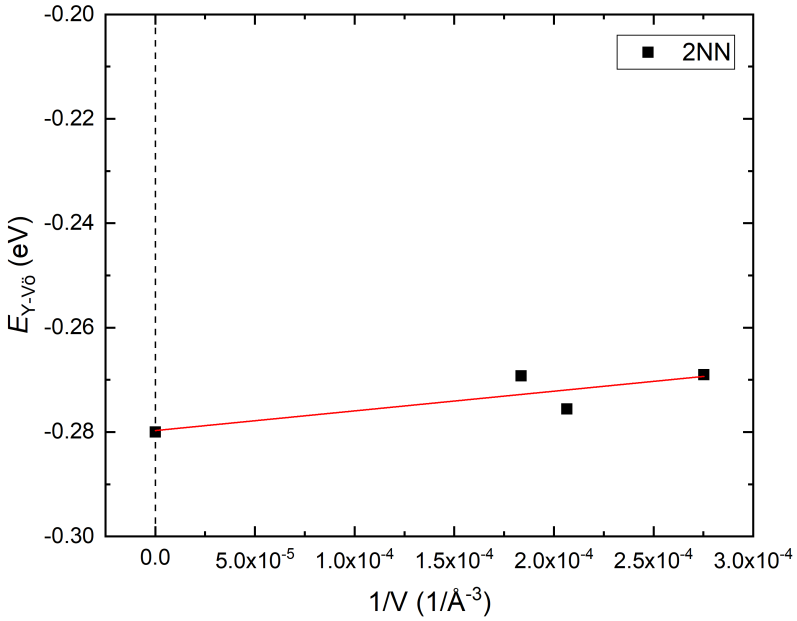


**Figure A.6: Finite size correction of the interaction energies of one yttrium ion with one oxygen vacancy in 2NN.** At least 3 different super cells were used for the calculations and extrapolated to $1/V = 0$.

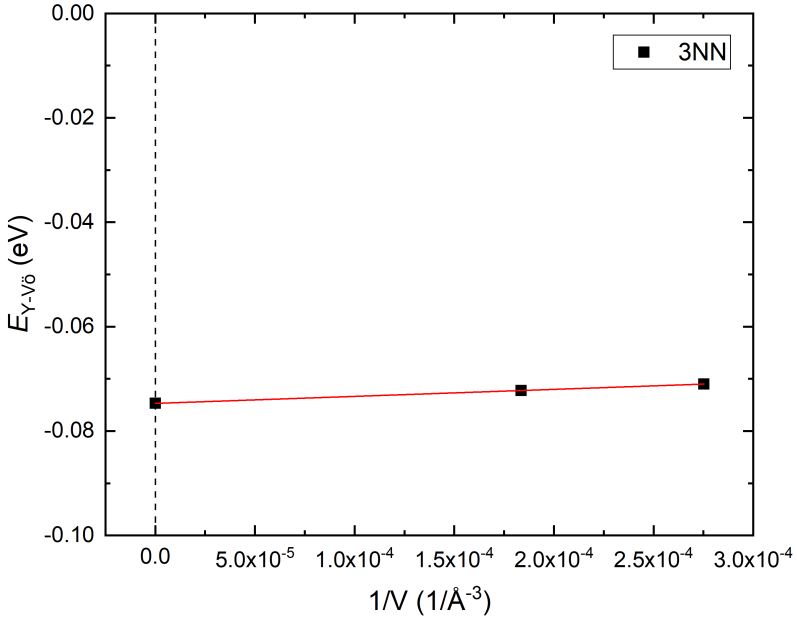


**Figure A.7: Finite size correction of the interaction energies of one yttrium ion with one oxygen vacancy in 3NN.** At least 3 different super cells were used for the calculations and extrapolated to $1/V = 0$.

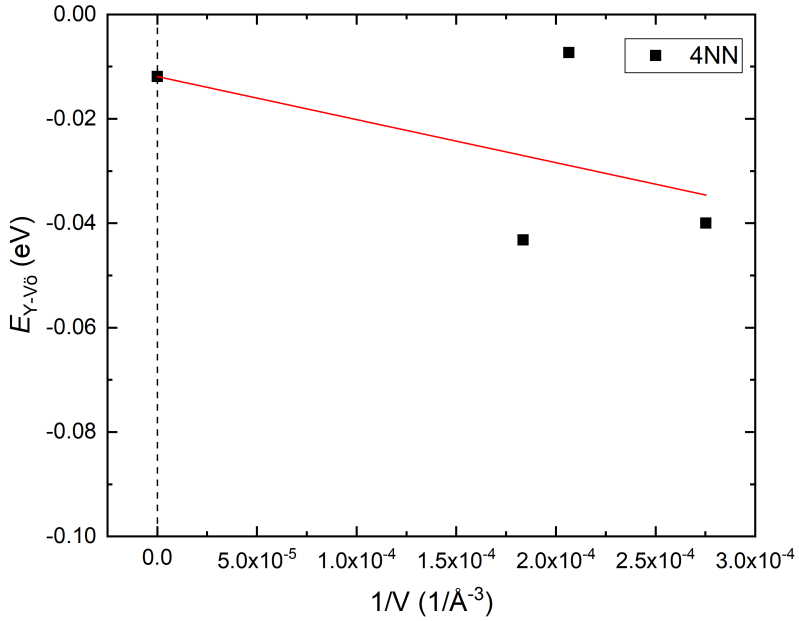


**Figure A.8: Finite size correction of the interaction energies of one yttrium ion with one oxygen vacancy in 4NN.** At least 3 different super cells were used for the calculations and extrapolated to $1/V = 0$.

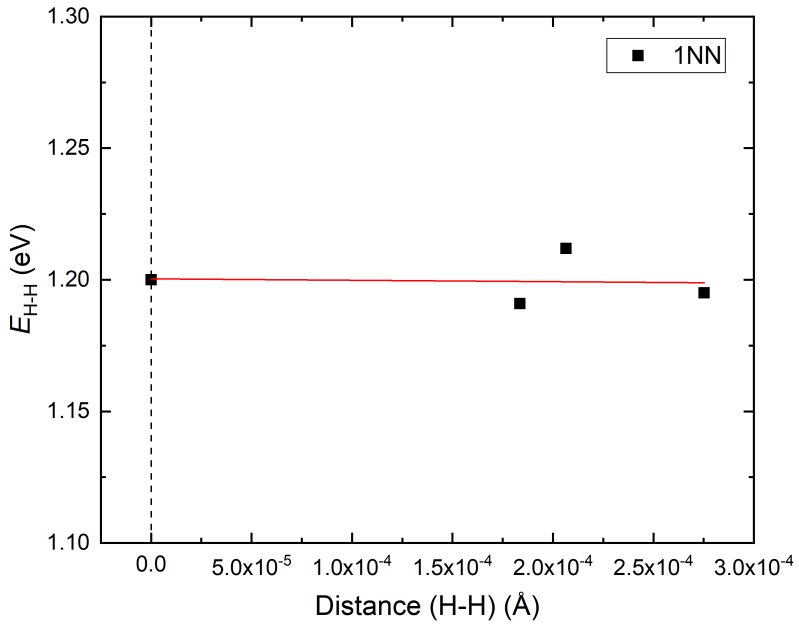


**Figure A.9: Finite size correction of the interaction energies of two protons with each other in 1NN.** At least 3 different super cells were used for the calculations and extrapolated to $1/V = 0$.

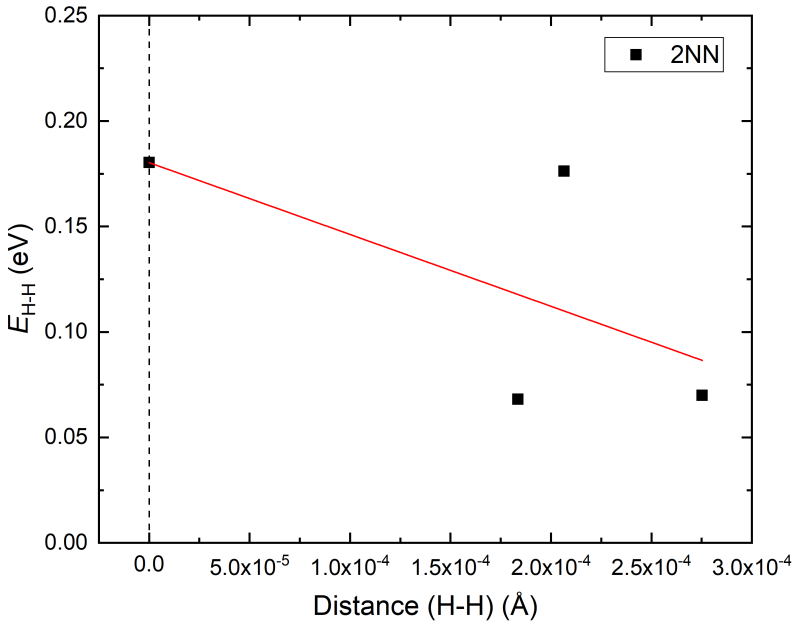


**Figure A.10: Finite size correction of the interaction energies of two protons with each other in 2NN.** At least 3 different super cells were used for the calculations and extrapolated to $1/V = 0$.

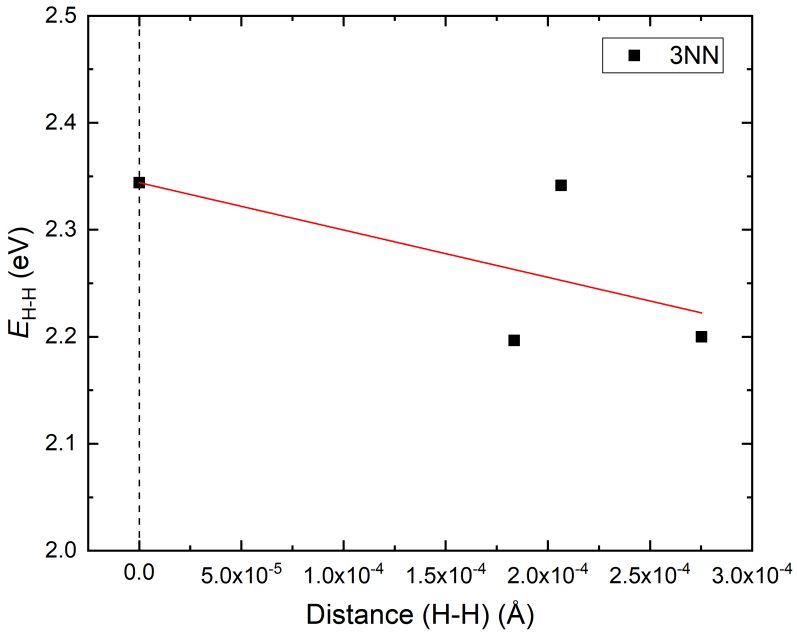


**Figure A.11: Finite size correction of the interaction energies of two protons with each other in 3NN.** At least 3 different super cells were used for the calculations and extrapolated to $1/V = 0$.

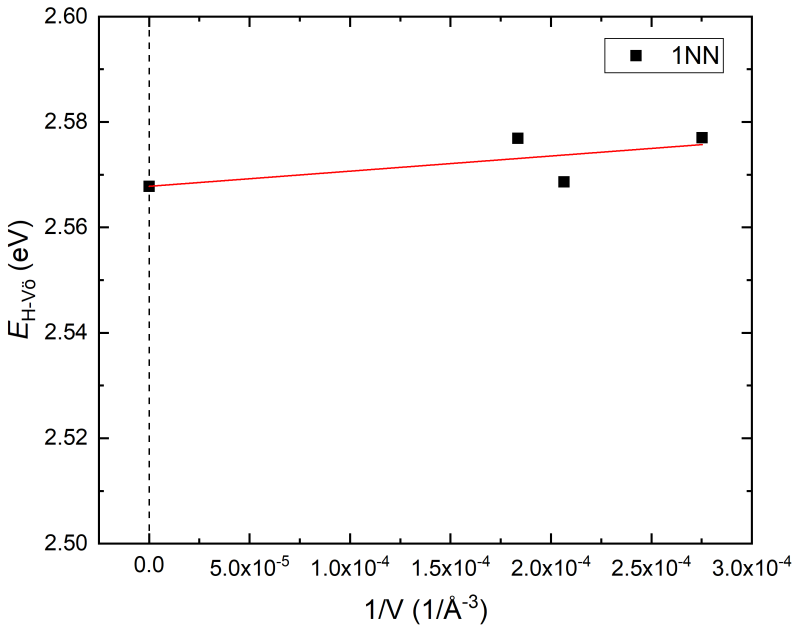


**Figure A.12: Finite size correction of the interaction energies of one proton proton with one oxygen vacancy in 1NN.** At least 3 different super cells were used for the calculations and extrapolated to $1/V = 0$.

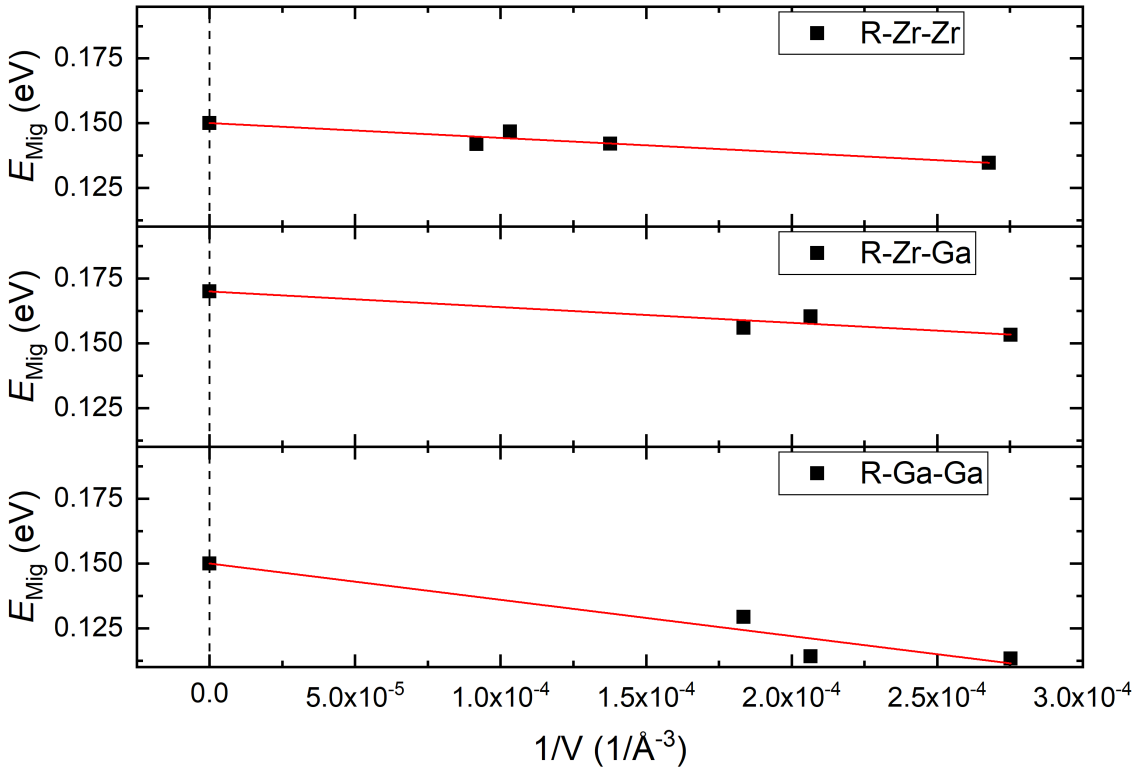


**Figure A.13: Finite size correction of the migration energies of the proton reorientation jumps in gallium-doped $BaZrO_3$.** Shown on top is the R-Zr-Zr jump, in the middle the R-Zr-Ga jump and on the bottom the R-Ga-Ga jump. At least 3 different super cells were used for the calculations and extrapolated to $1/V = 0$.

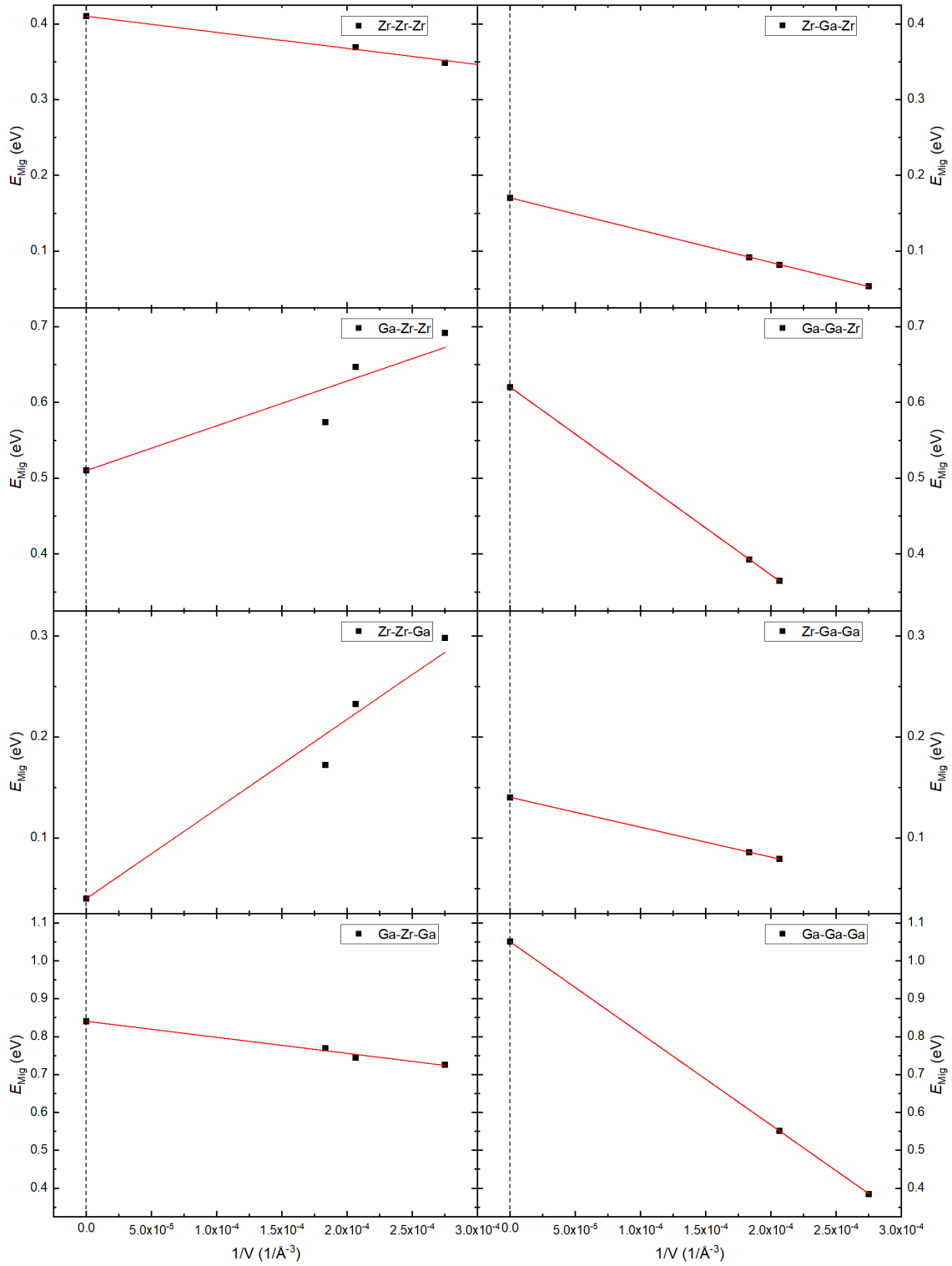


**Figure A.14: Finite size correction of the migration energies of the proton translation jumps in gallium-doped $BaZrO_3$.** The nomenclature is explained in chapter 5. At least 2 different super cells were used for the calculations and extrapolated to $1/V = 0$.

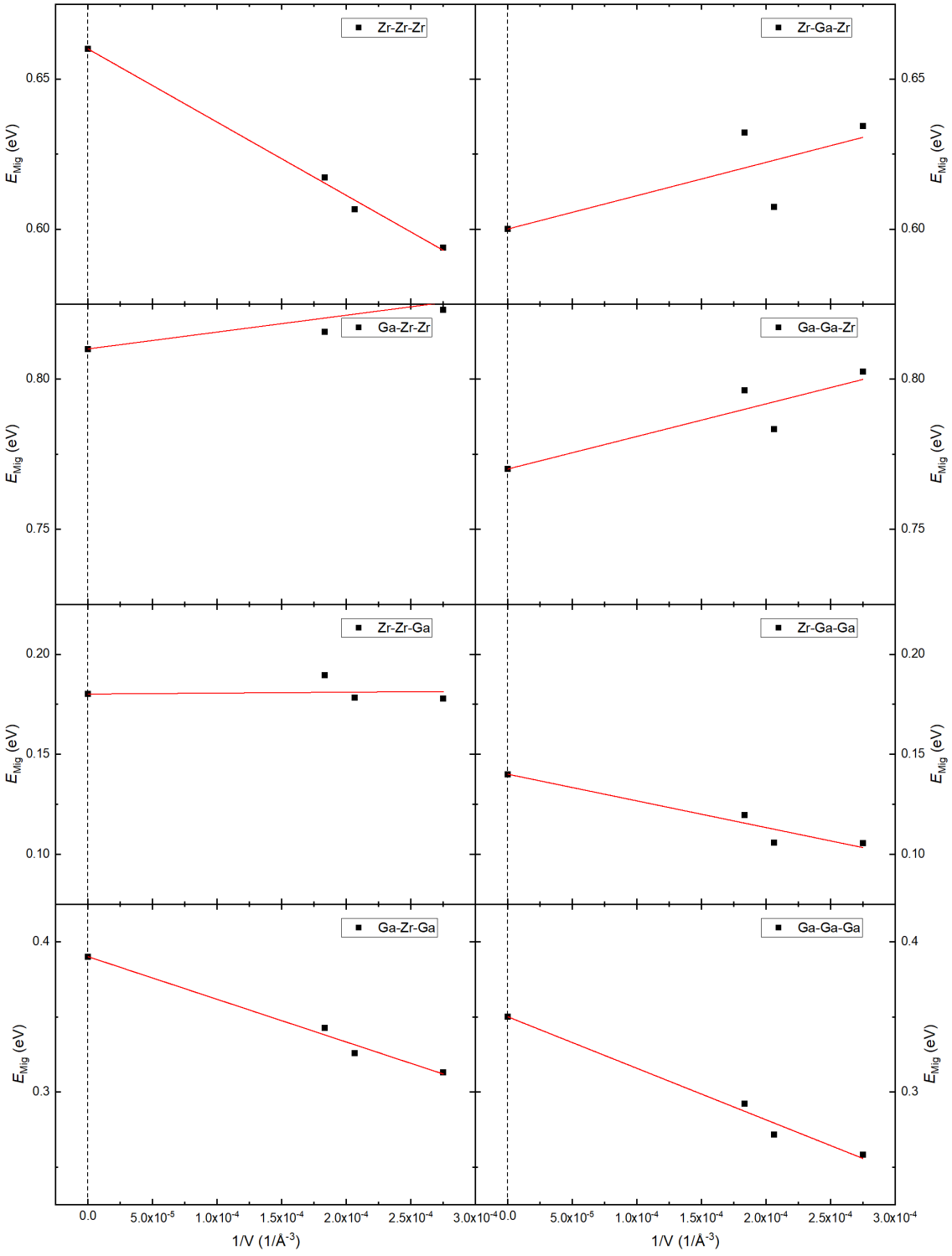


**Figure A.15: Finite size correction of the migration energies of the oxygen vacancy translation jumps in gallium-doped $BaZrO_3$.** The nomenclature is explained in chapter 5. At least 3 different super cells were used for the calculations and extrapolated to $1/V = 0$.

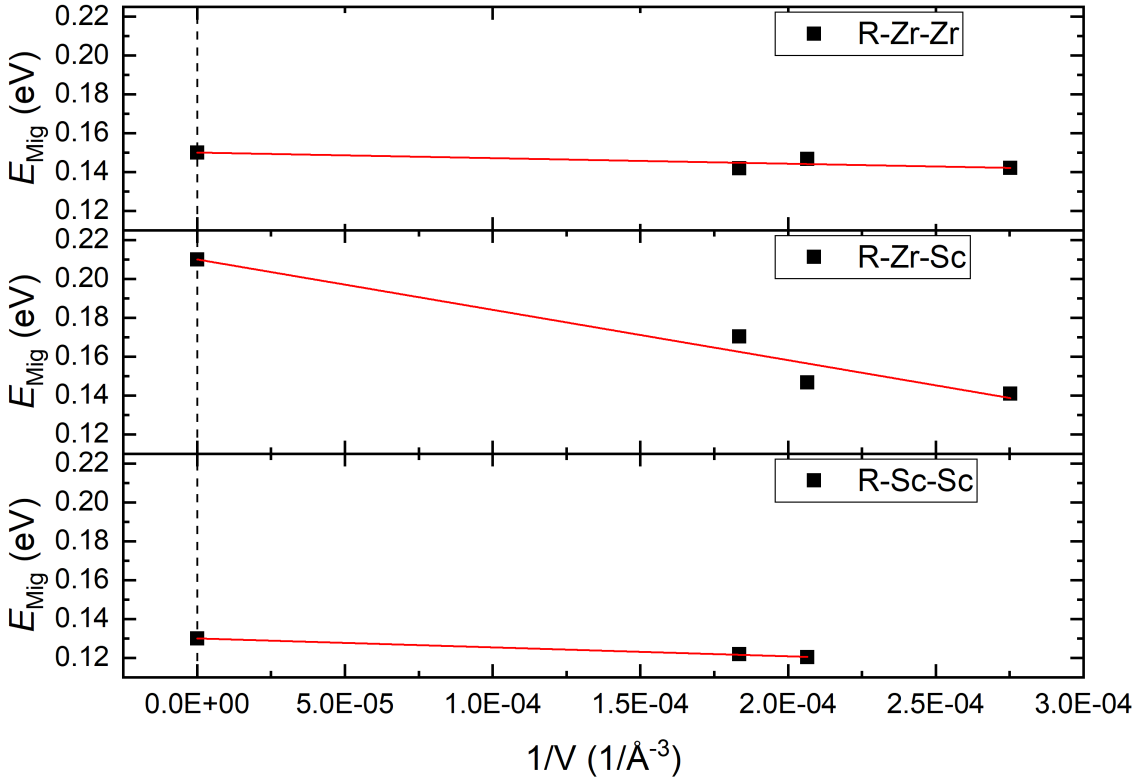


**Figure A.16: Finite size correction of the migration energies of the proton reorientation jumps in scandium-doped $BaZrO_3$.** Shown on top is the R-Zr-Zr jump, in the middle the R-Zr-Sc jump and on the bottom the R-Sc-Sc jump. At least 2 different super cells were used for the calculations and extrapolated to $1/V = 0$.

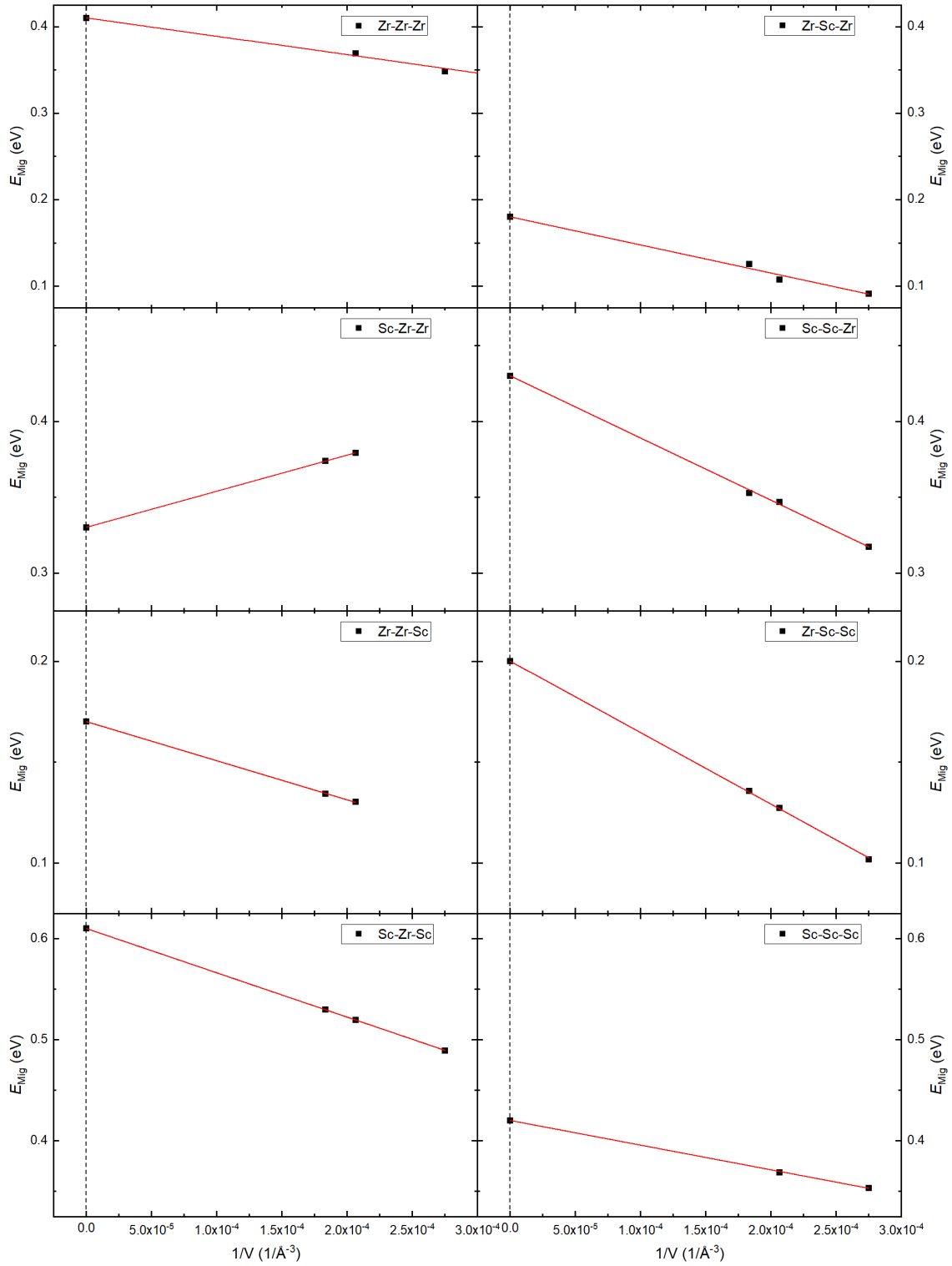


**Figure A.17: Finite size correction of the migration energies of the proton translation jumps in scandium-doped $BaZrO_3$.** The nomenclature is explained in chapter 5. At least 2 different super cells were used for the calculations and extrapolated to $1/V = 0$.

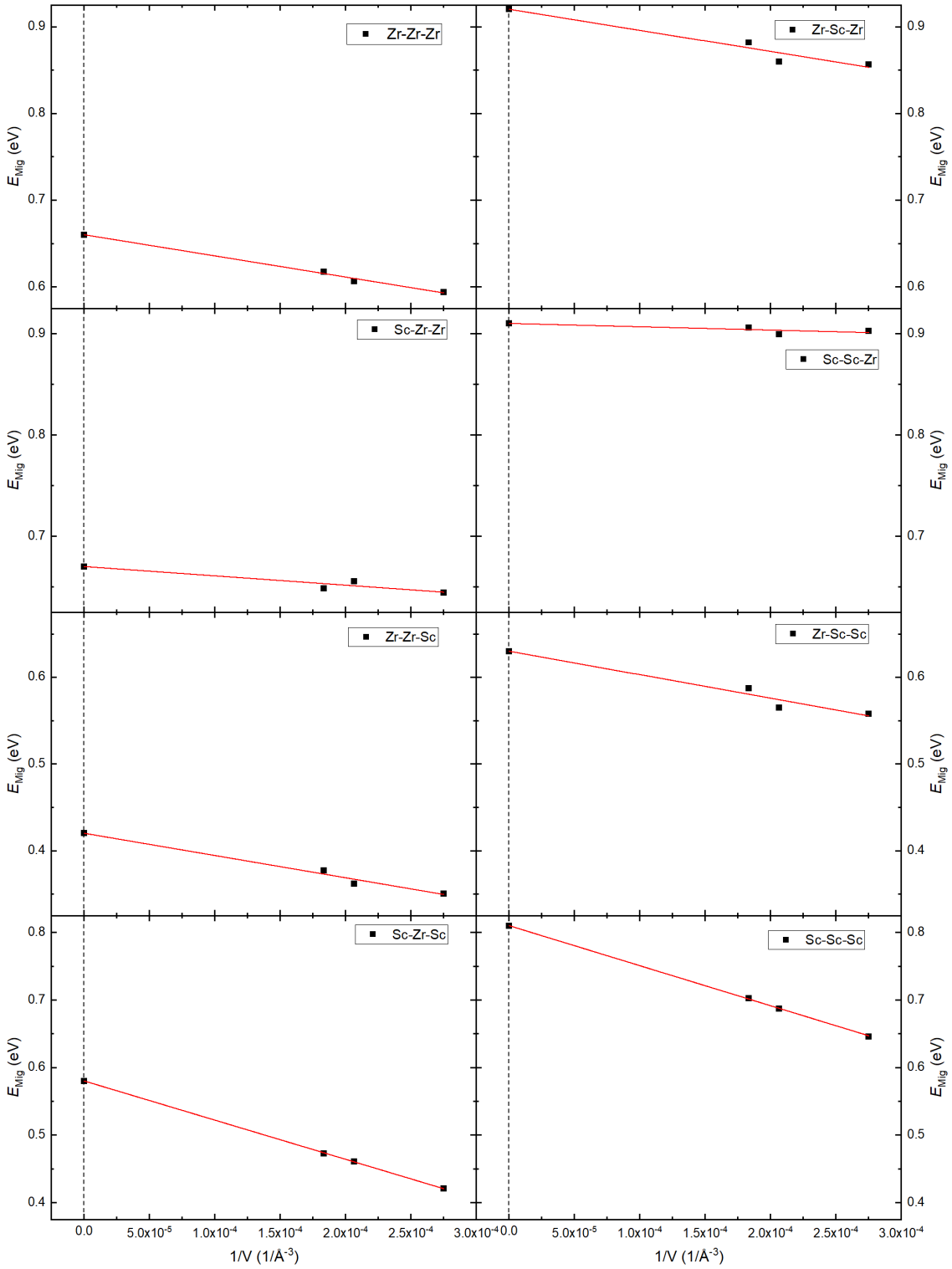


**Figure A.18: Finite size correction of the migration energies of the oxygen vacancy translation jumps in scandium-doped $BaZrO_3$.** The nomenclature is explained in chapter 5. At least 3 different super cells were used for the calculations and extrapolated to $1/V = 0$.

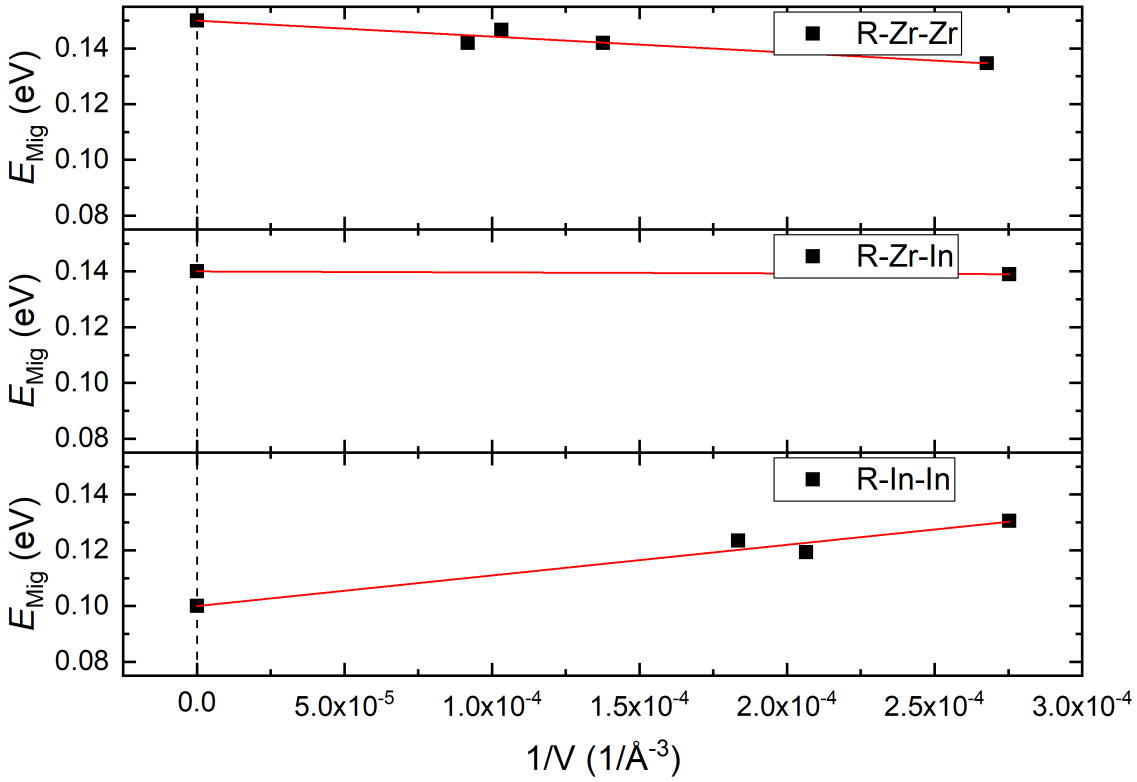


**Figure A.19: Finite size correction of the migration energies of the proton reorientation jumps in indium-doped $BaZrO_3$.** Shown on top is the R-Zr-Zr jump, in the middle the R-Zr-In jump and on the bottom the R-In-In jump. At least 3 different super cells were used for the calculations and extrapolated to $1/V = 0$.

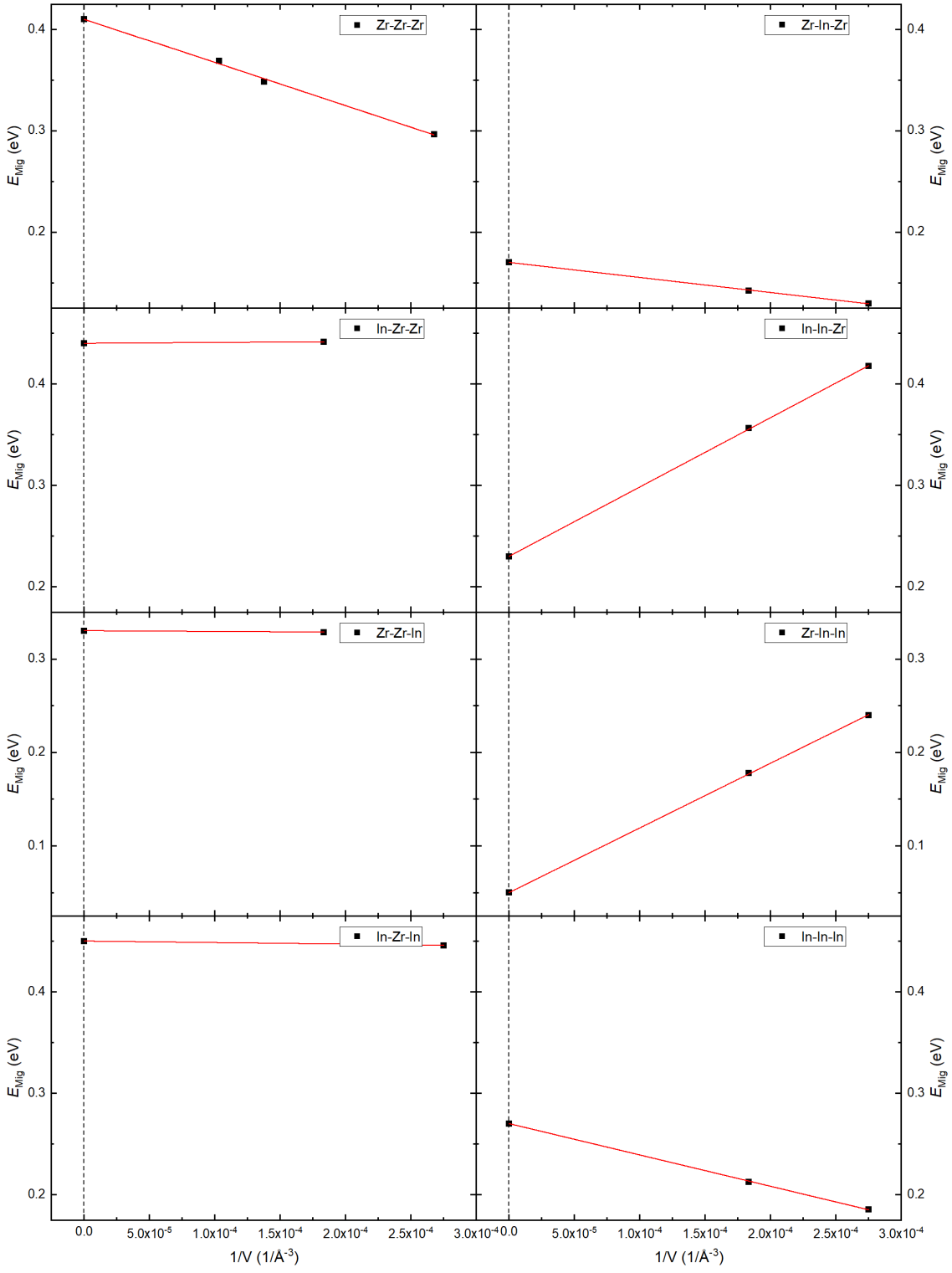


**Figure A.20: Finite size correction of the migration energies of the proton translation jumps in indium-doped $BaZrO_3$.** The nomenclature is explained in chapter 5. At least 2 different super cells were used for the calculations and extrapolated to $1/V = 0$. Only for the In-Zr-Zr and Zr-Zr-In no finite size correction was possible because the calculation in only one super cell converged.

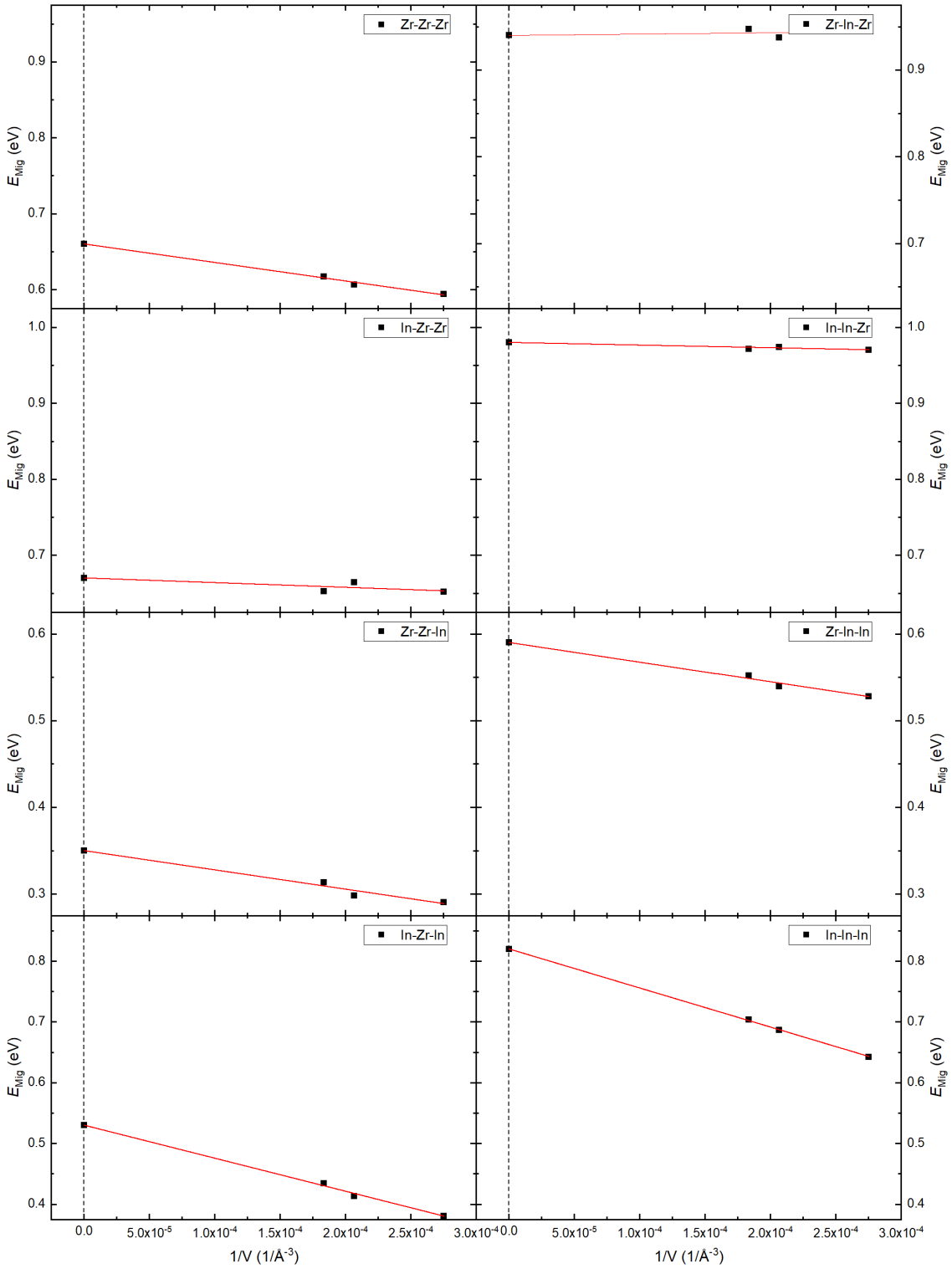


**Figure A.21: Finite size correction of the migration energies of the oxygen vacancy translation jumps in indium-doped $BaZrO_3$.** The nomenclature is explained in chapter 5. At least 3 different super cells were used for the calculations and extrapolated to $1/V = 0$.

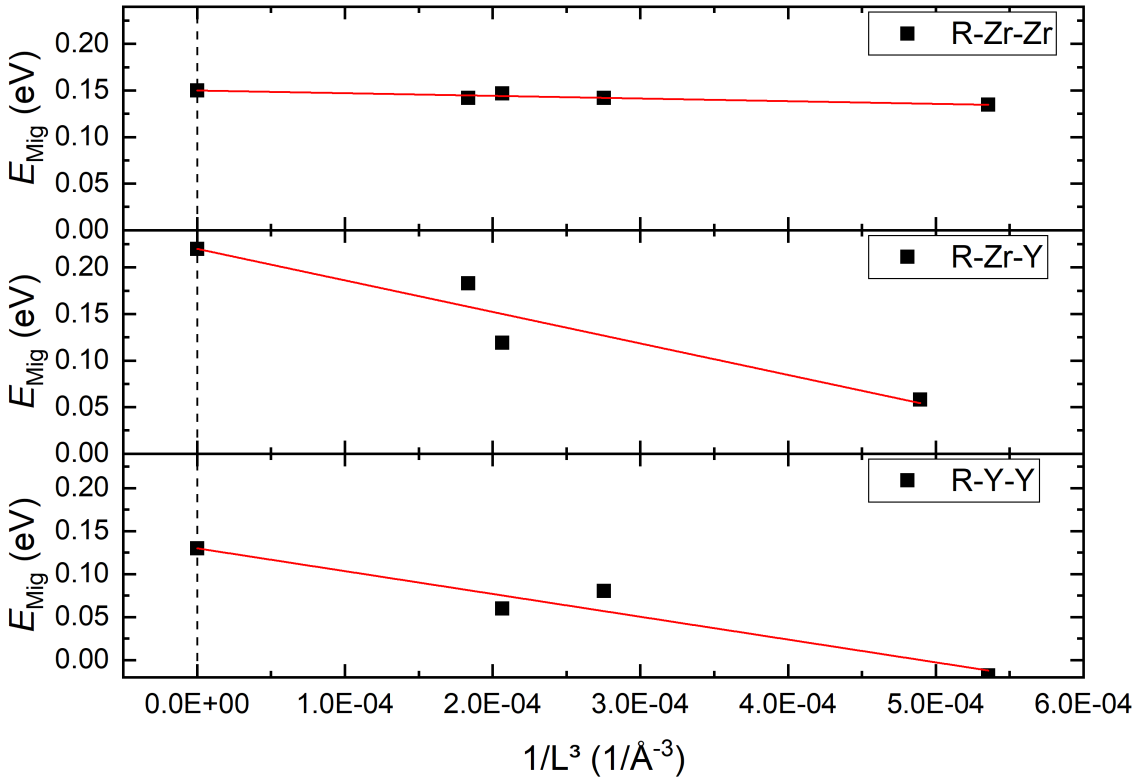


**Figure A.22: Finite size correction of the migration energies of the proton reorientation jumps in yttrium-doped $BaZrO_3$.** Shown on top is the R-Zr-Zr jump, in the middle the R-Zr-Y jump and on the bottom the R-Y-Y jump. At least 3 different super cells were used for the calculations and extrapolated to $1/V = 0$.

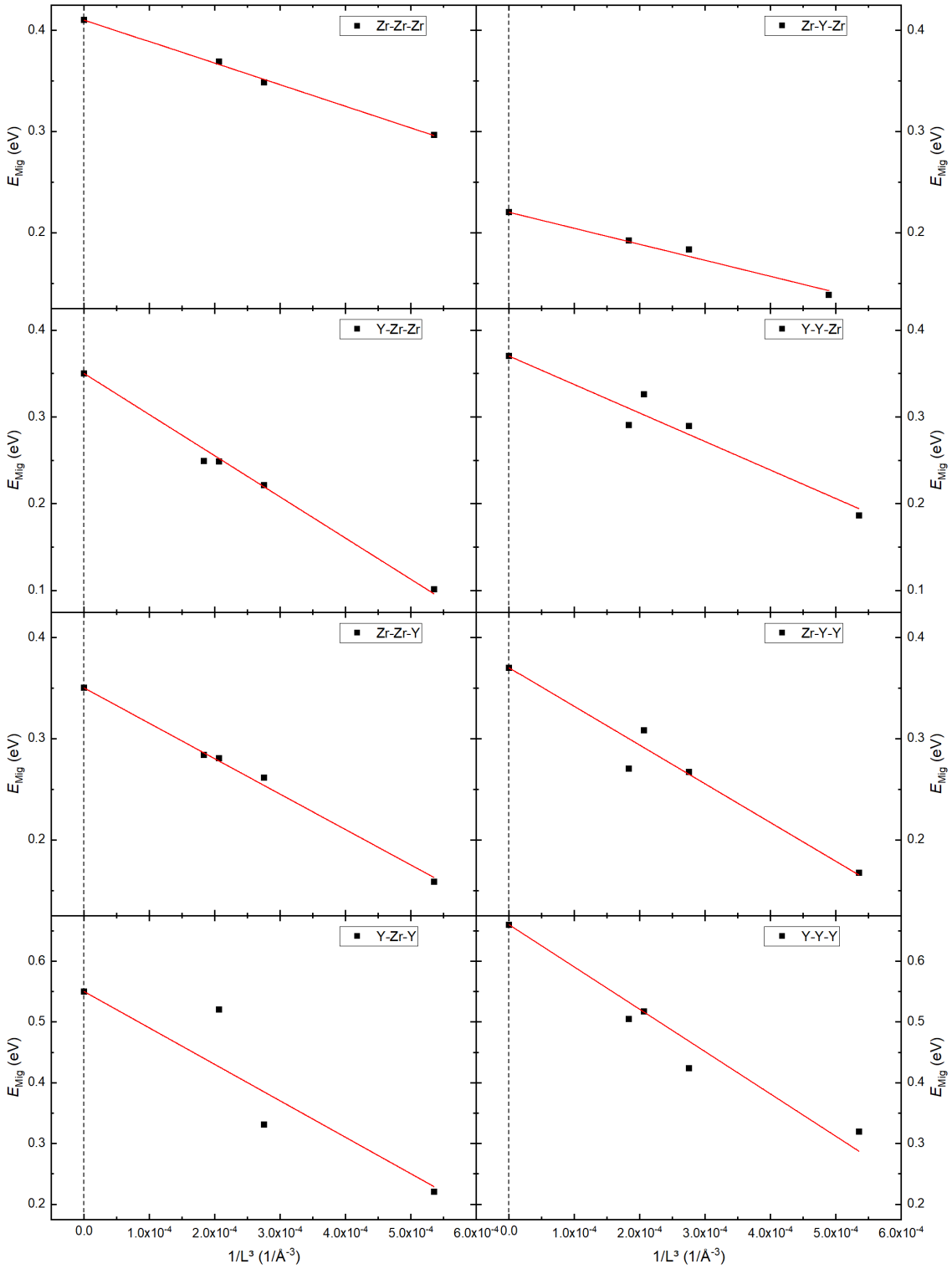


**Figure A.23: Finite size correction of the migration energies of the proton translation jumps in yttrium-doped $BaZrO_3$.** The nomenclature is explained in chapter 5. At least 3 different super cells were used for the calculations and extrapolated to $1/V = 0$.

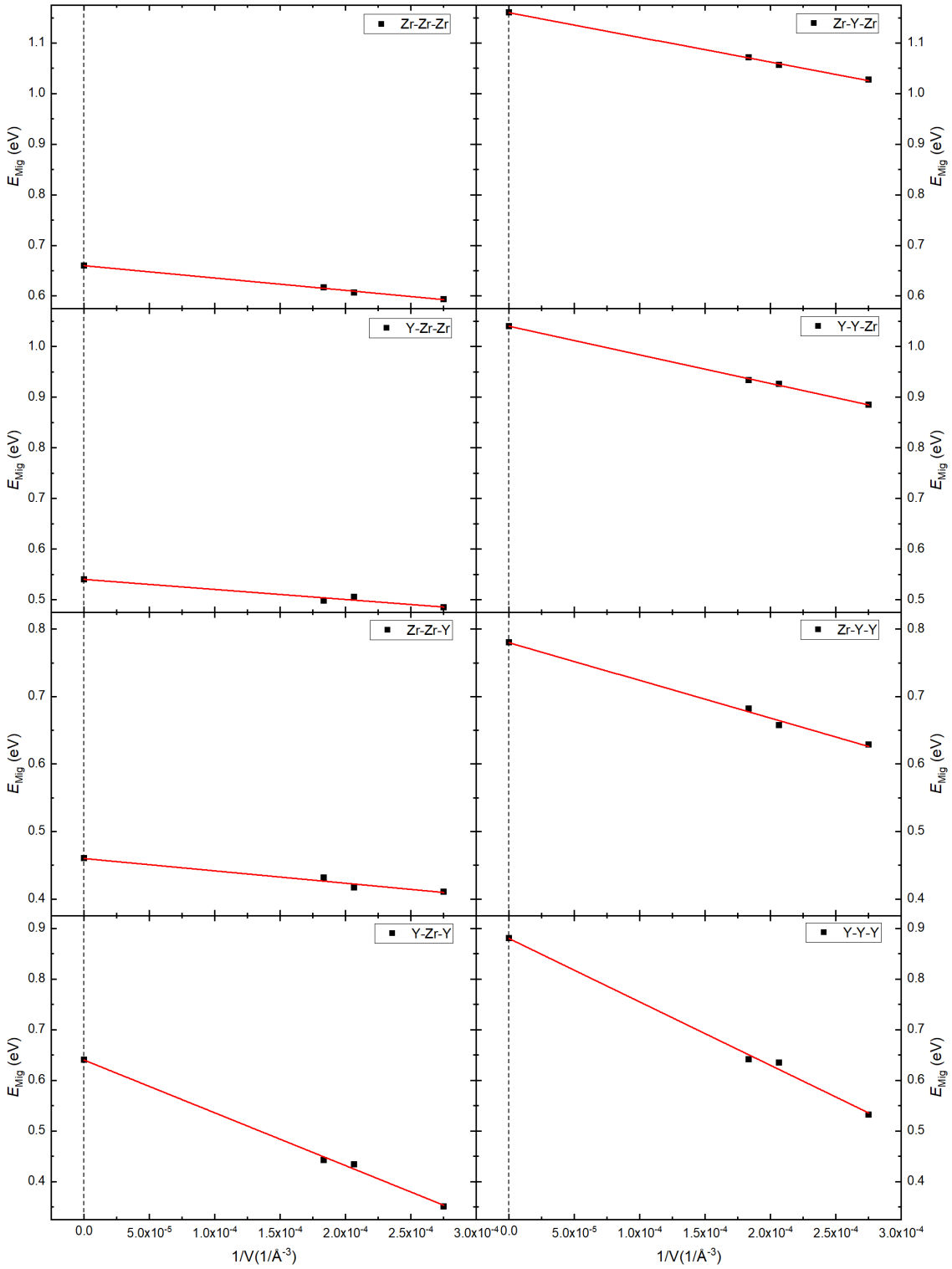


**Figure A.24: Finite size correction of the migration energies of the oxygen vacancy translation jumps in yttrium-doped $BaZrO_3$.** The nomenclature is explained in chapter 5. At least 3 different super cells were used for the calculations and extrapolated to $1/V = 0$.

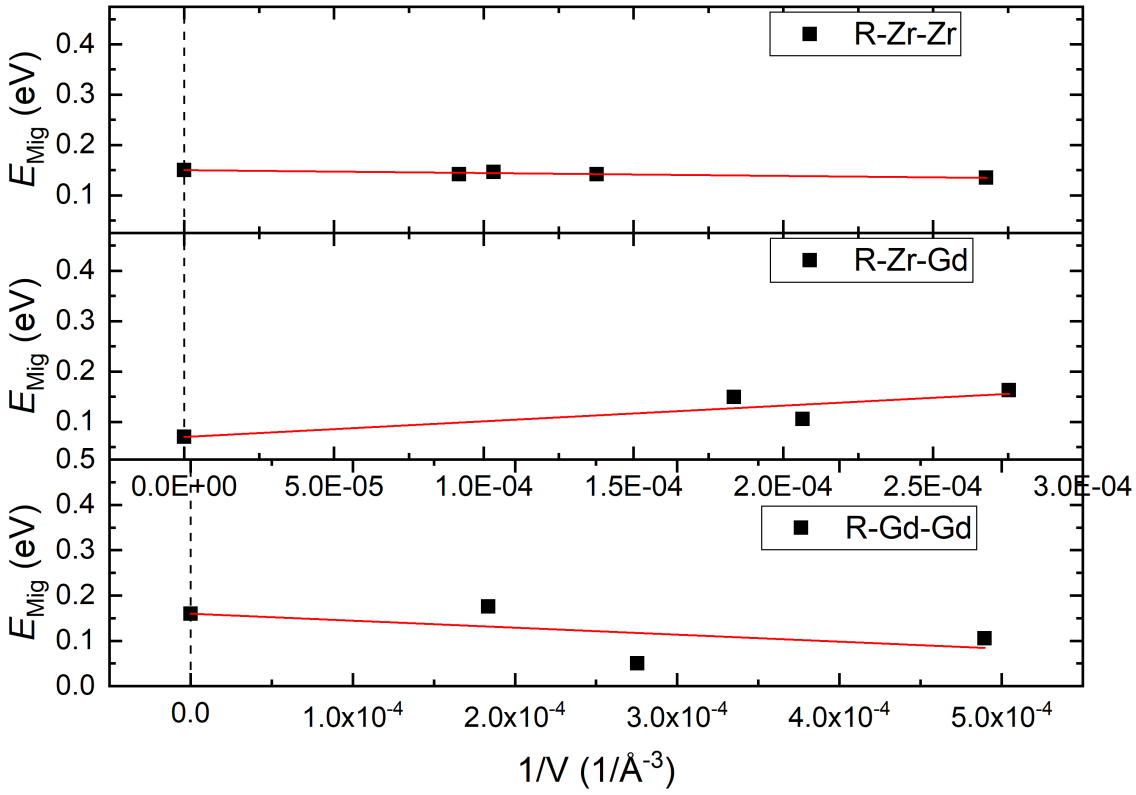


**Figure A.25: Finite size correction of the migration energies of the proton reorientation jumps in gadolinium-doped $BaZrO_3$.** Shown on top is the R-Zr-Zr jump, in the middle the R-Zr-Gd jump and on the bottom the R-Gd-Gd jump. At least 3 different super cells were used for the calculations and extrapolated to $1/V = 0$.

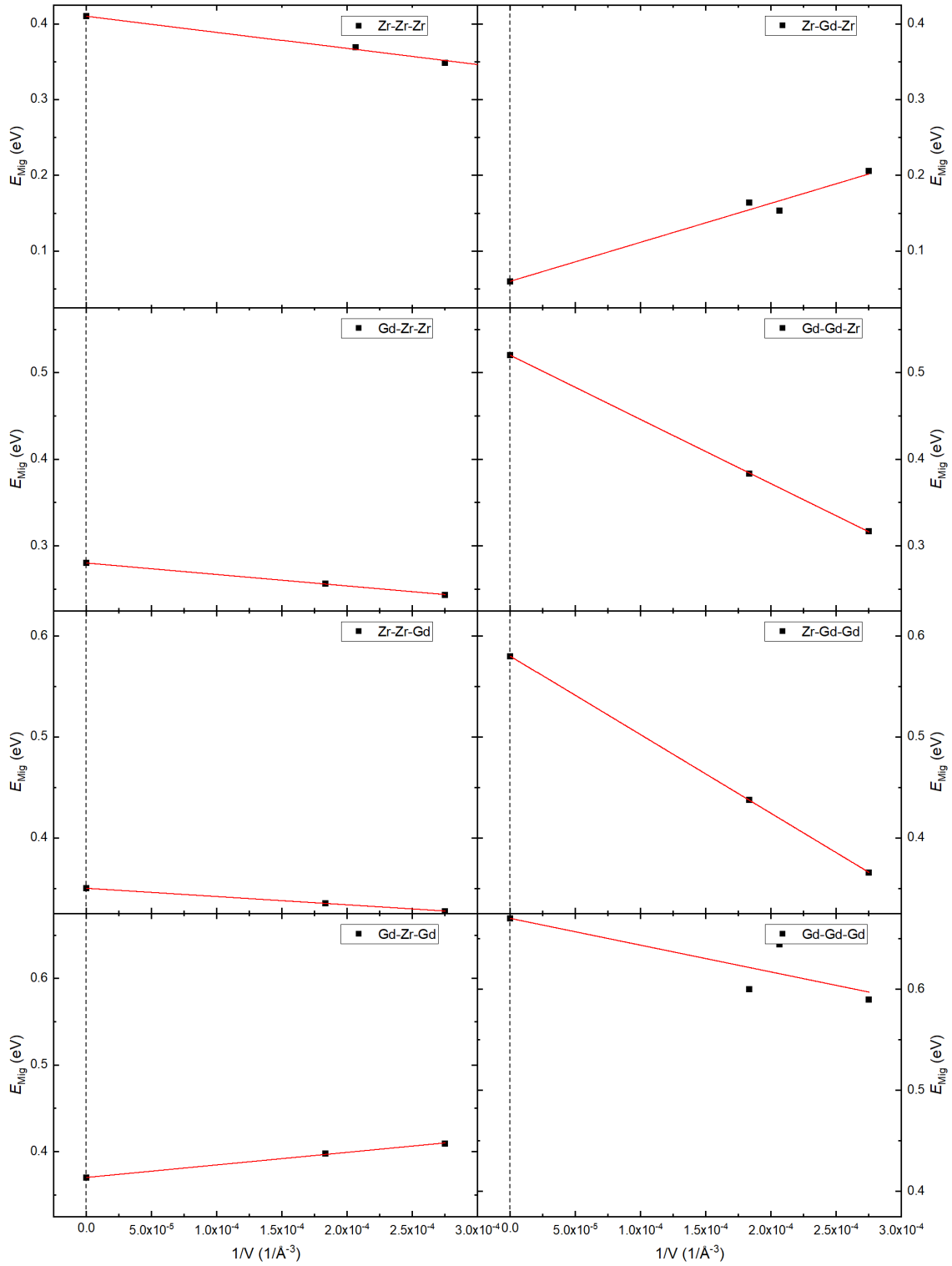


**Figure A.26: Finite size correction of the migration energies of the proton translation jumps in gadolinium-doped $BaZrO_3$.** The nomenclature is explained in chapter 5. At least 3 different super cells were used for the calculations and extrapolated to $1/V = 0$.

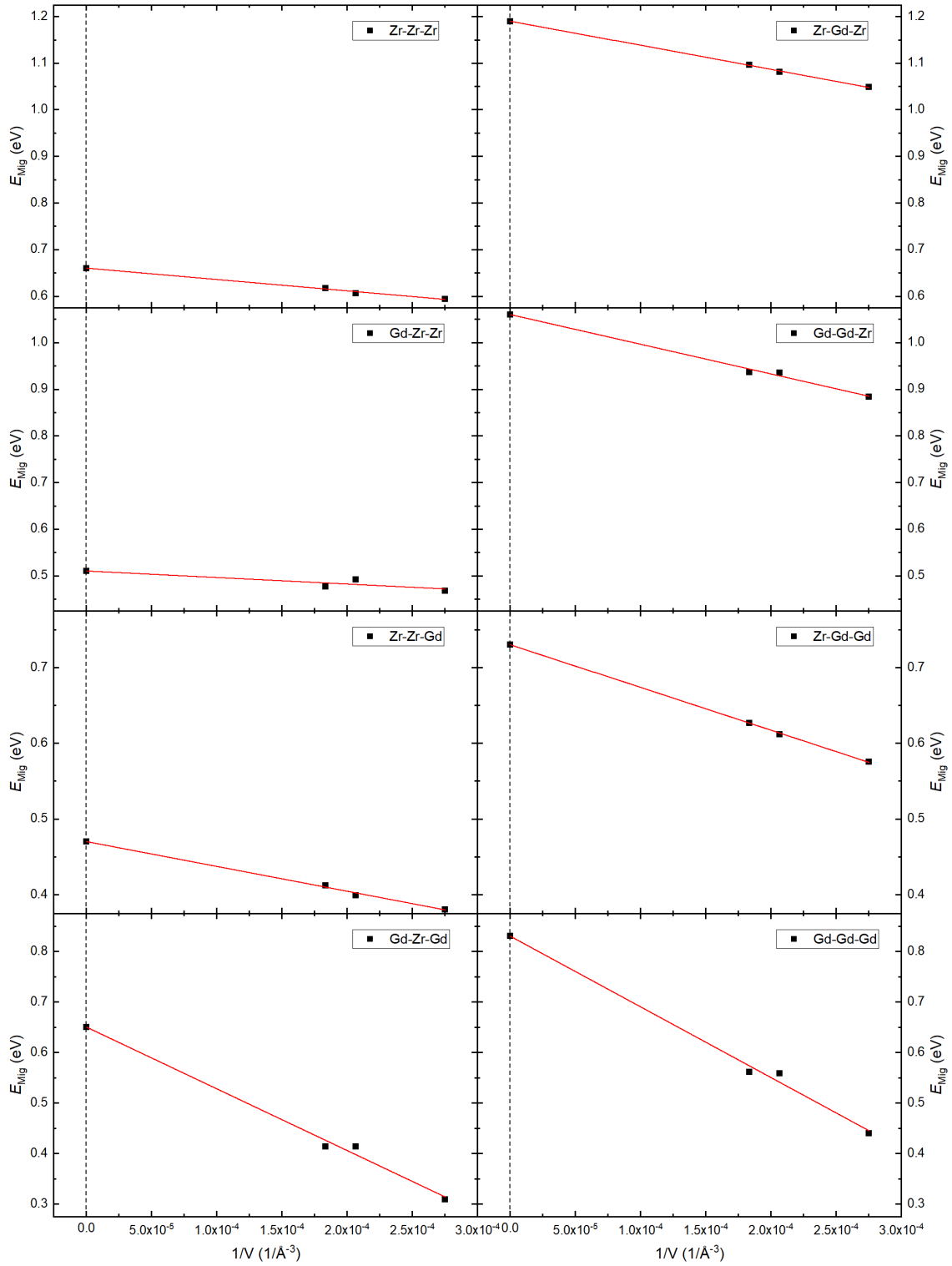


**Figure A.27: Finite size correction of the migration energies of the oxygen vacancy translation jumps in gadolinium-doped $BaZrO_3$.** The nomenclature is explained in chapter 5. At least 3 different super cells were used for the calculations and extrapolated to $1/V = 0$.

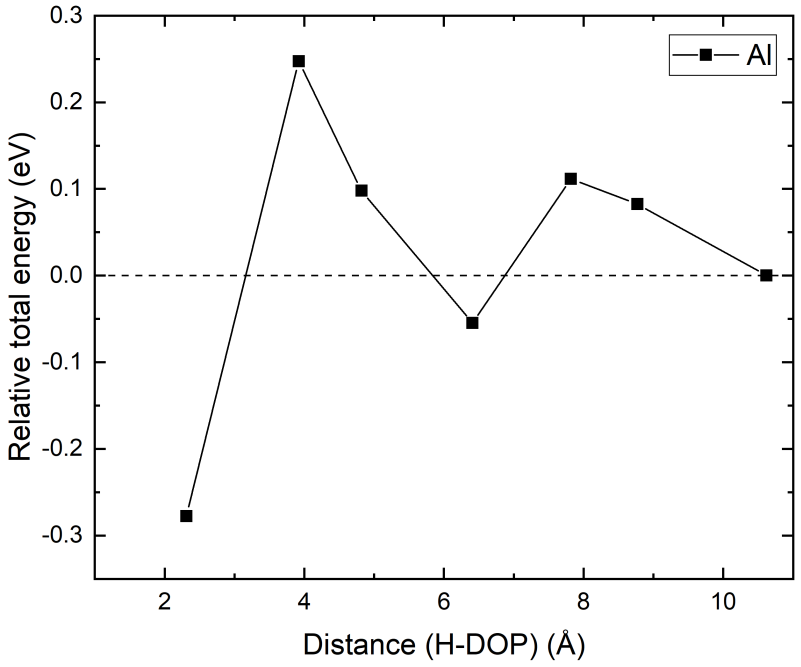


**Figure A.28: The relative total energy of a supercell that contains one dopant ion and one proton at different distances.** Energies are related to the energy that corresponds to the largest distance, which is set to 0.0 eV. Calculations were performed in a 320-atom supercell.

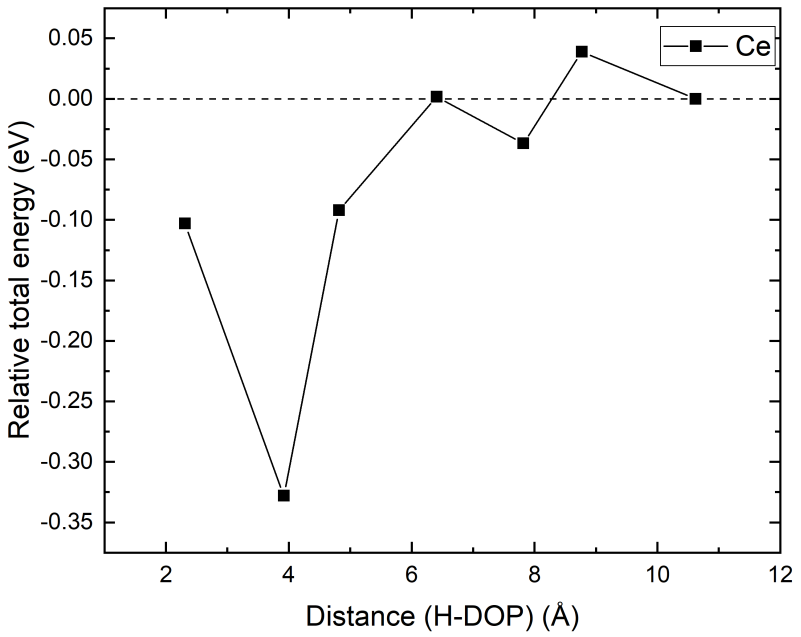


**Figure A.29: The relative total energy of a supercell that contains one dopant ion and one proton at different distances.** Energies are related to the energy that corresponds to the largest distance, which is set to 0.0 eV. Calculations were performed in a 320-atom supercell.

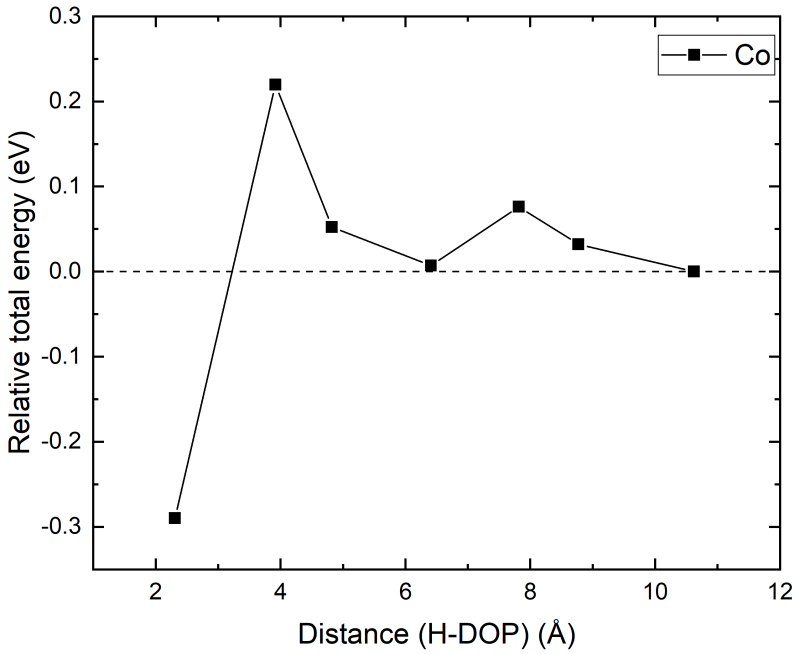


**Figure A.30: The relative total energy of a supercell that contains one dopant ion and one proton at different distances.** Energies are related to the energy that corresponds to the largest distance, which is set to 0.0 eV. Calculations were performed in a 320-atom supercell.

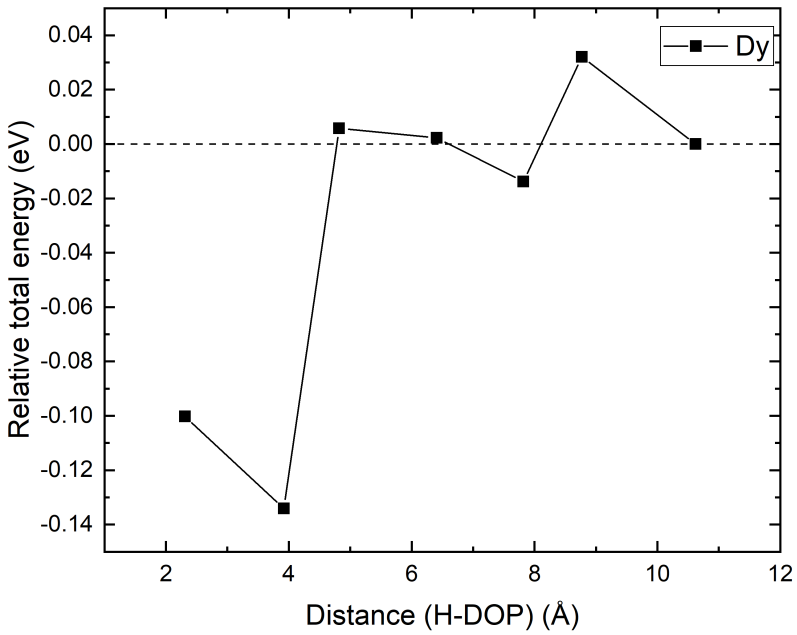


**Figure A.31: The relative total energy of a supercell that contains one dopant ion and one proton at different distances.** Energies are related to the energy that corresponds to the largest distance, which is set to 0.0 eV. Calculations were performed in a 320-atom supercell.

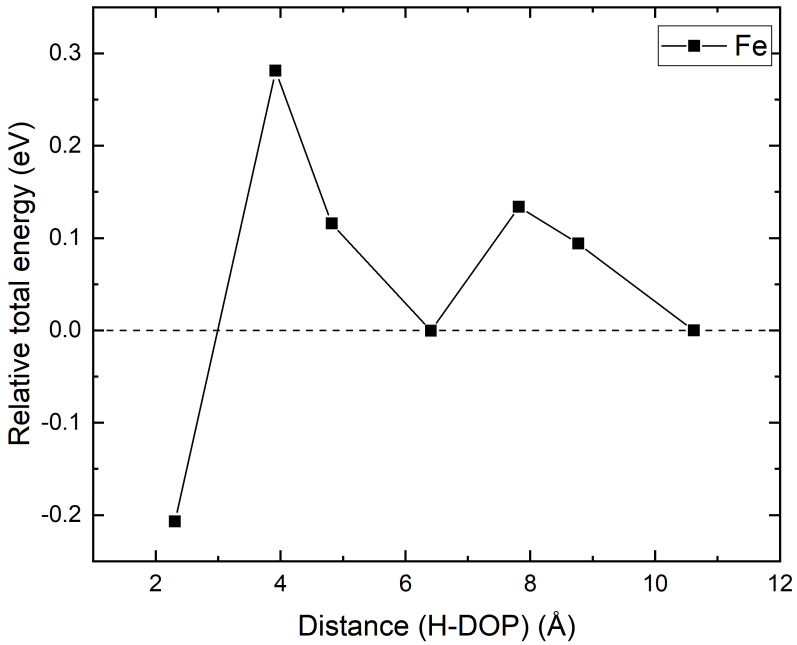


**Figure A.32: The relative total energy of a supercell that contains one dopant ion and one proton at different distances.** Energies are related to the energy that corresponds to the largest distance, which is set to 0.0 eV. Calculations were performed in a 320-atom supercell.

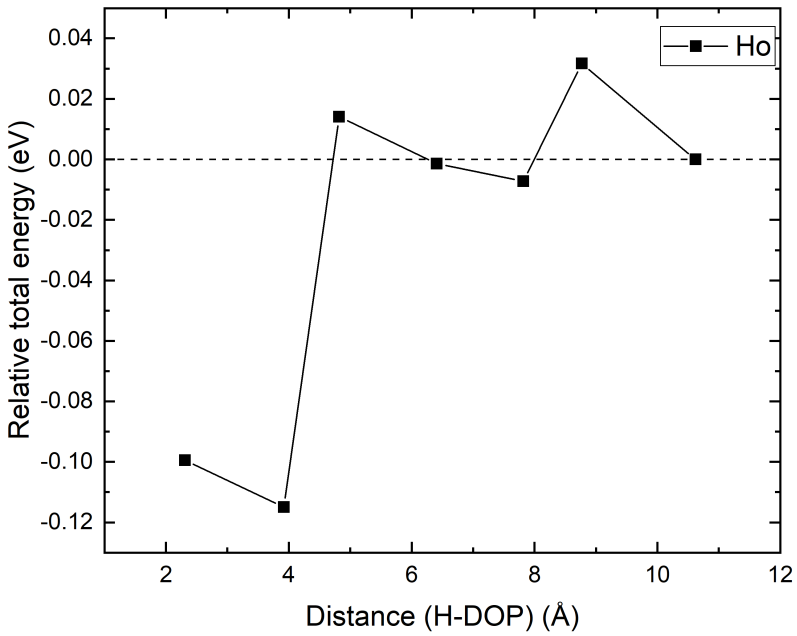


**Figure A.33: The relative total energy of a supercell that contains one dopant ion and one proton at different distances.** Energies are related to the energy that corresponds to the largest distance, which is set to 0.0 eV. Calculations were performed in a 320-atom supercell.

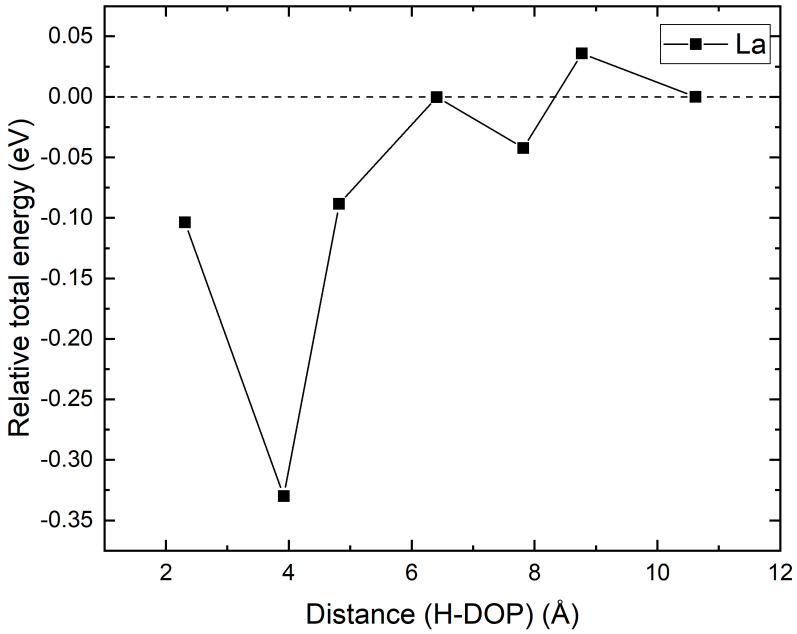


**Figure A.34: The relative total energy of a supercell that contains one dopant ion and one proton at different distances.** Energies are related to the energy that corresponds to the largest distance, which is set to 0.0 eV. Calculations were performed in a 320-atom supercell.

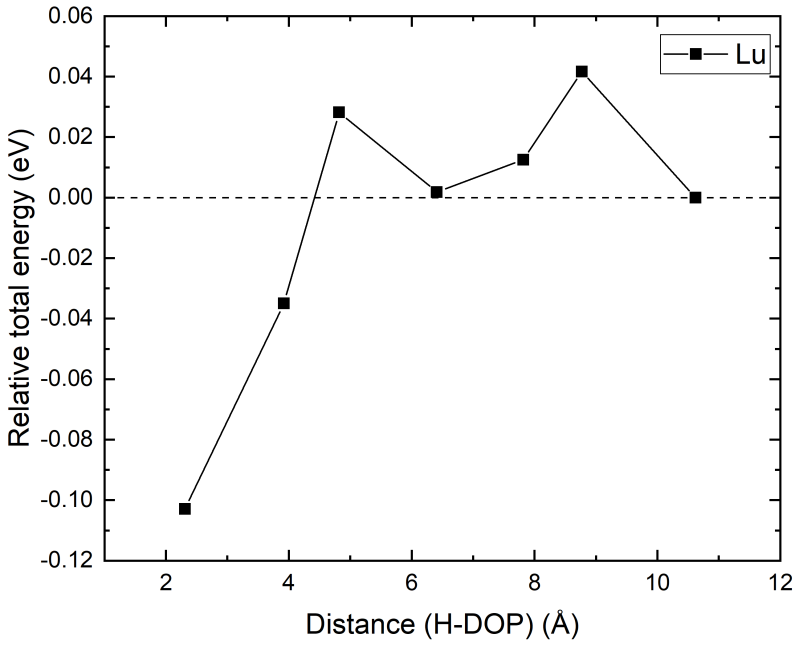


**Figure A.35: The relative total energy of a supercell that contains one dopant ion and one proton at different distances.** Energies are related to the energy that corresponds to the largest distance, which is set to 0.0 eV. Calculations were performed in a 320-atom supercell.

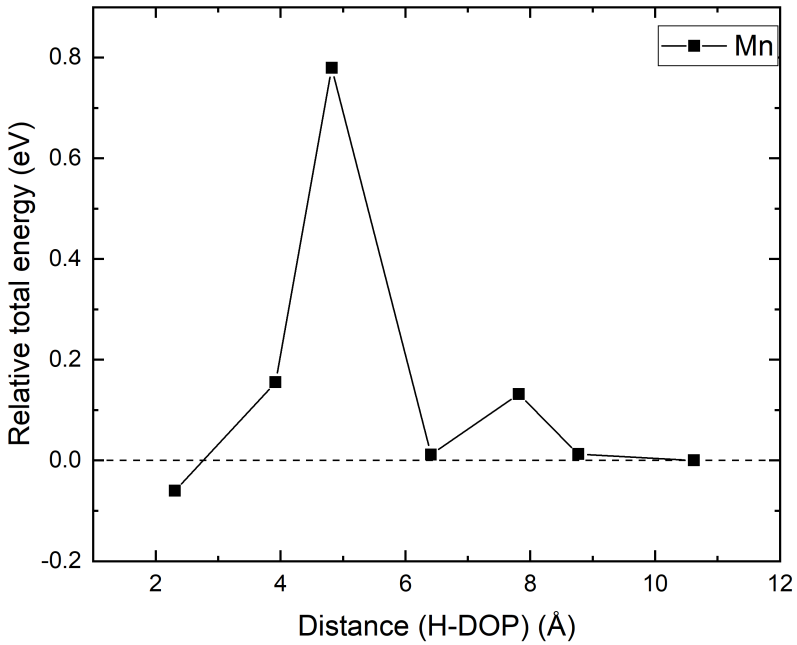


**Figure A.36: The relative total energy of a supercell that contains one dopant ion and one proton at different distances.** Energies are related to the energy that corresponds to the largest distance, which is set to 0.0 eV. Calculations were performed in a 320-atom supercell.

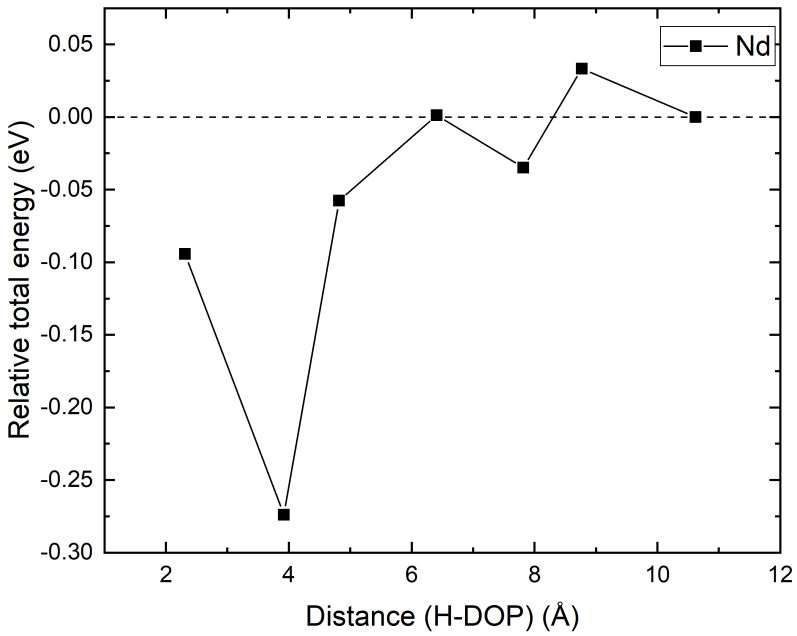


**Figure A.37: The relative total energy of a supercell that contains one dopant ion and one proton at different distances.** Energies are related to the energy that corresponds to the largest distance, which is set to 0.0 eV. Calculations were performed in a 320-atom supercell.

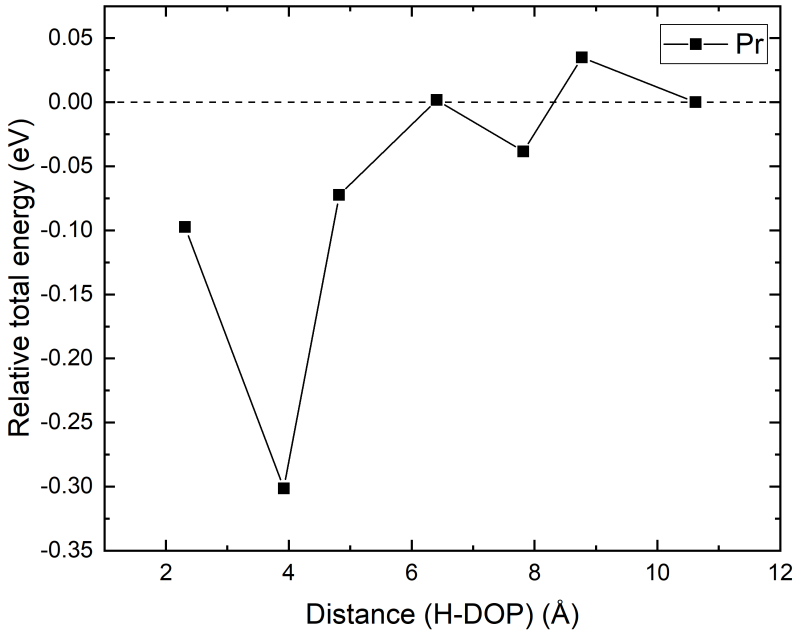


**Figure A.38: The relative total energy of a supercell that contains one dopant ion and one proton at different distances.** Energies are related to the energy that corresponds to the largest distance, which is set to 0.0 eV. Calculations were performed in a 320-atom supercell.

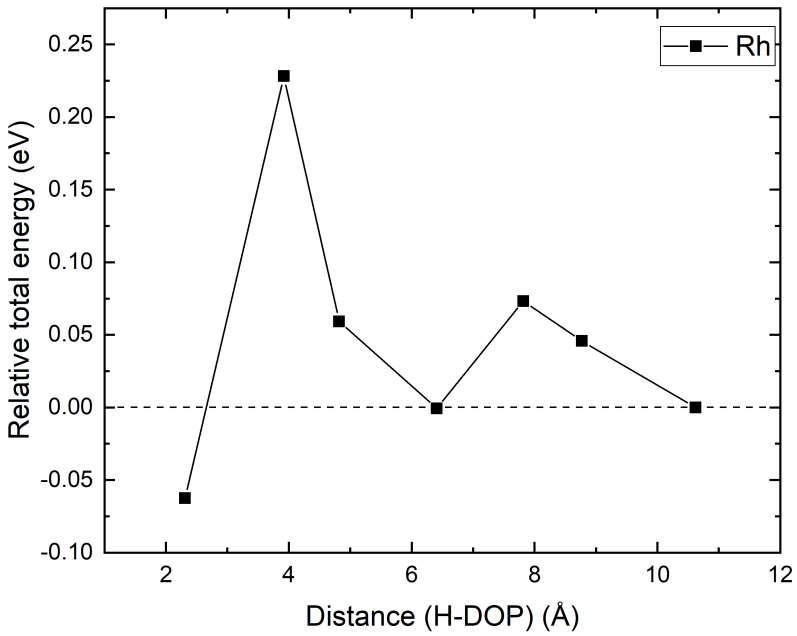


**Figure A.39: The relative total energy of a supercell that contains one dopant ion and one proton at different distances.** Energies are related to the energy that corresponds to the largest distance, which is set to 0.0 eV. Calculations were performed in a 320-atom supercell.

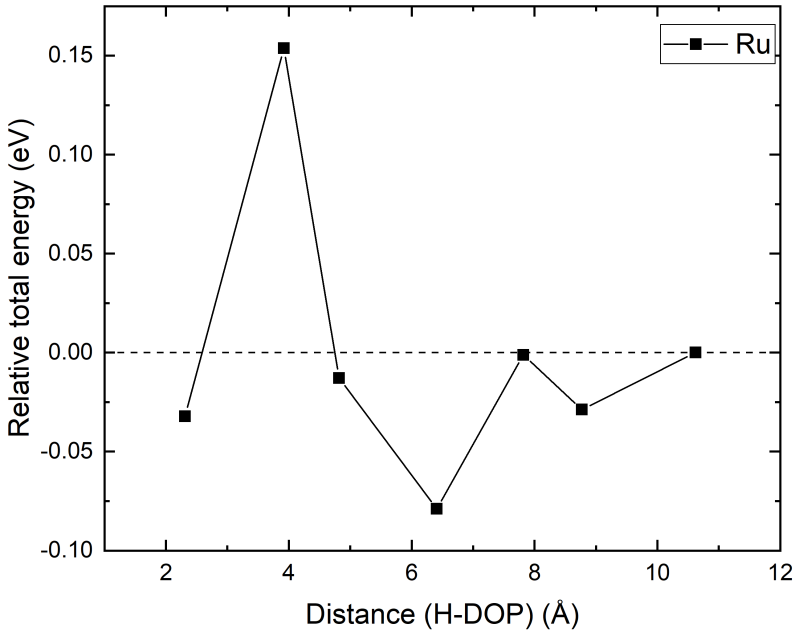


**Figure A.40: The relative total energy of a supercell that contains one dopant ion and one proton at different distances.** Energies are related to the energy that corresponds to the largest distance, which is set to 0.0 eV. Calculations were performed in a 320-atom supercell.

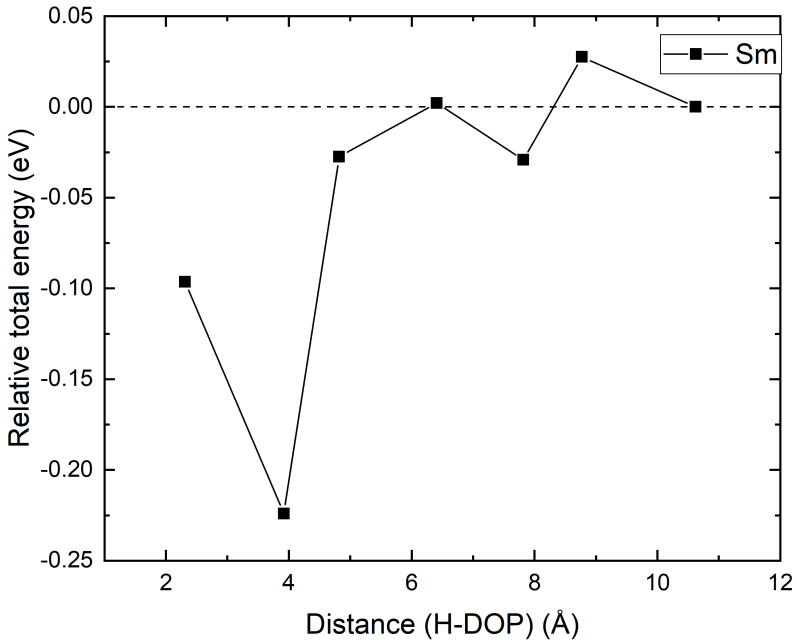


**Figure A.41: The relative total energy of a supercell that contains one dopant ion and one proton at different distances.** Energies are related to the energy that corresponds to the largest distance, which is set to 0.0 eV. Calculations were performed in a 320-atom supercell.

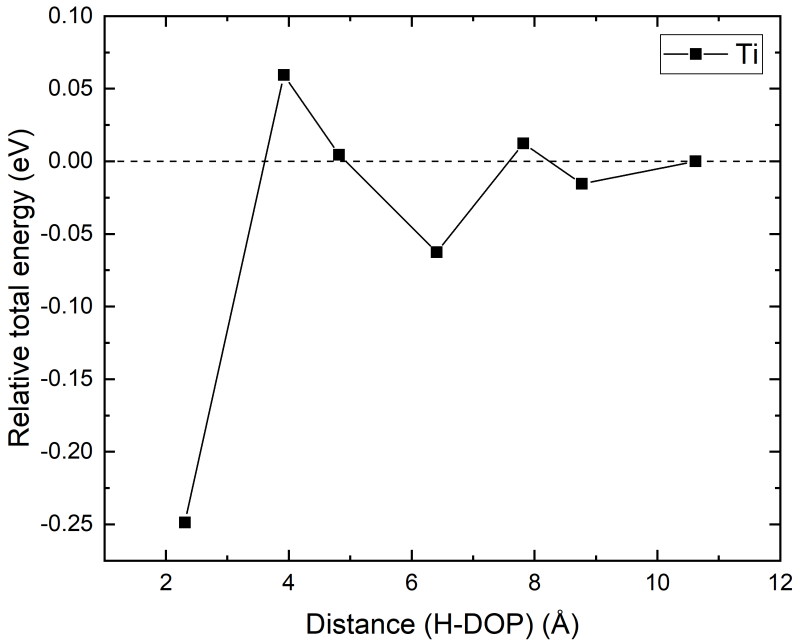


**Figure A.42: The relative total energy of a supercell that contains one dopant ion and one proton at different distances.** Energies are related to the energy that corresponds to the largest distance, which is set to 0.0 eV. Calculations were performed in a 320-atom supercell.

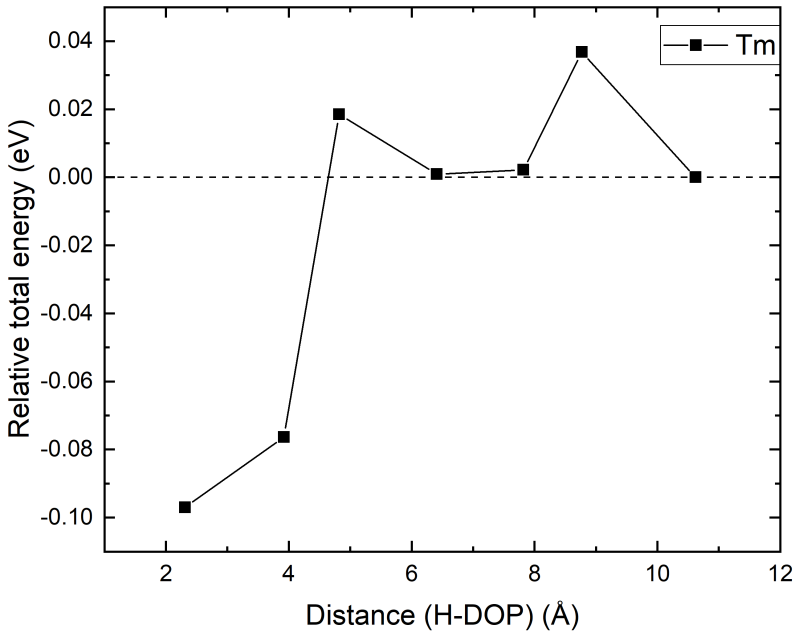


**Figure A.43: The relative total energy of a supercell that contains one dopant ion and one proton at different distances.** Energies are related to the energy that corresponds to the largest distance, which is set to 0.0 eV. Calculations were performed in a 320-atom supercell.